

NASA Contractor Report 165427

(NASA-CR-165427) AN EXPERIMENTAL STUDY OF
COMBUSTION: THE TURBULENT STRUCTURE OF A
REACTING SHEAR LAYER FORMED AT A
REARWARD-FACING STEP. IN: PROCEEDINGS OF THE
FIRST INTERNATIONAL CONFERENCE ON COMBUSTION,
MILWAUKEE (WISCONSIN UNIV., BERKELEY).

81-32140

HC A08/MF A01

8/07 2/513

**AN EXPERIMENTAL STUDY OF COMBUSTION: THE TURBULENT
STRUCTURE OF A REACTING SHEAR LAYER FORMED AT A
REARWARD-FACING STEP**

Robert W. Pitz and John W. Dally
University of California
Berkeley, California

August 1981

Prepared for
NATIONAL AERONAUTICS AND SPACE ADMINISTRATION
Lewis Research Center
Under Grant NSG-3227

and

NATIONAL SCIENCE FOUNDATION
Engineering Energetics Program
Under Grant ENG 77-02019

ORIGINAL PAGE IS
OF POOR QUALITY

ERRATA

NASA Contractor Report 165427

AN EXPERIMENTAL STUDY OF COMBUSTION: THE
TURBULENT STRUCTURE OF A REACTING SHEAR
LAYER FORMED AT A REARWARD-FACING STEP

Robert W. Pitz
August 1981

The cover and the report documentation page should be replaced with the attached pages to indicate the inclusion of the coauthor, John Daily, and the cosponsor, the National Science Foundation.

Page 18: Equation 2.2 should be

$$\nu_D = U/d_f$$

Page 19: Equation 2.5 should be

$$\nu_D = U/d_f + \nu_0$$

Page 23: Equation 2.6 should be

$$U_i = (\nu_{D_i} - \nu_0)/d_f$$

Page 48, figure 2.9: The value for $\theta/2$ should be given as $\theta/2 = 4.76^\circ$, where θ is the beam crossing angle.

Page 58, lines 7 and 11: The symbol for Reynolds number should be Re_x .

Page 71, line 23: The symbol for Reynolds number should be Re_θ .

Page 90: Equation 3.9 should be

$$Str_H = 1.79 \left(\frac{H}{x - x_0} \right)^{0.117}$$

Page 153, figure 3.5: The label for the curve should be

$$\frac{H\bar{f}}{U_c} = 1.79 \left(\frac{x - x_0}{H} \right)^{-0.117}$$

1. Report No. NASA CR-165427		2. Government Accession No.		3. Recipient's Catalog No.	
4. Title and Subtitle AN EXPERIMENTAL STUDY OF COMBUSTION: THE TURBULENT STRUCTURE OF A REACTING SHEAR LAYER FORMED AT A REARWARD-FACING STEP				5. Report Date August 1981	
				6. Performing Organization Code	
7. Author(s) Robert W. Pitz and John W. Daily				8. Performing Organization Report No. None	
				10. Work Unit No.	
9. Performing Organization Name and Address University of California Berkeley, California				11. Contract or Grant No. NSG-3227 and ENG 77-02019	
				13. Type of Report and Period Covered Contractor Report	
12. Sponsoring Agency Name and Address National Aeronautics and Space Administration Washington, D. C. 20546 and National Science Foundation Washington, D. C. 20550				14. Sponsoring Agency Code 505-32-32	
				15. Supplementary Notes Final report, Project Managers, Cecil J. Marek, Aerothermodynamics and Fuels Division, NASA Lewis Research Center, Cleveland, Ohio, and Royal Rostenback, Engineering Energetics Program, National Science Foundation. Report was submitted as a dissertation by the first author in partial fulfillment of the requirements for the degree of Doctor of Philosophy in Engineering at the University of California at Berkeley in May 1981.	
16. Abstract A premixed propane-air flame is stabilized in a turbulent free shear layer formed at a rearward-facing step. The mean and rms averages of the turbulent velocity flow field are determined by LDV for both reacting ($\phi = 0.57$) and non-reacting flows ($Re = 1.5 \times 10^4$ to 3.7×10^4 based on step height). The reacting flow is visualized by high speed schlieren photography. Large scale structures dominate the reacting shear layer. The growth of the large scale structures is tied to the propagation of the flame. The linear growth rate of the reacting shear layer defined by the mean velocity profiles is unchanged by combustion but the virtual origin is shifted downstream. The reacting shear layer based on the mean velocity profiles is shifted toward the recirculation zone and the reattachment lengths are shortened by 30%. The edge of the flame controlled by the large scale structure development propagates faster into the incoming reactants than the boundary of the shear layer given by the mean velocity flow field. This results in non-Gaussian behavior above the shear layer. The velocity probability density function is positively skewed from the impelling effect of the large scale structures expanding between the top of the shear layer and the flame boundary. Under combustion, measurements of the passing frequency of the large scale structures from LDV spectra indicate that the coalescence rate is sharply reduced. The pairing process in the reacting shear layer is sharply eliminated as a growth mechanism. The reacting shear layer grows primarily by entrainment of fluid and heat expansion.					
17. Key Words (Suggested by Author(s)) Large scale turbulence; Turbulence; Combustion; Premixed propane; Velocity probability functions			18. Distribution Statement Unclassified - unlimited STAR Category 07		
19. Security Classif (of this report) Unclassified		20. Security Classif (of this page) Unclassified		21. No of Pages 164	22. Price*

Chapter 1

INTRODUCTION

1.1 Motivation

The turbulent shear layer is an important flow structure in most industrial combustors. Premixed flames are stabilized by heat recirculation involving the recycling of hot products which are mixed with cold reactants in a turbulent shear layer. Diffusion flames are controlled by the rate at which fuel and oxidizer mix in a turbulent shear layer.

There has been considerable interest in premixed combustion related to gas turbine engines because of the pollutant advantages (Jones et al, 1978). Premixed combustion in model gas turbine combustors can give a twentyfold decrease in nitric oxide emissions (Lefebvre, 1977). A particularly simple experimental configuration incorporating the aspects of premixed combustion stabilized in a turbulent shear layer is the rearward-facing step combustor (Figure 1.1). A premixed flame forms in a two-dimensional turbulent shear layer formed at the edge of a rearward-facing step. Stabilization is achieved by recirculation of hot products behind the step which mix with the incoming premixed reactants in the shear layer.

The two-dimensional, rearward-facing step combustor facilitates easy access for experimental viewing by advanced laser diagnostics and flow visualization. Measurements in turbulent, reacting flows are limited and necessary for comparison to turbulent models. The rearward-facing or backward-facing step flow has been the subject of considerable modeling efforts (Marvin, 1977, Ashurst, 1979). Also

recently Ghoniem et al (1980) used a random vortex technique (Chorin, 1973) to model the rearward-facing step combustor. The two-dimensionality of the rearward-facing step flow make it more tractable for modeling.

In earlier work, Ganji and Sawyer (1980) described the flow field of the rearward-facing step combustor with high speed schlieren photography. They found the flow field is dominated by large scale structures with an ordered pattern previously unreported in combustion flows. The reacting, turbulent shear layer structure is similar to that found in turbulent mixing layers where the importance of large scale structures has already been established (Brown and Roshko, 1974). The purpose of this work is to quantify the effect of combustion on the shear layer dynamics. The turbulent velocity is mapped in detail by laser Doppler velocimetry (LDV) for both isothermal and reacting flows. The effect of combustion on the rearward-facing step flow properties such as the shear layer growth rate, entrainment rate, turbulence development, and large scale structure development are determined.

1.2 Background

The turbulent structure of the rearward-facing step is largely preserved under combustion. A discussion of its flow field will lead to a better understanding of the reacting flow. The backward facing step flow can be separated into two regions: i) the mixing layer region and ii) the relaxation region (Figure 1.2). The mixing layer region includes the flow from the initial boundary layer at separation to the reattachment point. The relaxation region covers from flow reattachment to the point of full recovery of a turbulent boundary

layer. The first region normally extends 5 - 7 step heights downstream of the step (Eaton and Johnston, 1980a). The reattachment region covers from reattachment to a distance of about 30 times the mixing layer thickness at reattachment (Bradshaw and Wong, 1972). This study focused on the mixing layer region. The mixing layer in a rearward-facing step flow is often called a reattaching shear layer. The reattaching shear layer is initially planar but then curves toward the wall and eventually impinges on the wall at reattachment. The turbulent structure of planar mixing layers is very similar to the reattaching shear layer. Since planar mixing layers have been studied extensively, their current state of understanding will be discussed next.

Mixing layers. The current understanding of the nature of turbulent mixing layers stems from the work of Brown and Roshko (1974). In a series of shadowgraph photographs they showed that the layer is composed of large scale, two-dimensional rollup vortices. The vortices or eddies evolve from a Kelvin-Helmholtz instability of the initial shear layer (Sherman, 1976). These two-dimensional large-scale structures grow by entrainment of fluid and pairing as they are convected downstream (Winant and Browand, 1974). Pairing of eddies is the uniting of two neighboring eddies into one with twice the original size. The pairing process is a result of the inherent instability of two parallel line vortices (Moore and Saffman, 1975). The growth of the eddies determines the growth of the shear layer as a whole.

The process of first bringing the irrotational fluid into the shear layer and then later mixing it microscopically is given the

names entrainment and mixing. The two processes are found to be almost separate and distinct in mixing layers (Dimotakis and Brown, 1976). The large scale structure growth which is responsible for entrainment is mainly a two-dimensional process and not a strong function of Reynolds number.

In the initial shear layer, mixing is a molecular diffusion process within the large scale structures. At Reynolds numbers greater than 10^4 based on the shear layer thickness, Konrad (1976) found a three-dimensional instability appears which increases mixing by 25%. More recently, Roshko and Bernal (1981) reported an intricate three-dimensional structure to the two-dimensional eddies which certainly enhances mixing. Thus the mixing is found to be Reynolds number dependent.

The initial conditions can have a pronounced influence on the large scale structure formation and the subsequent shear layer growth and turbulence development. In a comprehensive review of mixing layers, Birch (1980) suggests that the shear layer flow will not become completely independent of the initial conditions until $Re_x > 2 \times 10^5$. At lower Reynolds numbers, the state of the boundary layer will influence shear layer growth rate, virtual origin, and turbulence development. The relationship between the initial conditions and the shear layer properties is still unresolved. Some researchers report an increase of the growth rate when the inlet boundary layer is tripped (Wyganski and Fielder, 1970, Batt, 1975) while others report a decrease (Browand and Latigo, 1978). Husain and Hussain (1979) tripped the boundary layer in a half jet mixing layer and found the growth rate is lower at first and higher later.

High free stream turbulence influences the shear layer development. Birch (1980) suggests that the free stream turbulence primarily influences the shear layer through the inlet boundary layer and can be ignored for levels less than 0.6%. Chandrsuda et al (1978) found that at high free stream turbulence levels the two-dimensional eddies largely disappear and suggest that the asymptotic state of the turbulent mixing layer is more three-dimensional.

Rearward-facing step: The mixing layer region. The mixing layer region of the rearward-facing step flow, often called the reattaching shear layer, differs from the planar mixing layer. The reattaching shear layer is initially planar, then curves toward the wall and impinges on it at reattachment. This curvature is thought to be responsible for the rapid decrease in shear stress near reattachment (Eaton and Johnston, 1980a, Castro and Bradshaw, 1976).

The recirculation zone behind the step results in variable, non-zero velocities that cause the velocity difference across the layer to vary with downstream distance. The velocity difference in a planar mixing layer is constant. Also the turbulence levels in the recirculation zone are higher (Kim, Kline and Johnston, 1978). Pressure driven, stress bearing fluid is swept into the recirculation zone from the reattachment region (Bradshaw and Wong, 1972). This increases the turbulence levels in the mixing layer (Eaton and Johnston, 1980a). Again the initial conditions influence the flow development. Besides effecting the mixing layer properties discussed earlier, variation of the boundary layer state changes the reattachment length (Eaton and Johnston, 1980a). A comprehensive review of backward-facing step research is given by Eaton and Johnston

(1980b).

Rearward-facing step combustor. The only previous experiments on the rearward-facing step combustor were performed by Ganji and Sawyer (1980). Using high speed schlieren photography they discovered that the reacting flow is dominated by large scale coherent structures found in mixing layers. Combustion is primarily confined to the eddies as they entrain premixed reactants and hot products. The spread of combustion is linked to the growth and development of the large scale structures. Ganji and Sawyer also described the pollutant and stability characteristics of the flow. They made time average measurements of the major gas species throughout the flow field and observed flashback and blowoff with high speed schlieren photography.

1.3 Goals

The primary aim of the present work is to assess the effect of combustion on the turbulent structure of the rearward-facing step flow. This includes the effect of combustion on the shear layer growth, turbulence levels, reattachment length, and large scale structure development. To carry out this goal the following objectives are set down:

1. To construct and develop a frequency shifted, laser Doppler velocimeter (LDV) and make unambiguous, time-resolved, velocity measurements in the turbulent, reacting, recirculating flow.
2. To develop the computer hardware and software to acquire the instantaneous velocity measurement and calculate the appropriate turbulent quantities.
3. To obtain a detailed mapping of the mean velocity and turbulent intensity in both the reacting and non-reacting flow. To

CHARACTERISTICS
OF POOR QUALITY

7

evaluate the shear layer growth rate, entrainment rate, and recirculation length in both cases.

4. To record the velocity probability density functions (PDFs) and determine the effect of combustion on the higher order moments.
5. To compare the large structure formation and development in the reacting and non-reacting shear layers by frequency analysis of the LDV signal and visualization of the flow field by high speed schlieren movies.

ORIGINAL PAGE IS
OF POOR QUALITY

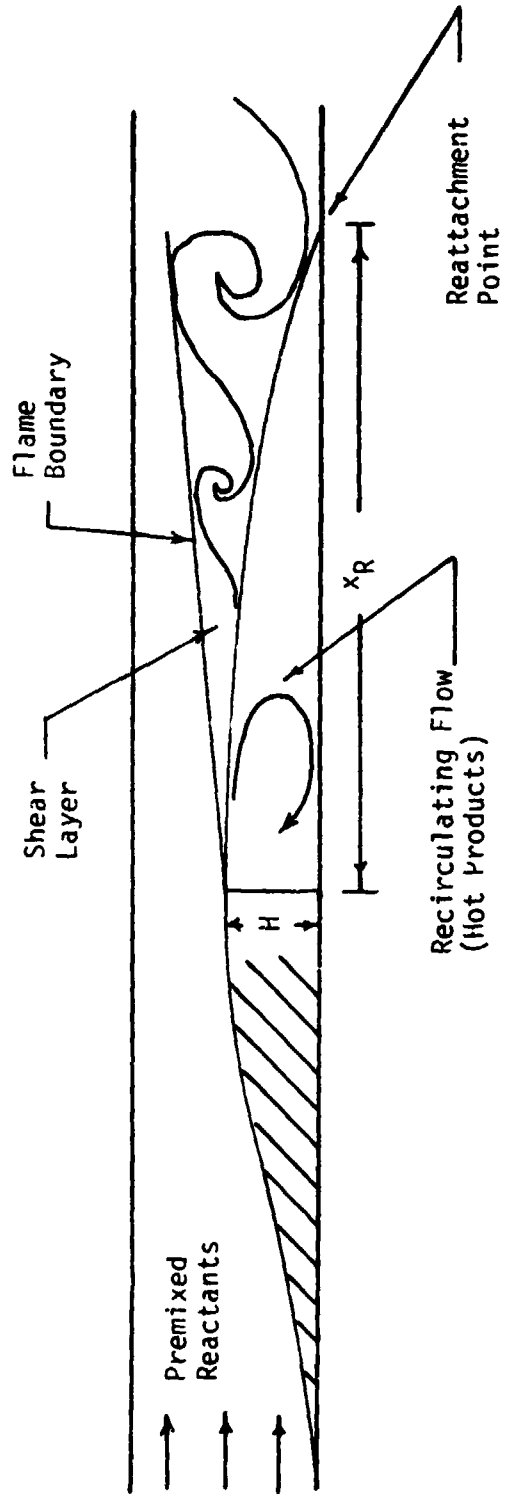


Figure 1.1: Rearward-facing step combustor.

ORIGINAL PAGE IS
OF POOR QUALITY

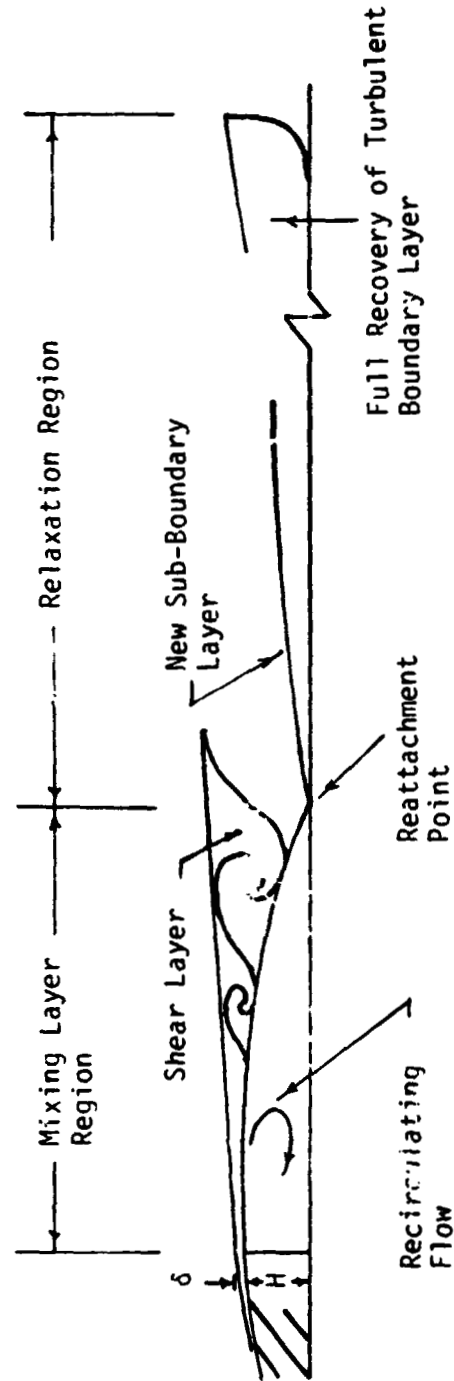


Figure 1.2 Rearward-facing step flowfield.

Chapter 2

EXPERIMENTAL APPARATUS AND INSTRUMENTATION

2.1 The Two-Dimensional Combustor

The two-dimensional combustor apparatus was basically unchanged from that described by Ganji (1979) or Ganji and Sawyer (1980). The major improvements included accurate pressure regulation, lowered inlet turbulence levels, and elimination of the air cooling in the test section.

A schematic of the overall system is viewed in Figure 2.1 and photographs are shown in Figures 2.4 and 2.10. The coordinate system used in the point measurements is given in Figure 2.3. A compressor supplied air at a maximum gage pressure of 650 kPa and a maximum flowrate of 0.5 kg/s. A Fisher series 99 pilot operated pressure regulator maintained the air pressure within $\pm 1\%$ of the set value. The air was dried below 20% humidity by a desiccant drier and filtered by a Balston air filter (Balston Filter Products, Lexington, Mass.). The Balston type A filters have a 99.9999% retention efficiency for 0.6 micron particles. The air stream was split and metered by two sonic nozzles which were calibrated at the Naval Air Rework Facility in Alameda, California to an uncertainty of less than .25%. During the laser Doppler velocimetry (LDV) measurements, additional air containing the particle seed was added directly downstream of the nozzles (See Section 2.5.6). The air was recombined at a manifold and passed through three parallel Venturi tubes. Fuel was injected at the throat of each Venturi tube.

The propane fuel was supplied by two 45 kg bottles of liquid

propane placed in steam heated water baths to maintain a constant fuel pressure. The fuel was metered by a Fisher-Porter (No. FP-3/4-27-G-10/80) or a Matheson 305 rotameter depending on the flowrate requirements. The fuel flow was controlled by a needle valve downstream of the rotameters. The fuel then passed thru a solenoid shutoff valve and flame arrestor before mixing with the air in the venturi section.

The cross section of the combustor is shown in Figure 2.2. After the fuel and air were mixed in the venturis, they entered a one meter long premix section 51 mm high and 173 mm wide. The section was packed with fine grade stainless steel wool to reduce the inlet turbulence level and prevent flashback. A stainless steel screen (80 mesh) was stretched across the end of the premix section to contain the packing. A brass foil safety port was designed to blowout at excessive pressures. The flow converged over the backside of a profiled step (Ganji, 1979) with a 2:1 area ratio. The two-dimensional shear layer formed at the edge of the 25 mm high step.

The test section was 220 mm long, 173 mm wide, and 51 mm high giving an aspect ratio (channel width to step height) of 6.9. Quartz windows (12.7 mm thick, Corning 7940 fused silica) were installed on the sides of the test section exposing 13 mm of the step and extending the entire length of the test section. Access ports (4.8 mm dia.) were provided on the centerline of the top and bottom plates of the test section at 10 mm intervals downstream of the step. The hot exhaust gases passed out of the test section into a 100 mm diameter exhaust pipe. Cooling water flowed thru the rear of the test section and was sprayed into the exhaust. A disc in the exhaust line was

rotated to adjust the test section pressure which was set at one atmosphere for all tests.

A safety system was designed to shut down the combustor in case of hazardous conditions. Detectors were placed throughout the system (see Figure 2.1) and shut the combustor down under the following circumstances:

Detector	Hazardous condition
1. Flame detector	Flame in premix section (flashback)
2. Over pressure	Excessive pressure in premix section
3. Water pressure	Cooling water loss
4. Under temperature	Exhaust temperature drop (flameout)
5. Air flow	Air flow loss
6. Fuel leak	Propane leak in room

The steam heated fuel baths were equipped with a independent safety system that turned off the steam and rang an alarm if the water bath temperature became too high.

To ignite the combustor, a high voltage ignitor rod was inserted into the shear layer from the top plate. The ignitor was located 50 mm downstream from the step and was normally withdrawn from the test section after ignition.

Chromel alumel thermocouples were installed throughout the system and connected to a single selector switch. A digital thermometer (Omega model 2160A-K) displayed the temperature with an accuracy of $\pm 1K$. Thermocouples measured the gas temperature at the sonic nozzles, fuel rotameters, and the test section entrance. Pressure transducers (Senso Metric model SP91) sensed the pressure upstream of each nozzle and fuel rotameter with an accuracy of 1% of full scale. A single

digital panel meter indicated the pressure readings.

2.2 Data Acquisition System

A PDP 11/34 computer system was utilized to calculate and store the overall flow conditions of the combustor during the experiments. The software package contained all the calibration curves of the fuel rotameters, sonic nozzles, pressure transducers, and the air rotameter (only used during LDV measurements). All the pertinent pressures and temperatures were directly keyed into a CRT terminal. The desired equivalence ratio, ϕ , and reference flow velocity, U_0 , (average inlet velocity) were input and the program calculated the corresponding settings for the sonic nozzles and fuel rotameter. A summary of the combustor data stored by the computer program is shown in Table 2.1. The system temperatures and pressures were constantly updated to maintain the desired equivalence ratio and inlet flow velocity. The accuracy of the inlet velocity and the equivalence ratio settings were 1.3% and 6% respectively.

2.3 Schlieren System

An important aspect of the experiments was a series of high speed schlieren movies and long exposure photographs taken of the turbulent free shear layer. A conventional "z" configuration was used in the experiment (Figure 2.5). The output of a 1000 watt xenon arc lamp (Oriel Optics, model C-60-50) was collimated by a 3.94 M focal length, 0.3 M diameter spherical mirror. The collimated light passed through the test section and was refocused by a second identical mirror onto the schlieren stop plane. A lens imaged light emanating from the test section onto the camera film plane. A 102 x 127 mm box camera was used for the long exposure (1/30 sec) photographs. The high speed movies

were recorded by a Hycam camera (Redlake Corp., model 41-0004) at framing rates ranging from 5000-8000 frames/sec.

Movies visualizing the entire flow field and enlarged high resolution movies of just the initial portion of the flow field were obtained. Complete specifications of the schlieren optics are given in Table 2.2 and Figure 2.5.

A typical polar diagram of the deflected light at the schlieren stop plane is shown in Figure 2.6. The distinct vertical and horizontal deflections result from temperature gradients on the combustor surfaces. Thermal boundary layers on the top of the step, and the top and bottom plates of the combustor produced the bright vertical lines. Light deflected from thermal gradients near the front of the step generated the horizontal line. The broad, dispersed pattern on the photograph resulted from index of refraction gradients in the shear layer. In order to visualize the shear layer, the schlieren stops were tailored to highlight the dispersed deflections from the shear layer and minimize interference from the wall boundary layers.

The schlieren photography was only used for visualization of the shear layer. No attempt was made to deduce temperature information from the photographs. Ganji and Sawyer (1980) give a detailed discussion of light refraction in a combusting media.

2.4. Hot Wire Anemometry

Although most of the velocity measurements were carried out using laser Doppler velocimetry, the superior frequency response and ease of operation of hot wire anemometry made the technique useful for the characterization of the entry flow. The hot wire measurements were

limited to the entry region where the flow direction was unambiguous. Hot wire measurements in the entry region also served as a check on the LDV velocity measurements.

The hot wire equipment included a TSI model 1010 Heat Flux System and a model 1005B Linearizer. Wollaston wire (10% rhodium, 90% platinum) was soldered across a TSI 1210 "u" probe. The sensor had an active length of 1 mm and a diameter of 8 microns. The hot wire probe was calibrated in the low speed wind tunnel facility. A typical calibration curve is shown in Figure 2.7.

Both mean velocity and rms turbulence measurements were made in the entry flow. The hot wire voltages were displayed on a digital volt meter capable of measuring the true rms voltage. The single sample uncertainty (Kline and McClintock, 1953) of the mean velocity measurement at a typical velocity of 10 m/s was 1.5%. The error in the rms velocity was much more difficult to assess. The frequency response of the probe was estimated with a square wave test to be 5 kHz. Individual LDV particles follow the flow more closely than this and the rms turbulence levels measured by the hot wire were lower than the LDV measurements. Also at velocities above 10 m/s the probe vibrated at 9.5 kHz producing spurious rms turbulence of the same order as the actual flow turbulence.

The frequency spectrum of the hot wire fluctuations were recorded by a digital fast Fourier transform analyzer (GenRad model 2512). Shear layers are sensitive to flow instabilities which include acoustical resonances in the combustion tunnel. The hot wire spectrum in the entry flow was checked to confirm that all such resonances were removed (See Section 3.1 for more details).

2.5 Laser Doppler Velocimetry

Due to the hostile nature of the flow environment, laser Doppler velocimetry was selected to quantify the velocity flow field. The hot recirculating, turbulent flow precluded the use of any other technique. Hot wire anemometry, widely used in turbulent shear flow research, cannot withstand the high temperatures or resolve the flow direction. Laser Doppler velocimetry (LDV), also called laser Doppler anemometry (LDA), is able to obtain measurements in combusting flows and resolve the velocity direction while maintaining high frequency response and spacial resolution. LDV has the additional advantages of producing a linear output and causing no flow disturbance.

The technique was first demonstrated by Yeh and Cummins (1964) and since that time has widely used for measurements in laminar and turbulent flows. Applications to non-reacting flow phenomena are extensive and have been reviewed by Durst et al (1972). Measurements in combusting systems are not as numerous and subject to the unique problems of high temperature environments. Index of refraction inhomogeneities caused by chemical concentration and temperature gradients lead to difficulties in achieving a stable location of the laser beams in the flow. Scattering particles are required for LDV and these must be made of refractory materials able to withstand the high temperatures. The special problems of design and application of LDV systems for combustion have been discussed at length by Self and Whitelaw (1976) and Chigier (1977).

2.5.1 Principles of Operation. The LDV measurement technique is based on the well known Doppler effect involving the frequency shift of light waves scattered by a moving object. With the development of

lasers which provided a coherent, monochromatic source of light, this effect was exploited to make precision point measurements of velocity. Particles are required to give sufficient scattered light intensity and the technique is limited by the ability of the particles to follow the flow field. There are numerous types of LDV systems and these are described in various reviews and introductions to the topic such as Drain (1980), Durst et al (1972, 1976), Goldstein and Kreid (1976), Trolinger (1974), Stevenson (1977), and Whitelaw (1975).

The two most predominate optical configurations for LDV are the dual beam, real fringe, differential scattering system and the single scatter, reference beam system (Durst et al, 1972). Due to the ease of alignment and better signal quality, the dual beam, real fringe system was chosen for this experiment. In gas flows, where the particle density is low and the number of particles in the focal volume are few, Drain (1972) has shown theoretically that the dual beam system will give a superior signal to noise ratio (SNR) than the reference beam system.

A typical dual beam, real fringe optical configuration is illustrated in Figure 2.8. The laser output is split into two beams and focused into the flow. An ellipsoidal volume of planar fringes is formed at the intersection of the two beams with a spacing,

$$d_f = \lambda / \{2 \sin(\theta/2)\} \quad 2.1$$

where λ is the laser wavelength and θ is the beam crossing angle. The beam crossing angle is given by the focal length of the focusing lens, f , and the beam separation, d_s , ($\theta = \sin^{-1} d_s/f$). Particles passing

through the fringe pattern will scatter light with a frequency,

$$\nu_D = d_f U \quad 2.2$$

where U is the velocity of the particle perpendicular to the planar fringes. The focal volume in an ellipsoid (Adrian and Goldstein, 1971) with the dimensions (Figure 2.8):

$$\begin{aligned} d_x &= d / \cos(\theta/2) \\ d_y &= d \\ d_z &= d / \sin(\theta/2) \end{aligned} \quad 2.3$$

The waist diameter, d , is the diffraction limited size of the laser beam,

$$d = 2\lambda f / (\pi D) \quad 2.4$$

where D is the laser beam diameter (defined at the $1/e$ intensity points) at the focusing lens (Goldstein and Kreid, 1976).

Light scattered by particles moving through the focal volume is modulated at the Doppler frequency given by equation 2.2. The collecting lens images light emanating from the focal volume on to a photomultiplier tube (PMT). Signal processing deduces the Doppler frequency from the PMT output.

The optical setup shown in Figure 2.8 has one drawback. A 180 degree shift in the velocity direction will result in an identical Doppler frequency. This is referred to as "directional ambiguity".

The difficulty is overcome by shifting one of the beams to a slightly different frequency which causes the fringes to move at a constant velocity (Durst and Zaré, 1974). A particle that is stationary in the focal volume will scatter light at the shifted frequency, ν_0 . As long as the fringe velocity is higher than any particle velocity in the same direction, all velocities will result in a unique, nonzero Doppler shift given by,

$$\nu_D = d_f U + \nu_0 \quad 2.5$$

In this experiment an acousto-optic modulator, a Bragg cell, produced the frequency shift (Durão and Whitelaw 1975).

2.5.2 The Optical System. The actual optical system designed for the experiment is illustrated in Figure 2.9. The output of an argon-ion laser tuned to the 514.5 nm line (0.3 watts) passes through two lenses (l1 and l2) and a polarization rotator (1/4 wave plate, Oriel model 2566). A path compensated beam splitter (OEI, Karlsruhe, West Germany) outputs two beams with a 50 mm separation. The beam splitter is polarization sensitive and the 1/4 wave plate is rotated to equalize the intensity of the output beams. Also the fringe pattern intensity is dependent on the polarization of the beams. Maximum interference is obtained when the two beams are linearly polarized perpendicular to the plane containing them (Stevenson, 1977).

One beam passes through the Bragg cell and is down shifted by 40 MHz causing the fringes to move in the opposite direction to the main flow. The Bragg cell (TSI model 982) is tilted to obtain proper phase

matching (Yarif, 1975) of the input and output beams resulting in a Bragg cell efficiency of 60%. The other beam passes through a path compensator and a neutral density filter (60%) to maintain equal path lengths and beam intensities. The laser beams are focused into the test section by an 82 mm diameter, 300 mm focal length lens (13). Optical access is provided by 12 mm thick quartz windows (Corning 7940).

The probe volume dimensions are given in Figure 2.9. The probe dimensions, position, and fringe parallelism are all subject to the propagation properties of Gaussian laser beams predicted by scalar diffraction theory (Hanson, 1973, Durst and Stevenson, 1977). For proper alignment, the laser cavity, lens positions, focal lengths, optical path lengths, and access windows must all be taken into account. The argon-ion laser operated in a TEM_{00} mode producing a Gaussian shaped output beam. Lenses 11 and 12 were selected to position the laser waist at the beam intersection with a diameter of 96 microns.

In line, forward scatter collection optics were used to obtain the maximum SNR (Durst and Whitelaw, 1971). Particle scattering is governed by Mie scattering theory (particle diameter $\approx \lambda$) where the maximum scattering intensity is in the forward direction. The laser beams were blocked by beam dumps and the scattered light from the focal volume was collected by an f/6 lens (14) and focused on the 0.5 mm diameter pinhole of the PMT housing. An adjustable aperture stop was positioned after the collection lens to minimize scattering from the quartz windows and adjust light levels on the PMT to prevent saturation. A 1 nm bandpass interference filter was installed in the

light tight PMT housing to eliminate room light and flame emission. The Pacific Photometric model 3150 PMT housing incorporated mu-metal tube encasement and a nickle coated exterior to shield against RF noise. An EMI 9761A/B PMT detected and amplified the scattered light and output the Doppler signal for processing.

The laser, transmission and collection optics, and the PMT housing were all secured to a single optical bench. The bench top was mounted to a milling table which allowed the test section to be scanned in all three directions. The LDV optics, laser, and milling table are shown in a photograph of the experimental apparatus in Figure 2.10. Most velocity profiles were taken vertically across the shear layer and a stepping motor drive was installed to easily move the table in the y direction. A dial indicator with a resolution of 0.01 mm displayed the y position. The y direction contained the steep velocity gradients and the milling table could be positioned to ± 0.05 mm. The x and z directions had a positioning accuracy of ± 0.5 mm.

2.5.3 Signal Processing. The signal processing system for the LDV measurements is shown in Figures 2.10 and 2.11. The output from the PMT is amplified by a 140 MHz bandpass, x100 gain preamplifier (Pacific Photometric model AD-6). The frequency shift (40 MHz) of the single Bragg cell is undesirably large. Therefore the shift is effectively reduced by the "downmix" circuit of the TSI model 985 driver/downshifter. A 40 MHz oscillator drives both the Bragg cell power amplifier and the downmix circuit. The effective frequency shift is selectable from 10 kHz to 20 Mhz in a 1, 2, 5, sequence. The frequency shift had a calibration accuracy of 0.0025%.

A Macrodyne model 2096 was selected to analyze the Doppler

frequency. Period counters are preferred over frequency trackers for analysis of single particle LDV signals found in turbulent gas flows. Under low duty ratios, they can be operated with wide input bandwidths allowing a wider range of particle velocities than frequency trackers (Humphrey et al 1975).

The block diagrams for the Macrodyne 2096 modules are given in Figure 2.12 and 2.13. In the Front End Detector (FED), the Doppler signal is first amplified ($\times 1$ or $\times 10$) and filtered. The selectable low pass and high pass filters (0.5, 2, 4, 8, 16, and 32 MHz, 40 db/decade) serve two functions, removing the pedestal and filtering out background noise. A threshold level discriminator on the filtered output prevented processing of residual noise. An overload level discriminator on the amplifier output eliminated large particle or multi-particle bursts.

The burst signal enters a zero crossing detector coupled with a Schmidt trigger (Figure 2.12). The Schmidt trigger outputs a pulse everytime the signal crosses zero and behaves like a sinewave with an amplitude exceeding the threshold level.

The Logic and Output Display (LOG) module performs the 5/8 validation test (Figure 2.13). The time for 5 pulses and the time for 8 pulses is compared. If they are not within a preset accuracy, the signal is not accepted. The Macrodyne has either a 5/8 or 10/16 comparator for the validation test. The 5/8 comparator at an accuracy setting of 2 was used in the experiment. This required that the two periods compare to about 1% accuracy. If the burst was validated a "sync" pulse was output. A validated burst is often described as a "realization". The sync pulses were externally counted to display the

instantaneous data rate (Figure 2.11). The period for 8 pulses (burst period) was timed by a 10 bit (1024 count) counter with variable ranges to cover 1.2 kHz to 100 MHz input frequencies.

The counter had a resolution of 2 ns. At a typical Doppler frequency of 8 MHz using the 5/8 comparator, the burst period is measured to an accuracy of 0.2%. The 10 bit counter outputs the period with the same accuracy. A typical burst period of 500 counts would have an accuracy of 0.2%.

A multiplexer and external clock (0.1 or 1 MHz) were added to output the time between realizations or the data period (Figure 2.13). The burst period, counter range, comparator setting, comparator accuracy, and data period were multiplexed over a 16 parallel line interface to a PDP 11/34 computer. An internal D/A in the Macrodyne was connected to a digital volt meter (DVM) for an continuous display of the burst period (Figure 2.11).

2.5.4 Velocity Data Acquisition and Reduction. A typical LDV data record is shown in Table 2.3. The LDV system parameters and typical values are indicated. In addition to the data directly accessed by the parallel line interface, information on the record length, fringe spacing, Bragg cell shift, and probe location were keyed into the computer. The LDV computer control program collected a 2048 point record on comand from the computer terminal. The instantaneous velocities were calculated according to,

$$u_1 = (v_{D1} - v_0)/df \quad 2.6$$

where v_{D1} is the Doppler frequency of an individual burst. Two types

of velocity averages were calculated, numerical and time integrated averages. The numerical averages are given by:

$$\bar{u} = 1/N \sum_{i=1}^N u_i \quad 2.7$$

$$u_{rms} = [1/N \sum_{i=1}^N (u_i - \bar{u})^2]^{1/2} \quad 2.8$$

where N is the record length, \bar{u} is the mean velocity and u_{rms} is the rms velocity. These averages which are calculated from individual particle bursts are subject to velocity biasing discussed by McLaughlin and Tiederman (1973). In turbulent flow the higher velocity particles have a higher probability of crossing the focal volume than the lower velocity particles resulting in a bias. Dimotakis (1976) suggested that in high data rate regimes the biasing error could be circumvented by the use of the time integrals,

$$\bar{u}_t = 1/T \int u(t) dt \quad 2.9$$

$$u_{rms,t} = [1/T \int (u_i - \bar{u}_t)^2 dt]^{1/2} \quad 2.10$$

where \bar{u}_t and $u_{rms,t}$ are the time integrated mean and rms velocities, respectively. The integrals were integrated numerically by the rectangular rule and time weighted averages of the data record were stored at all measurement locations.

The probability density function (PDF) was also

calculated and stored. The velocity record was divided into 72 equal intervals (bins) between the maximum and minimum velocities. The number of velocity points in each bin was computed to determine the PDF.

Again a time correction was applied to avert the velocity biasing in the PDF at high data rates. Each data point was weighted by the data period (dt). Typical PDFs in the shear layer are shown in Figure 3.28.

Another biasing problem occurred with the PDFs. The Macrodyne output is inversely proportional to the velocity, that is the burst count register is in equal units of time (burst counts) not frequency. Equal intervals in velocity in the 72 bin PDF will not correspond to equal intervals in burst counts. For some high velocity (low burst count) intervals there will be no burst count value corresponding to that velocity interval. The PDF intervals must be weighted by the ratio of dB_e/dB_a where dB_e is the exact width of the velocity interval in burst counts (ie 2.51) and dB_a is the possible number of burst count values that fall in that interval (ie 2). All the PDFs were weighted in this fashion. This did not completely eliminate the biasing problem. The correct method is to store the PDF of the burst period and produce velocity PDFs with equal intervals of burst period and not velocity.

Spectral analysis of the Doppler signal was also performed. Large data records (50,000 - 200,000 points) involving sample periods of a minute or more were required to obtain frequency spectra with sufficient signal quality. The PDP 11/34 had no provision for storage of such large records and the on line fast Fourier transform (FFT)

software was very slow. Hence a FFT analyzer (GenRad model 2512) processed the analog output from the burst period counter. Up to 512 FFTs were averaged by the analyzer to obtain the spectrum. A typical spectrum is shown in Figure 3.46. This is the spectrum of the a.c. component of the burst period rather than the Doppler burst frequency. For low turbulence levels the relationship is linear, but for high turbulence levels the amplitude of the spectra will be biased. The major use of the spectra was to quantify the frequency of the large scale structures in the shear layer and the value of the spectral density was unimportant.

2.5.5 Data Verification. The LDV system had to be checked to ascertain whether the system was generating the correct velocities and turbulence levels. The greatest source of systematic error involved adjustment of the Macrodyne front panel settings: the threshold and overload discriminators, the lowpass and highpass filters, and the counter range.

The threshold setting was determined by the amount of noise measured at the "Filtered Output" (Figure 2.12). The threshold level was set such that the noise would not be validated. First, the threshold level was calibrated (Figure 2.14). The minimum validated sinewave amplitude was measured as a function of the threshold level. For a given threshold setting, if the Doppler burst is above that amplitude and fulfills the other Macrodyne validation criterion, it will be validated. The threshold level could simply be set above the noise level given by this curve.

This was found to be too strict of a criterion. The turbulence intensity and data rate as a function of the threshold setting is

shown in Figure 2.15. At low threshold settings the noise would be validated and the turbulence intensity would depend strongly on the threshold setting. As the threshold level was increased the turbulence intensity would become practically threshold insensitive. The turbulence intensity was never completely independent of the threshold setting since as the threshold increased the Macrodyne would only validate the larger particles which do not follow the flow as well. The threshold was set at the knee of the curve resulting in the optimum data rate, noise rejection, and particle size validation. This corresponded to setting the threshold minimum validated sinewave amplitude to 90% of the noise amplitude at the "Filtered Output". The noise level versus threshold setting calibration curve for this criterion is given in Figure 2.14.

The overload discriminator setting did not make a significant improvement in the turbulence intensity measurement. Large particle rejection was not important and the overload level was simply set well above the input signal levels.

As mentioned earlier the velocity PDF was calculated for each data record. The PDF of the burst period was also displayed on the CRT terminal for each 2048 point record to check the Macrodyne operation. The Macrodyne only accepted a window of Doppler burst frequencies determined by the input filters and counter range. This window had to be larger than the burst frequency bandwidth. Also the Bragg cell shift had to be high enough to obtain nonzero, unambiguous velocity measurements. All these criterion could easily be examined by viewing the burst period PDF. The boundaries of the PDF were displayed in both time and frequency units. The maximum and minimum

burst frequencies were checked against the input filters to prevent cutoff. The Bragg cell shift was adjusted so that the minimum Doppler frequency was above the minimum filter setting of 0.5 MHz. Display of the maximum and minimum burst periods allowed the operator to set the counter range to the highest sensitivity without overflowing the counter register.

Finally the LDV velocity profiles were compared with the hotwire measurements. Also the velocity profiles were integrated and the integrated values were checked against the mass flowrate measurements. This will be discussed in the next chapter.

2.5.6 Particle Seeding. Cyclone aerosol generators described by Glass and Kennedy (1977) were used to suspend alumina (Al_2O_3) particles into the flow (See Figure 2.16). Air forced thru a nozzle, mounted tangentially to a plexiglass cylinder, swirled the air and entrained the alumina particles at the bottom. The particle laden air was drawn out the top. Two generators were mounted in parallel and their exhaust lines were connected to a manifold. The manifold injected the seeded air downstream of the two sonic air nozzles (Figure 2.17b). To minimize contamination of the quartz windows, the alumina particles were injected into the air flow only during the acquisition of the LDV velocity-time record. A three-way solenoid valve directed the seeder secondary air either through the seeders or a bypass so that the total air flowrate was constant at all times (Figure 2.17a).

The alumina particles (0.05 micron dia., $\rho = 3.7 \times 10^3$ Kg/M³, Linde Div., Union Carbide) were dried at 500 K for eight hours before each experiment to limit particle agglomeration. The entraining air

was also dried to prevent additional water absorption. The 3.14 micron fringe spacing prohibited particles over 1.5 microns from generating a Doppler frequency. Measurements by Glass and Kennedy (1977) indicate that particle agglomeration occurs increasing the average particle diameter by about a factor of 3. This would indicate an average particle diameter of about 0.2 microns was produced. One could safely assume that the particle diameter was below 1 micron.

2.5.7 Sources of Error. Errors in the LDV measurement can result from any of the different facets of the measurement system: optical alignment, signal processing, gas medium, and seed particles.

Processor errors. A common source of error in frequency measurement is Doppler ambiguity broadening or transit time broadening (George and Lumley, 1973). The precision which the frequency of a waveform of finite length can be measured is limited. For a processor working in frequency space, a wave form N cycles long is effectively Fourier transformed and the relative width is of order $1/N$. This type of broadening was avoided by using a period counter which works in the time domain (Self and Whitelaw, 1976). The waveform of an individual burst can be timed to a precision only limited by the clock resolution. As discussed earlier (Section 2.5.3) this results in a 0.2% uncertainty.

Optical errors. Besides the frequency measurement, the error in the velocity is dependent on the uncertainty in the beam crossing angle, θ , the laser wavelength, λ , and the Bragg cell shift, ν_0 , (Equations 2.1 and 2.6). The single sample uncertainty for the velocity measurement was estimated to be 0.4%.

Fringe gradient broadening. Additional broadening in the Doppler

signal can result from curved fringes in the focal volume. Laser light propagates as Gaussian beams and the minimum waists of the beams may not be at same position as the intersection point of the beams (Durst and Stevenson, 1977, Hanson, 1973). If the waists of the beams are not at the intersection point, the fringes will be curved, the fringe spacing, d_f , will not be constant, and broadening of the Doppler signal will occur. The broadening was estimated to be 0.1% and will add to the rms turbulence. This apparent turbulence will only be important in the free stream above the layer. The gradient in the fringe spacing is too small to produce any discernible error in the mean velocity measurement.

Velocity gradient broadening. Gradient broadening due to velocity gradients in the finite sized focal volume can result in errors in the calculation of the mean and rms velocities. For individual realizations, Kreid (1974) approximated the error in the mean velocity to,

$$\bar{u} - u_a = \frac{1}{8} b_y^2 u'' + \frac{1}{4} \frac{b_y^2}{u_a} u'^2 + \dots \quad 2.11$$

where \bar{u} is the measured mean, u_a is the actual mean, and b_y is the probe volume diameter in the gradient direction, y . The gradients u' and u'' are evaluated with respect to y in the center of the probe volume.

For the streamwise velocity, at any given distance downstream of the step, the maximum gradient will occur in the center of the shear layer. The velocity variation is linear and only the second term of equation 2.11 will be important. The most severe gradients are near

the edge of the step and are maximized at the highest inlet velocity ($U_0 = 22 \text{ M/s}$).

For example, when $U_0 = 22 \text{ M/s}$ at 0.5 step heights downstream, the maximum gradient in the layer was $1.3 \times 10^4 / \text{s}$. The probe volume has a diameter of 96 microns in the direction of the gradient. A mean velocity of 10 M/s will be 0.4% in error. The gradients downstream of this region were much less. At one step height downstream, a gradient of $4.5 \times 10^3 / \text{s}$ was typical which gives a 0.05% error at a local velocity of 10 M/s.

Curvature effects are important at the edge of the shear layer. The strongest curvature will be at the edge of the boundary layer at separation. The maximum effect of the first term of Eqn. 2.11 can be estimated there. The boundary layer profile is laminar (See Section 3.1). From a Blasius fit of the boundary layer at the highest Reynolds number ($Re_H = 3.7 \times 10^4$, $U_0 = 22.2 \text{ M/s}$, $u_a = 20 \text{ M/s}$) the maximum curvature is $-4.6 \times 10^7 / (\text{Ms})$ where $u' = 1.8 \times 10^4 / \text{s}$. This will produce a 0.1% error in the mean velocity for the worst case.

The rms turbulence will also be affected by gradient broadening. Following Durst et al (1976), one assumes that the variation of the velocity in the probe volume can be expanded into a Taylor series. Since the laser beam has a Gaussian intensity profile, the velocity variation is weighted by a Gaussian probability function. The rms turbulence is then,

$$\frac{1}{(u - u_a)^2}^{\frac{1}{2}} = \left[\frac{1}{4} b_x^2 u'^2 + \frac{3}{64} b_y^4 u''^2 + \dots \right]^{\frac{1}{2}} \quad 2.12$$

The curvature term is small throughout the flow field. However, the

first term in Eqn. 2.12 is important in the boundary layer at separation and in the shear layer. The gradient broadening was subtracted in the boundary layer by calculating u' from the \bar{u} -velocity data. A polynomial fit of three neighboring velocity points was used to determine the gradient. The maximum gradient broadening in the boundary layer ranged from $u_{\text{rms}}/U_0 = 0.04$ to 0.07 for the three Reynolds numbers studied. This amounted to about half of the turbulence measured in the boundary layer.

Calculating u' directly from the data added noise to the turbulence intensity measurements. Therefore in the shear layer, the \bar{u} -velocity data was fit with an error function by a least squares fit routine. The gradient was calculated from the error function fit and the broadening was removed. The maximum correction in the shear layer was about $u_{\text{rms}}/U_0 = 0.03, 0.02, 0.005$ for $x/H = 0.5, 1, 2$, respectively.

The skewness and flatness factors which are the third and fourth moments of the velocity PDF were also determined in the shear layer. Gradient broadening will also effect their evaluation. Again expanding the velocity in the probe volume into a Taylor series and averaging over a Gaussian probability one finds the skewness broadening is given by,

$$\overline{(u - u_a)^3} = \frac{9}{32} b_y^4 u'^2 u'' + \frac{15}{512} b_y^6 u''^3 + \dots \quad 2.13$$

and the flatness broadening is given by,

$$\overline{(u - u_a)^4} = \frac{3}{16} b_y^4 u'^4 + \frac{45}{128} b_y^6 u'^2 u''^2 + \frac{105}{4096} b_y^8 u''^4 + \dots \quad 2.14$$

Both terms in the skewness broadening were found to be negligible. The first term in the flatness broadening is not negligible. However if one normalizes the flatness factor by the uncorrected rms turbulence, the broadening due to the first term is removed. The rest of the terms in the flatness broadening are insignificant.

Velocity biasing. In turbulent flows, McLaughlin and Tiederman (1973) first recognized that the mean and rms velocity averages will be biased because at higher velocities more fluid and hence more particles are convected through the focal volume than at lower velocities. Time average computations proposed by Dimotakis (1976) to circumvent the McLaughlin-Tiederman bias in high data rate regions has been presented in Section 2.5.4. The time weighted averages are correct for regions where the data rate is high. In the low data rate regions where time averages are no longer valid, simultaneous measurements of at least two and sometimes three components of the velocity must be made to properly correct for the biasing (Dimotakis, 1976). A single component LDV system was employed, prohibiting this type of correction. In the low data rate regions, the numerical averages (Equations 2.7 and 2.8) were reported without corrections.

Bragg cell biasing. Velocity biasing is also caused by frequency shifting. The fringes move at a constant velocity and the number of realizations per particle will depend on the velocity of the particle (Meyers and Clemmons, 1979). In the limit, a stationary particle in the focal volume will produce an infinite number of realizations.

This velocity biasing effect will serve to cancel the McLaughlin-Tiederman bias. The importance of velocity biasing in the low data rate regions can be partially checked by examining the symmetry of the velocity PDFs which were stored at each measurement location.

Particle Considerations. The ability of the particles to follow the flow is an important consideration. The upper limit on the particle size is determined by the particle inertia and the lower limit by Brownian motion, molecular slip, and the particle scattering cross section. The particle concentration must not be too high to affect the flow. Also the size distribution must be narrow since the velocity lag is dependent on the particle size.

The cyclone particle generators using 0.05 micron alumina particles produced a particle diameter of about 0.2 microns (See Section 2.5.6). Mazumder and Kirsch (1975) set the lower limit of particle diameter determined by molecular slip at 0.1 microns. Brownian motion need only be considered for very low velocity (≤ 0.05 M/s) laminar flows (Durst et al, 1976). The particles were large enough to produce data rates up to 10 kHz in the free stream. Thus the particle size was not too small.

The particle concentration was about 1×10^{10} /M³ in the free stream. This represents an average separation distance of 2000 diameters for 0.2 micron particles, causing a negligible effect on the flow.

The upper limit on the particle size is determined by the required frequency response. The particles need to follow flow oscillations in the LaGrangian (moving) frame rather than the Eulerian (laboratory) frame which relaxes the size limitations considerably.

Using the particle flow solution by Hjalmfelt and Mockros (1966), Durst et al (1976) calculated the frequency response for various types of particles in both air flows and flames. Their calculations indicate that alumina particles 0.4 microns in diameter will follow flow oscillations (in the Eulerian frame) up to 10 kHz with 1% velocity lag in room temperature air flows. Particles of 0.8 micron size will provide the same performance in flames. Thus 0.2 micron particles used here will have a frequency response in excess of 10 kHz.

The size distribution of the alumina particles was not measured. The boundaries of the particle size PDF were determined by the initial particle size (0.05 micron) and the fringe spacing (3.1 micron). Thus realizations could only occur from particles ranging from 0.05 to 1.5 microns. Mazumder and Kirsch (1975) noted that the velocity lag varies with the size distribution and a wide distribution of particles might broaden the Doppler frequency. This may occur for highly accelerating flows with low turbulence levels. The flow field behind the rearward-facing step had turbulence levels exceeding 4% everywhere and turbulence levels greater than 50% in the shear layer. The large particle velocity lag was at most 2% and would tend to narrow the Doppler spectrum due to the low frequency response of the larger particles. This is clear from the effect of threshold setting on the turbulence level shown in Figure 2.15. As the threshold setting is increased, only the larger particles are validated, and the turbulence level decreases.

Combustion effects. Use of LDV in a combusting medium generates new sources of imprecision. Temperature and concentration variations

lead to index of refraction variations that cause movement and dispersion of the laser light. The probe volume position fluctuates and the beams may be deflected such that they no longer cross. Propagation of the Gaussian beams through the index of refraction inhomogeneities increases the waist diameter, distorts the fringes, and broadens the Doppler signal. These problems and others associated with combustion systems have been discussed by Self and Whitelaw (1976) and to some extent by Durst et al (1976).

Beam deflections and the ensuing beam uncrossings did not appear to be a problem in the two-dimensional combustor. The data rates for isothermal and reactive flows were essentially the same. The light deflections in the schlieren system (Figure 2.6) indicate that beam deflections of the order of 0.2 mm could have taken place in the burning shear layer. Deflections of this magnitude would certainly result in some signal dropout. However, the probability of such beam uncrossings must be small because no significant signal loss was recorded.

Durst and Kleine (1973) reported velocity biasing due to particle density variations in combusting flows. The high temperature, low density regions contain lower particle densities than the unburned regions. Uncorrected averages will be biased toward the velocity in the cooler turbulent eddies. At high data rates this bias was corrected by storage of the velocity-time record and time averaging (Equation 2.9 and 2.10). At low data rates, this biasing added additional uncertainty to the numerical averages (Equations 2.7 and 2.8).

Durst and Kleine (1973) also studied the effect of metal oxide

particles on the flame velocity. They found no significant change in the flame velocity in a premixed, stoichiometric, natural gas flame when using MgO particles at a concentration of $2 \times 10^{10} / \text{M}^3$. Thus the alumina particles used in this experiment at a maximum concentration of $1 \times 10^{10} / \text{M}^3$ had no influence on the combustion process.

Table 2.1 Combuster Data Record

Input Computer Terminal	{	(TA,PA)	Ambient air temperature and pressure
		(TT,PT)	Test section temperature and pressure
		(TF,PF)	Fuel rotometer temperature and pressure transducer setting
		(TS,PS,YS)	LDV seeder rotometer temperature, pressure, and displacement
		(TN,DN)	Main air nozzle temperatures and diameters
Desired Conditions	{	(Uo)	Reference velocity
		(Phi)	Equivalence ratio
Output Settings	{	(PN1,PN2)	Main air nozzle transducer settings
		(YF)	Fuel rotometer displacement
Output Conditions	{	(MA)	Main air mass flow rate
		(MAT)	Total air mass flow rate
		(MF)	Fuel mass flow rate

Table 2.2 Schlieren Optics Specifications

Camera	Test section view	X_1 (mm)	$X_2=f_1$ (mm)	θ_1 (deg)	θ_2 (deg)
Movie	Full	220	120	3.2	3.8
Movie	Enlarged	285	254	3.2	3.8
Movie	Super enlarged	165	365	3.2	3.8
Still	Full	120	1000	3.2	3.7

Table 2.3 LDV Data Record

Computer
Access:

Parallel
Line
Interface

[Burst counter range (4-7)
Comparator setting (5/8)
Comparator accuracy (2)

Computer
Terminal

[Record length (2048)
Fringe spacing (3.114 microns)
Bragg cell shift (0.01 - 10 Mhz)
Probe location (X,Y,Z)

Parallel
Line
Interface

[Burst period Data Period
 --- ---
 --- ---
 --- ---
 (x 2048 points)

ORIGINAL PAGE IS
OF POOR QUALITY

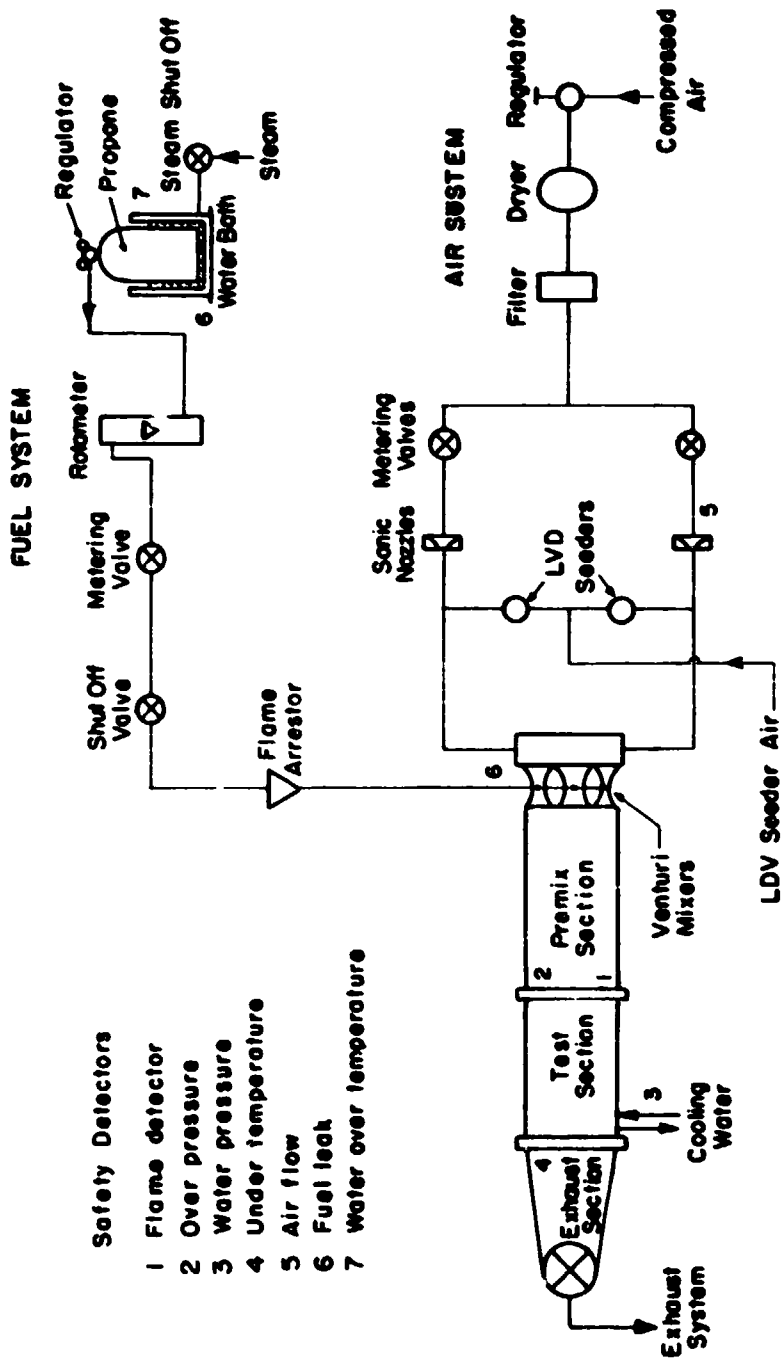


Figure 2.1 Two-dimensional combustor facility.

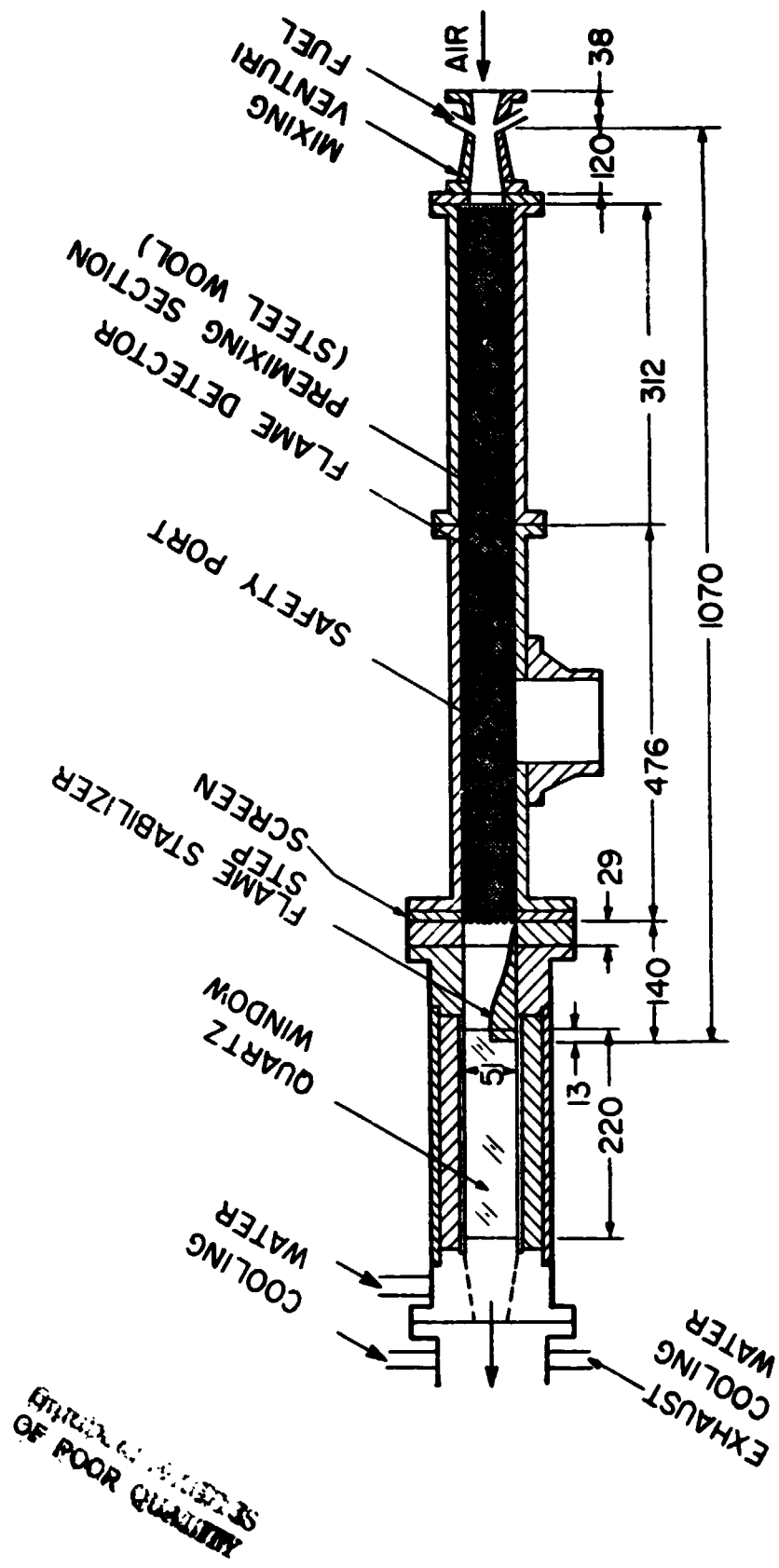


Figure 2.2 Cross section of the two-dimensional combustor (all dimensions in mm).

ORIGINAL PAGE IS
OF POOR QUALITY,

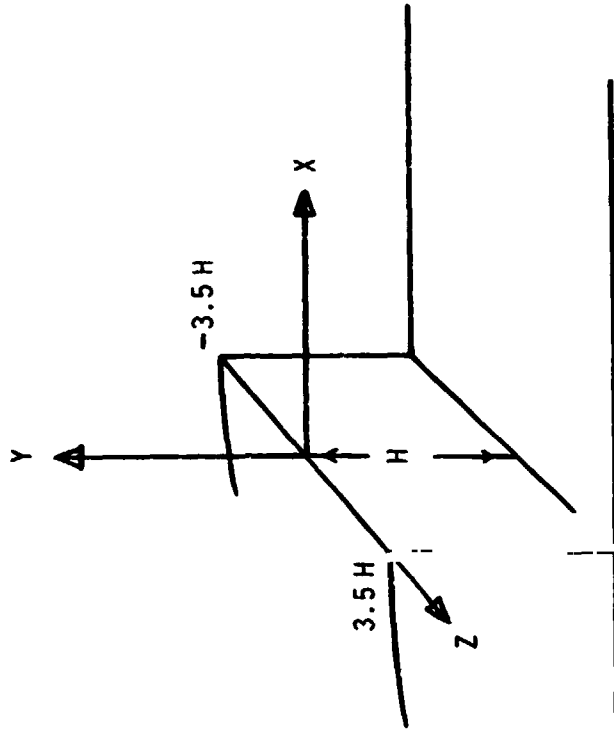


Figure 2.3 The two-dimensional combustor coordinate system.

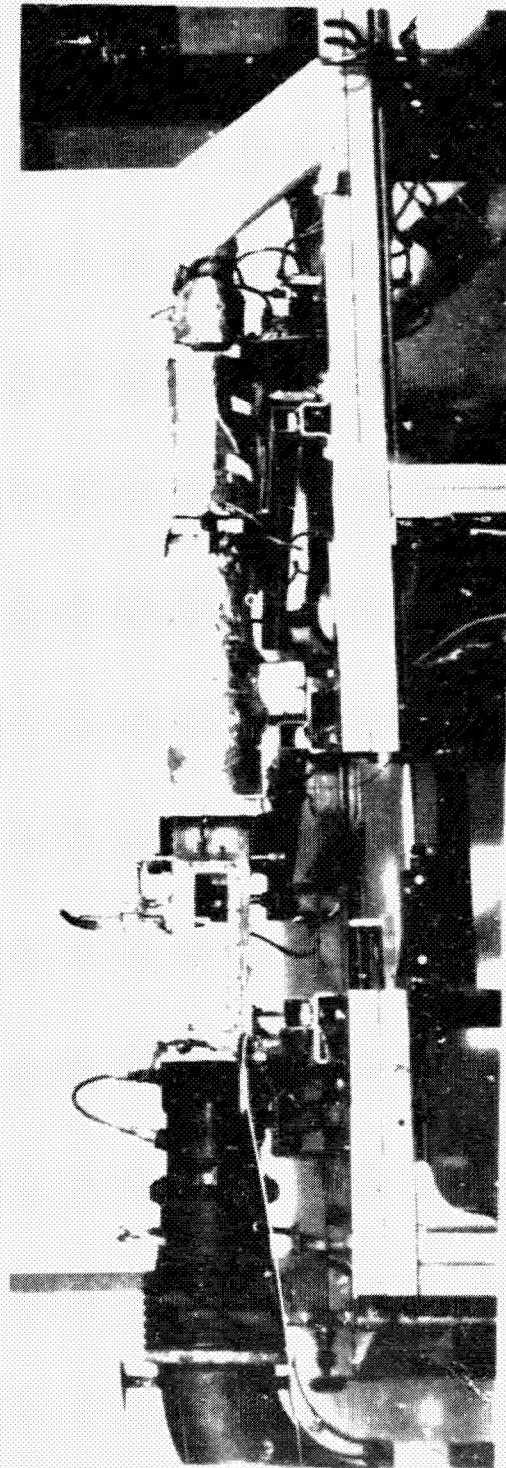


Figure 2.4 The two-dimensional combustor.

ORIGINAL SOURCE
OF PGR

ORIGINAL PAGE IS
OF POOR QUALITY

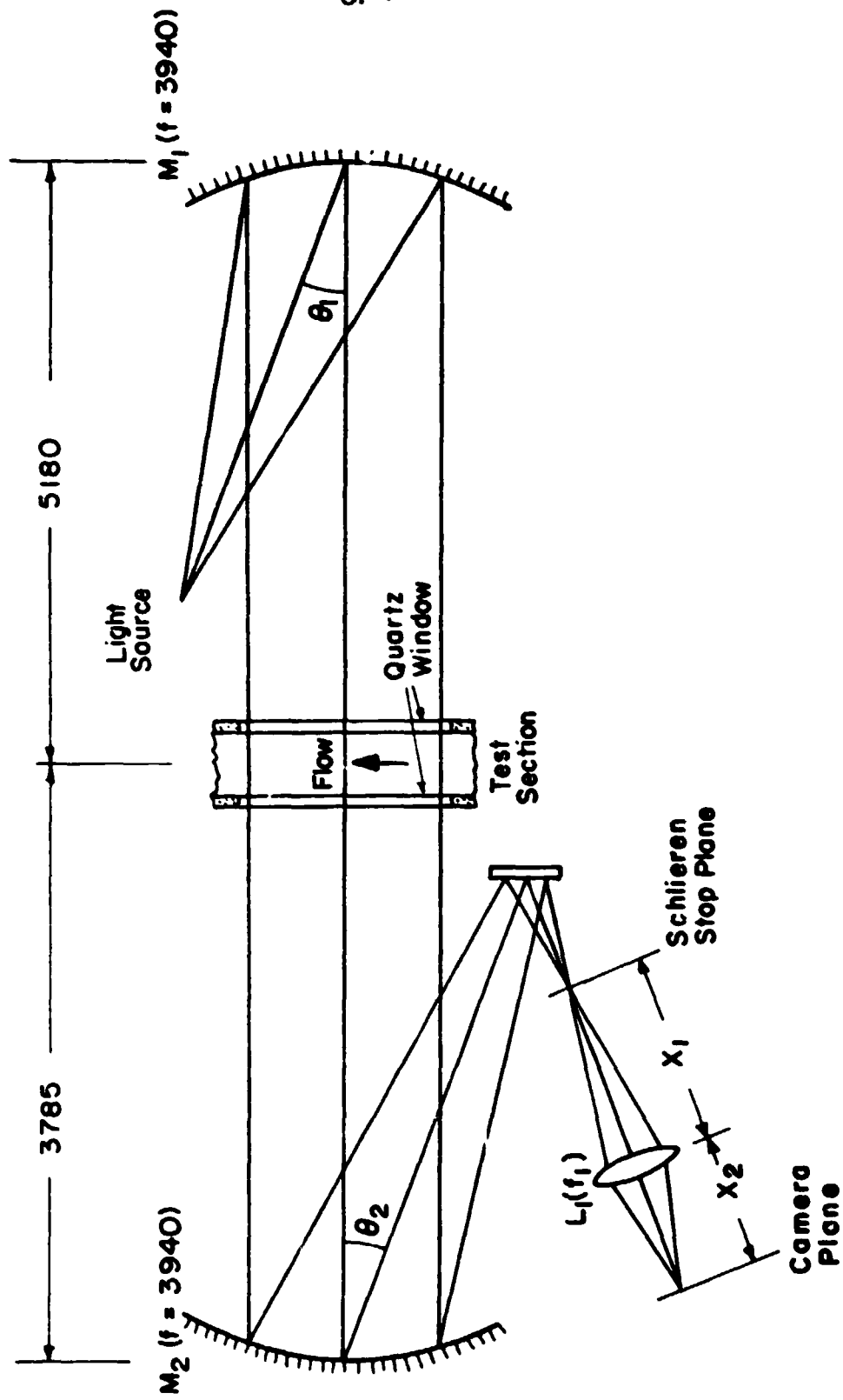


Figure 2.5 Schlieren optical layout (dimensions in mm).

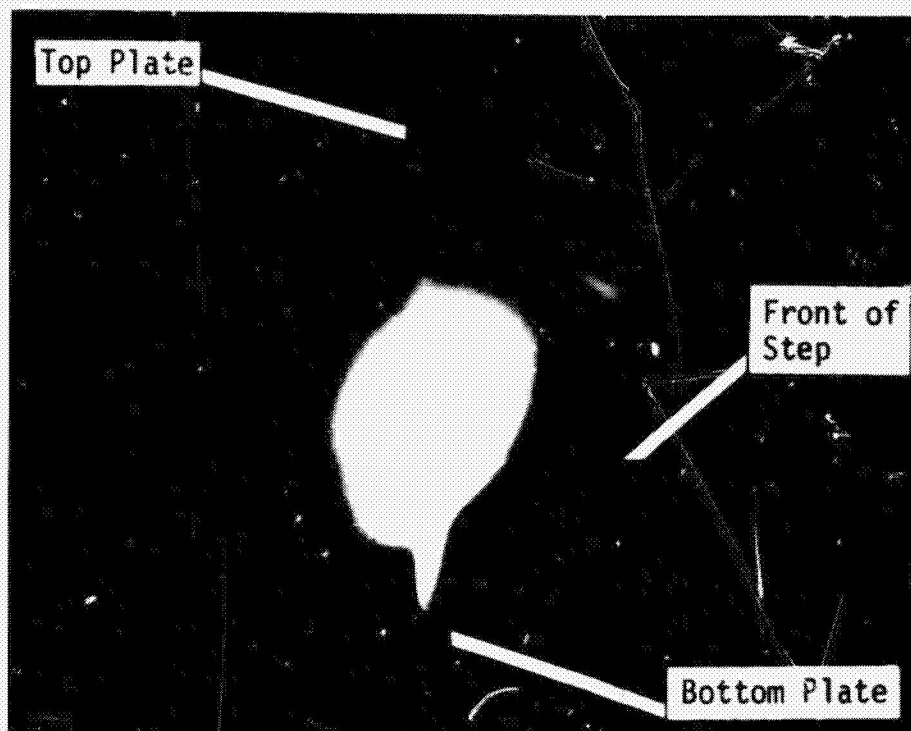


Figure 2.6 Polar diagram of schlieren deflections.

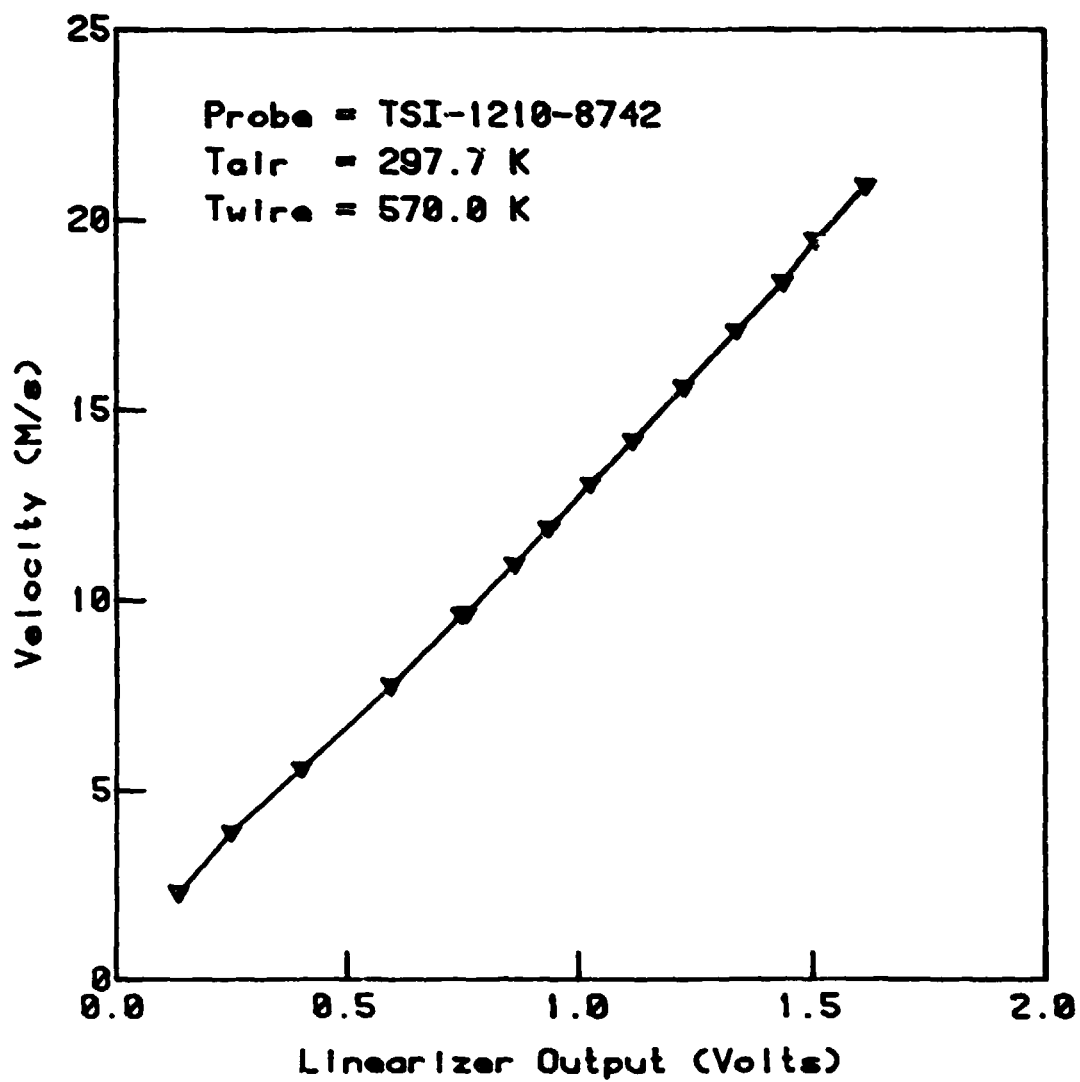


Figure 2.7 Hot wire calibration curve.

OF POOR QUALITY

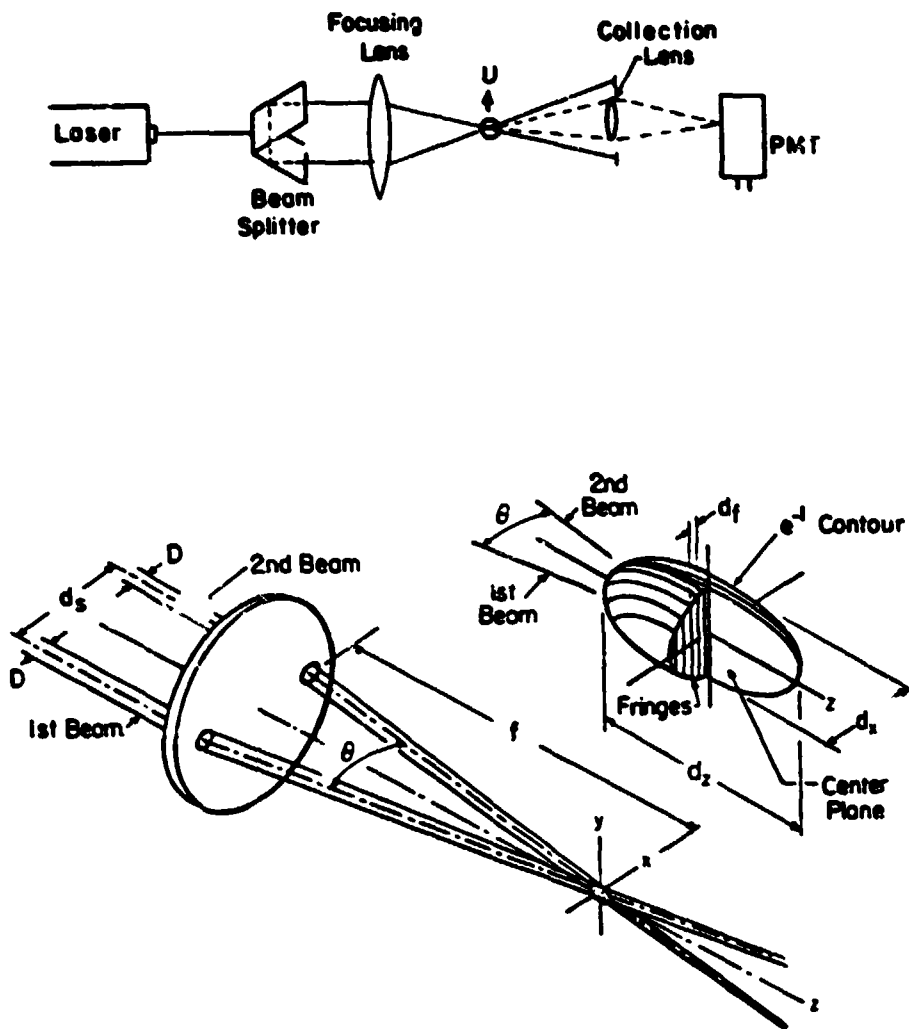


Figure 2.8 Typical LDV dual beam optics.

OF POOR QUALITY

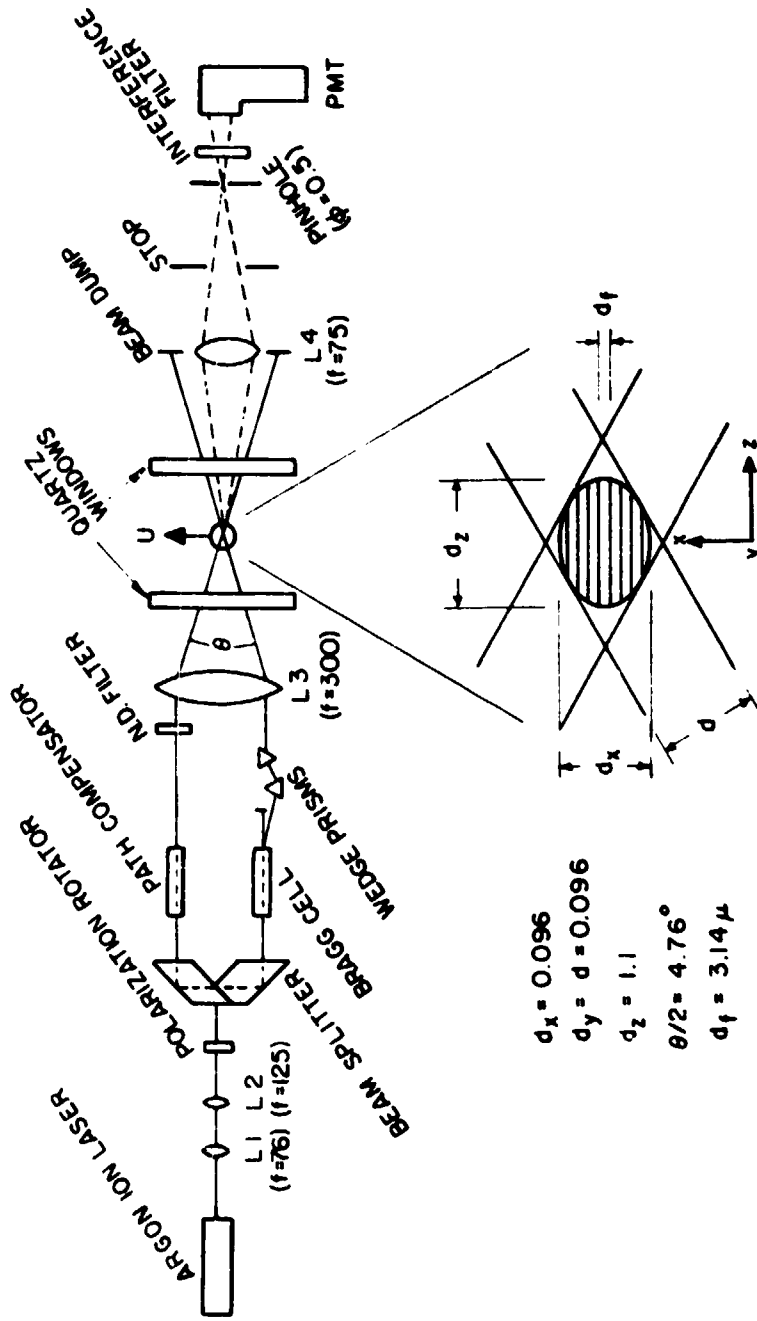


Figure 2.9 Two-dimensional combustor LDV optics.

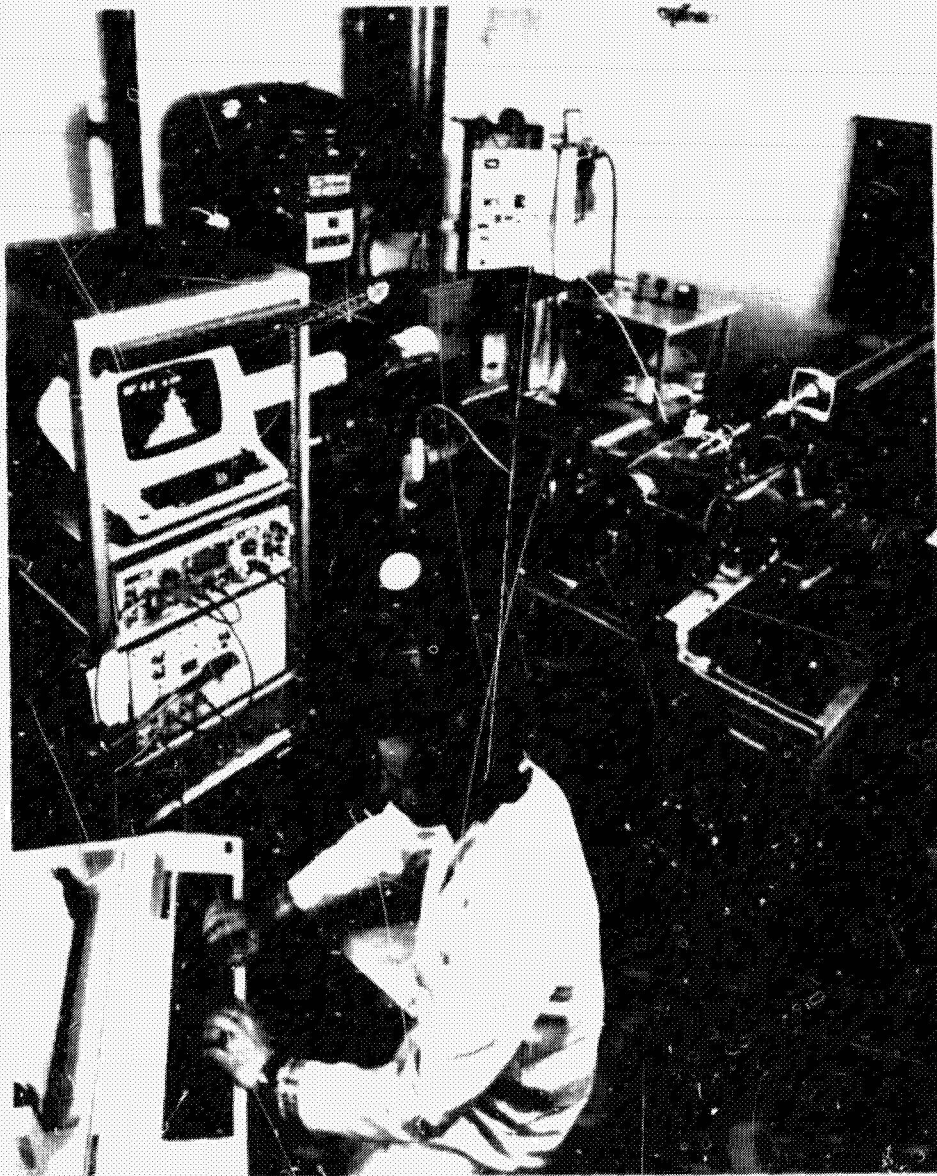


Figure 2.10 LDV data acquisition in the two-dimensional combustor facility.

ORIGINAL PAGE IS
OF POOR QUALITY

ORIGINAL PAGE IS
OF POOR QUALITY

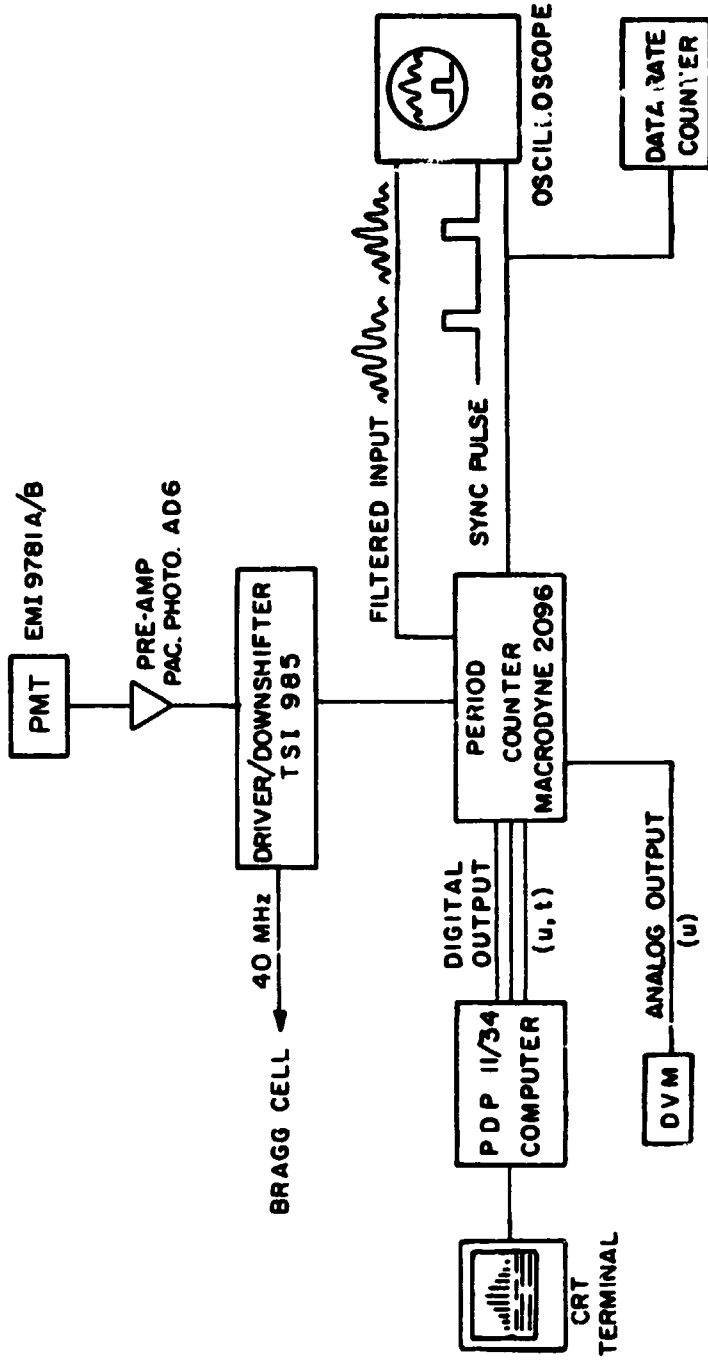
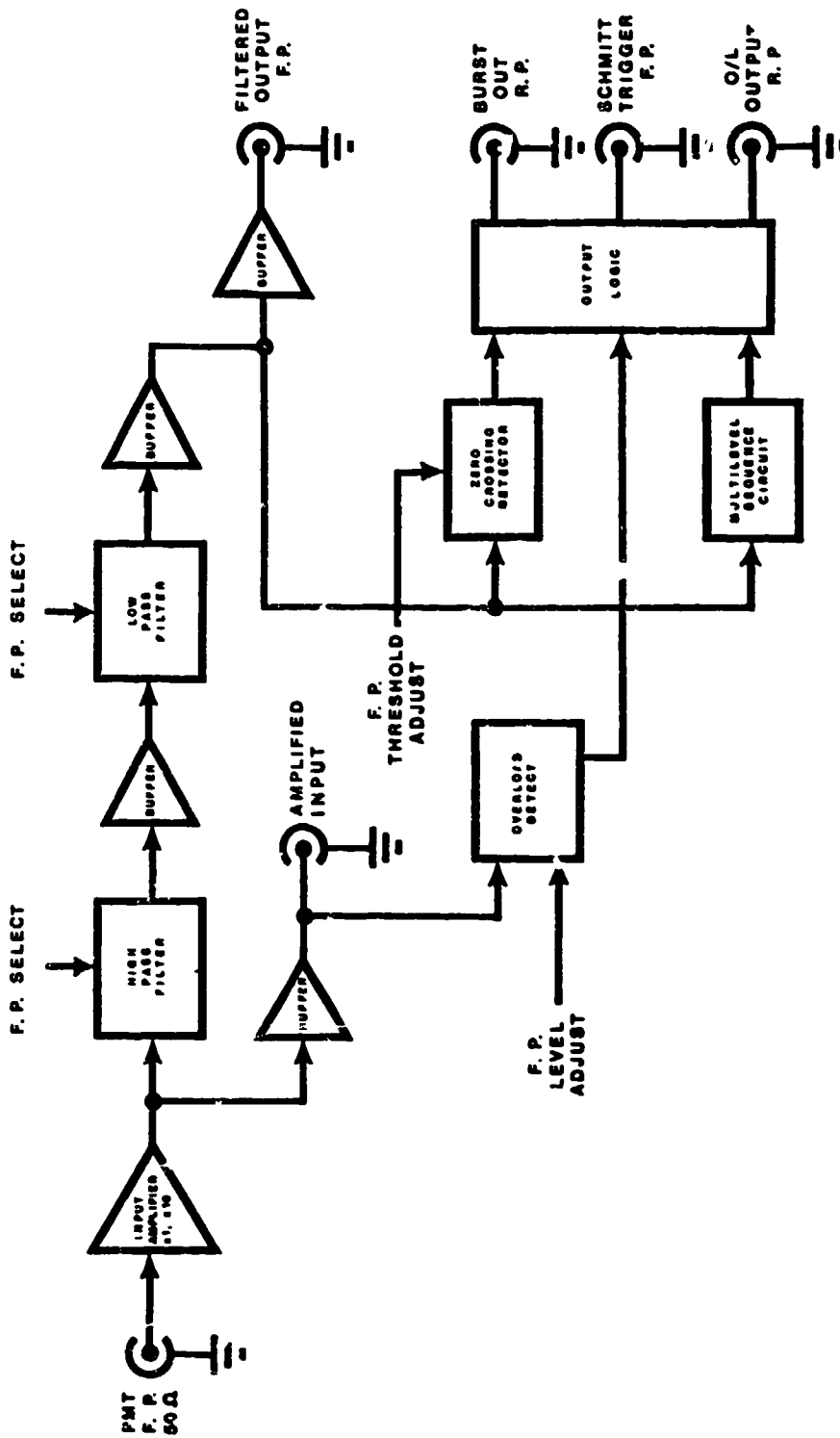


Figure 2.11 LDV signal processing system.



FED MC FILE 2096-2 BLOCK DIAGRAM

Figure 2.12 Macrodyne counter front end detector.
(Photo courtesy of Macrodyne, Inc., Rotterdam, N.Y.)

ORIGINAL RESULTS
OF FOUR QUANTY

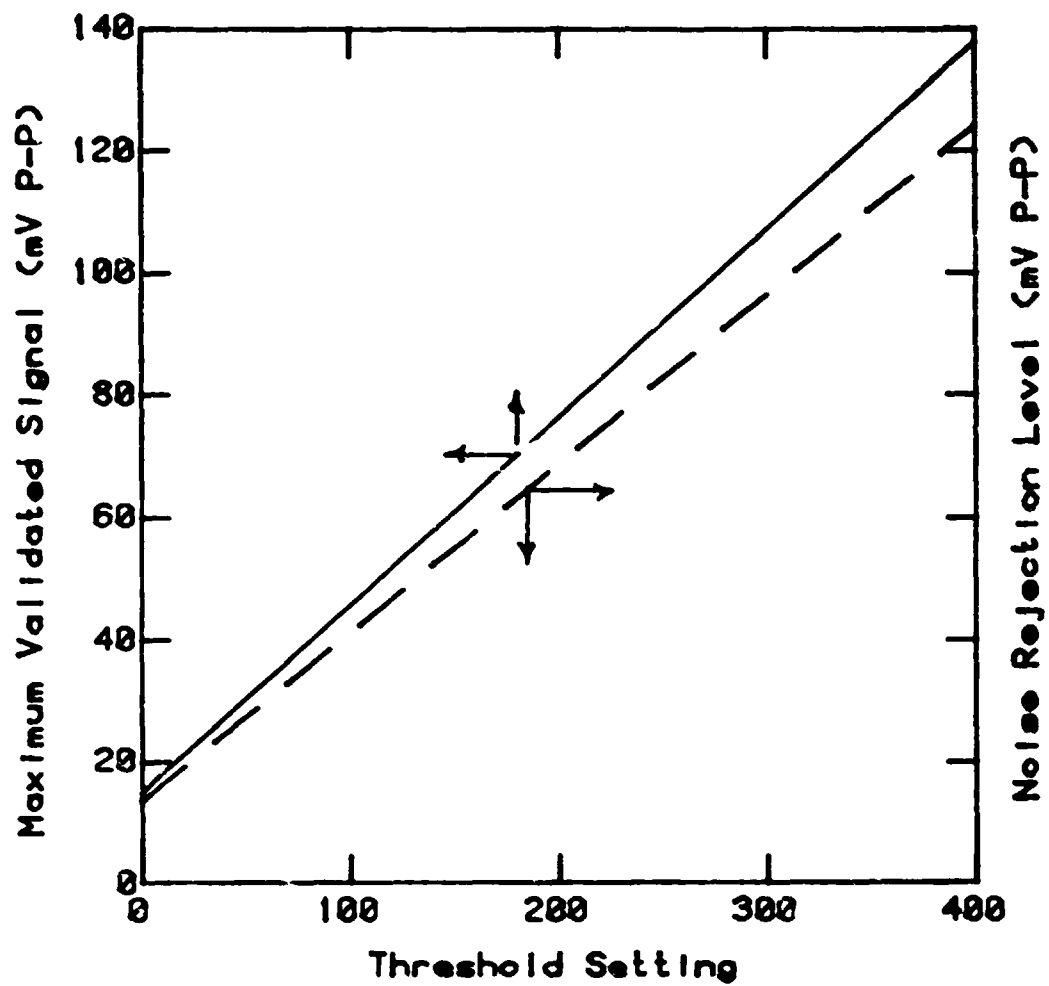


Figure 2.14 LDV noise rejection - Macrodyne counter threshold setting calibration.

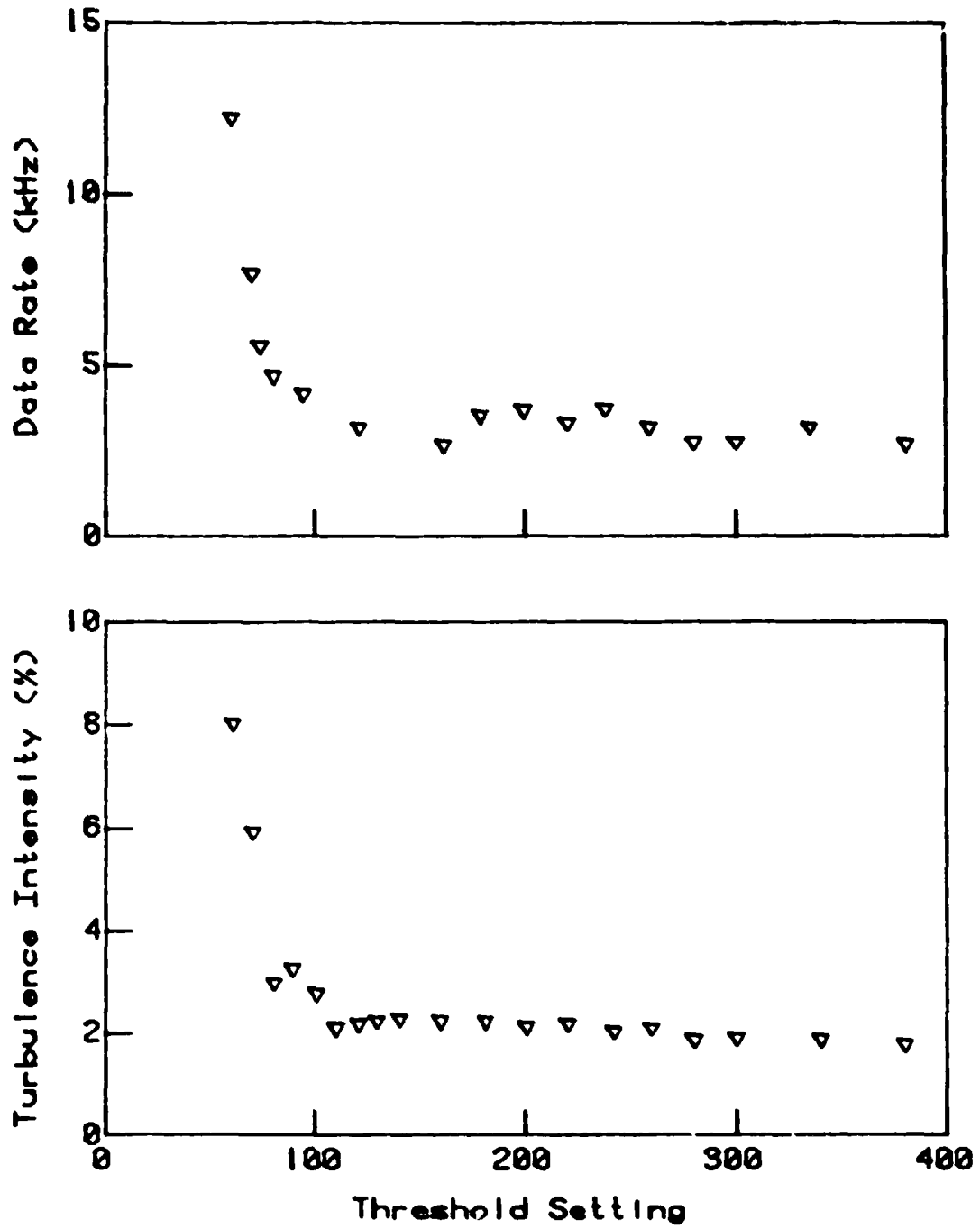


Figure 2.15 Variation of turbulence intensity and data rate with Macrodyne threshold setting.

ORIGINAL FIGURE IS
OF POOR QUALITY

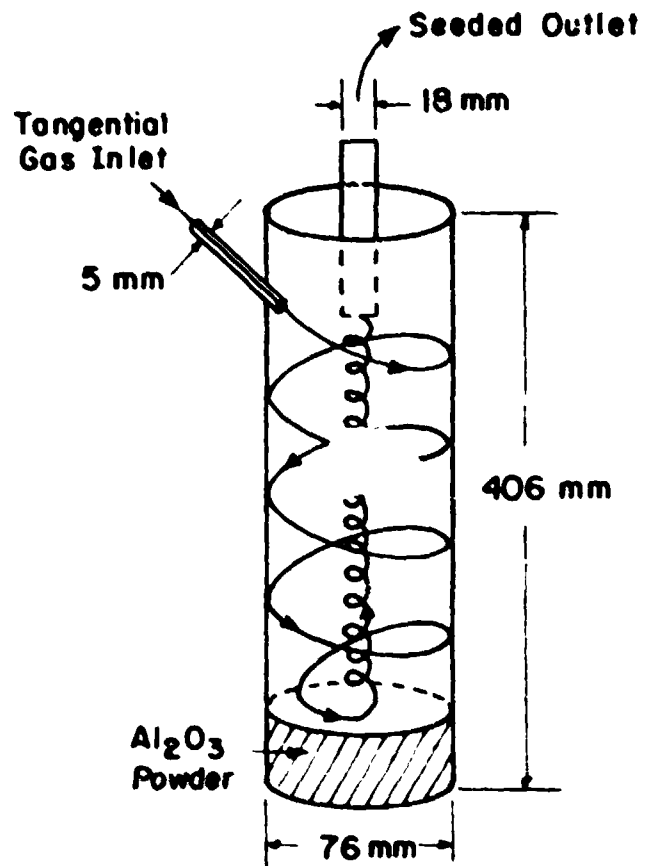


Figure 2.16 LDV cyclone particle seeders.

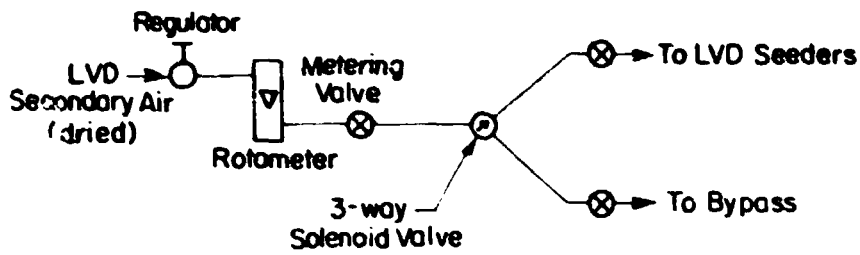


Figure 2.17a LDV seeder air supply.

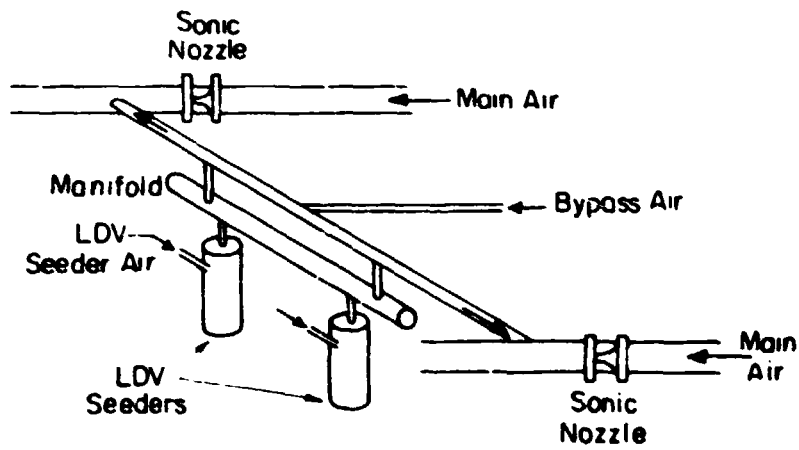


Figure 2.17b LDV seeder layout.

Chapter 3

RESULTS AND DISCUSSION

Three Reynolds number conditions ($Re_H = 1.5 \times 10^4$, 2.2×10^4 , 3.7×10^4) are studied for both reacting and non-reacting flow. The step height is fixed at 25 mm. In the reacting flow premixed propane-air is burned at an equivalence ratio of 0.57. The Reynolds number limits are determined by the stable burning modes of the combustor. All the inlet conditions are at room temperature.

Complete profiles of the mean and rms averages of the u-velocity component are recorded for each flow condition. The velocity PDF is stored at most locations. The reacting flows are visualized with high speed schlieren photography. Measurements of the v-velocity component are made for one Reynolds number ($Re_H = 2.2 \times 10^4$). Finally, the frequency spectra of the v-component velocity are obtained to assess the local large scale structure passing frequency at two inlet Reynolds numbers ($Re_H = 1.5 \times 10^4$, 2.2×10^4).

3.1 Initial Conditions

The state of the entry flow can have substantial effects on the behavior of mixing layers and reattaching flows. The condition of the boundary layer at separation can affect the shear layer's virtual origin, initial breakdown, growth rate, reattachment point, and turbulence development (see Bradshaw, 1966, Browand and Latigo, 1978, Batt, 1975, and Eaton, 1980a). Other variables such as test section geometry (Dimotakis and Brown, 1976), and free stream turbulence (Chandrsuda et al, 1978) can also be important. In rearward-facing step flows, the major scaling parameters assessing the state of the

boundary layer are the momentum thickness Reynolds number, $U_0\theta/\nu$, the boundary layer thickness, δ/H , and possibly the shape factor, $H_{12} = \delta^*/\theta$. Here δ is the 99% boundary layer thickness. The displacement and momentum thicknesses are δ^* and θ , respectively.

Birch (1977, 1980) suggests that the plane mixing layer flow becomes independent of the initial conditions at very high Reynolds number ($Re > 2 \times 10^6$). Most investigations in mixing layers and backward-facing step flows are well below this value and initial conditions are important. The effect of the state of the boundary layer (laminar or turbulent) on the shear layer growth and development for $Re < 2 \times 10^6$ is still not well understood. Batt (1975) and Wagnanski and Fielder (1970) report an increase in the growth rate when the boundary layer is tripped and Browand and Latigo (1978) report a decrease. In this study the maximum Reynolds number, Re_x , before curvature effects become large is 2×10^5 making the documentation of the initial conditions important.

The entry velocity profiles on the centerline for the three Reynolds numbers studied are shown in Figures 3.1, 3.2, and 3.3. These are numerical averages of the velocity. The time integrated averages are identical except near the step wall where the data rates are too low for the time averages to be meaningful. The inlet velocity is flat to $\pm 5\%$ of the average freestream velocity. The variations in the mean velocity are due to the small contraction ratio (2:1) and nonuniformities in the steel wool packing. Integration of the centerline profiles yields mass flowrates that are 2% - 3% lower than the flowmeter measurements. The free stream turbulence levels are about 2% for isothermal flow and 3% for reacting flow. The noise level

for the turbulence intensity measurements in the reacting flow is higher.

Hot wire anemometry measurements of the entry velocity profile are made to check the LDV operation. Velocity profiles for non-reacting flow measured by both techniques are shown in Figure 3.4. The agreement between the measurements for the three entrance Reynolds numbers varies from 0.3% to 2%. This is within the accuracy of the measurements which is 1.5% for hot wire and 0.4% for the LDV (see Chapter 2).

The boundary layer for the low Reynolds number case is plotted against the Blasius profile for $\phi = 0$ and 0.57 in Figure 3.5. The mean velocities follow the Blasius profile and the shape factor of the profiles is the Blasius value ($H_{12} = 2.6$). The turbulence levels are corrected for gradient broadening (see Section 2.5.7) which is significant in the boundary layer. The correction is proportional to the velocity gradient (Eqn. 2.12) which is not a smooth varying function and the noise level of u_{rms} is increased. The turbulence level is high in the boundary layer (~4%) but flat. The heat transfer back to the step in the reacting flows did not alter the boundary layer significantly. The medium and high Reynolds number flows are shown in Figures 3.6 and 3.7. The medium and high Reynolds number velocity profiles depart from the Blasius values but the shape factors of 2.5 and 2.4 are still much larger than the turbulent value of 1.3. The turbulence levels increase in the boundary layer for the higher Reynolds number flows.

The boundary layer parameters are summarized in Table 3.1 for all the run conditions. The influence of combustion on the boundary layer

state is minimal. Under all conditions the turbulence levels in the boundary layer are high (4 - 8%) yet the velocity profiles are basically laminar. This boundary layer state is similar to the tripped layer reported by Batt (1975). He used a wire trip producing high turbulence levels with a Blasius profile. Here imperfections in the profiled step (probably at the leading edge) might have tripped the boundary layer. The momentum thickness Reynolds numbers are around the critical value of 160 but are well below the transitional value of 390. The boundary layer never becomes fully turbulent. The condition of the boundary layer for all three Reynolds numbers is best described as "transitional".

The initial boundary layer state can also have important effects on the stabilization of the reacting shear layer. Figure 3.8 shows an enlargement of the mixing layers for the reacting flows. The dark object protruding from the top is the ignitor. The schlieren sensitivity is minimized in Figure 3.8b so that only the flame is shown. The flame stabilizes in the boundary layer just before separation. With too large a boundary layer the flame could propagate upstream causing flashback. At low flow rates ($Re_H < 1.5 \times 10^4$) the ignition point of the flame is found to wander in the boundary layer causing a low frequency flapping of the reacting layer. As the boundary layer becomes thinner, the ignition point of the flame must move downstream, and the flame could destabilize and blow off.

Hot wire spectra of the rms streamwise velocity component in the entry region were taken for the non-reacting flow. In the study by Ganji and Sawyer (1980), the premix section had no packing or screens. The hot wire spectra revealed many resonant peaks from

acoustic waves in the tunnel (see Figure 3.9). These "tuned" flow oscillations could trigger instabilities in the shear layer. Installation of screens and packing in the premix section (Chapter 2) eliminated this resonant turbulence. The hot wire spectra in the entrance flow for this study is given in Figure 3.10. The spectra is smooth and void of acoustic resonances. As will be seen later, under combustion the LDV rms velocity spectra exhibit some resonant peaks due to acoustic waves in the test section. It will be shown that they are not of sufficient magnitude to affect the layer.

3.2 Shear Layer Development

The rearward-facing step flow develops initially very much like a free shear layer with zero velocity on one side (half jet mixing layer). Before curvature effects become large ($\delta_w/R \ll 1$, where R is the radius of curvature of the dividing streamline) the growth rate and velocity profiles are similar to the half jet (Eaton and Johnston, 1980a). Unlike the half jet flows, the upper velocity, U_1 , does vary slightly with x and more importantly the velocity in the recirculation zone is not zero. Since the mixing layer growth rates are dependent on the velocity difference across the layer, one would expect an effect on the growth rate. Turbulence levels in the recirculation zone are also much higher than the half jet mixing layer. The influence of these higher turbulence levels in the recirculation zone on the turbulence development of the mixing layer are not well understood (Eaton and Johnston, 1980a).

As the layer continues to grow, curvature effects become large and the analogy to a mixing layer no longer applies. The layer curves down toward the wall and eventually impinges on the wall at the

reattachment point. The shear layer behind a rearward-facing step is often called a "reattaching" shear layer. The recirculation zone size depends to a great extent on the rate of growth of the reattaching shear layer into the recirculation zone. The growth of the upper boundary of the shear layer will determine the rate of entrainment of fresh fluid into the layer.

As in mixing layers, the turbulent structure of the reattaching shear layer is determined by the formation and development of large scale structures. The initial laminar shear layer breaks down from a Kelvin-Helmholtz instability (Sherman, 1976) and the large scale structures form. These large scale structures are primarily two-dimensional (Brown and Roshko, 1974) and grow by fluid entrainment and coalescence (Winant and Browand, 1974). The growth of the large scale structures mark the boundaries of the reattaching shear layer. Their growth effects the recirculation zone size and the rate of spread of the upper boundary of the shear layer into the free stream. The turbulence in the layer results from the passing of these two-dimensional structures which contain a smaller scale, three-dimensional framework (Breidenthal, 1978, Konrad, 1976).

In the reacting layer, the incoming flow is premixed reactants. The flame is stabilized at the edge of the step. Near the step, the reactants and hot products mix in a laminar layer and burn. Once the eddies form the burning takes place in the two-dimensional structures (Ganji and Sawyer, 1980). The eddies fold in reactants and hot products as they roll downstream. As we will see, the heat expansion causes the shear layer defined by the mean velocity field to be shifted downward and the recirculation size shortened. The large

scale structures react and expand above the shear layer. The density above the shear layer is lowered as the upper flame boundary extends beyond the boundary of the shear layer. The coalescence rate of the structures is also lowered by heat release. These and other effects of reaction on the reattaching shear layer will be detailed in the next sections.

3.3 Mean Velocity Flow Field

3.3.1 Streamwise Velocity Flow Field. A typical streamwise velocity profile is shown in Figure 3.11. Both the numerical and integrated mean values are plotted along with the corresponding data rate. Above the shear layer the data rates are fairly high and the two means are identical. In the shear layer there are some differences between the two means but the values match closely. Only in the recirculation zone, where the data rates are typically low, are significant differences apparent. Clearly the time integrated values are suspect here since the data rates are too low to truly follow the flow. The numerical averages are also subject to velocity biasing errors in this turbulent region. In all the mean profiles the only significant departure of the two mean values occurs in the recirculation zone. Since the numerical means are more appropriate for this region, and the two values are the same elsewhere, all the velocity profiles reported will be numerical averages.

Integration of the centerline velocity profiles in the isothermal flow yield mass flow rate estimates that range from 8% to 25% below the flowmeter measurements. Off-center profile measurements indicate that this flow deficit can be attributed to lower recirculation rates near the side walls. A centerline profile at $x/H = 3$ is compared to an

off-center profile taken halfway between the wall and centerline ($z/H = 1.8$) in Figure 3.12a. The average bulk velocity in the profiles is 20% low in the centerline and 3% low at $z/H = 1.8$. The lower recirculation rates near the wall increase the average bulk velocity. The velocity in the recirculation zone ($y/H = -0.67$) for the same x position is shown in Figure 3.12b confirming that the recirculation rates are lower away from the centerline. A complete volume integral involving sequential scans across the tunnel is not made but the lower recirculation rate near the wall can easily account for the flow deficit on the centerline.

The aspect ratio (tunnel width to step height) is 6.9. According to de Brederode and Bradshaw (1972) at aspect ratios greater than 10 three-dimensional effects are small. Here three-dimensional effects are not negligible, but as seen from Figure 3.12 the flow is still predominantly two-dimensional. Schlieren pictures of the reacting shear layer (Figures 3.8 and 3.40) also demonstrate the two-dimensionality of the flow.

The centerline streamwise velocity profiles of the reacting and non-reacting flow at the three entrance Reynolds numbers studied are shown in Figures 3.13 through 3.15. The dashed line shown in the reacting flow indicates the upper edge of the flame boundary measured from long exposure schlieren photographs such as Figure 3.44. The flame boundary is well above the shear layer given by the mean velocity profiles.

For the non-reacting flow the position of the zero streamline is determined from the centerline profile by integrating from the top wall. The results indicate that curvature effects do not become

important until $x/H = 4$ or $x/x_R = 0.6$, where x_R is the reattachment length. This is consistent with the results of Eaton and Johnston (1980a). The three-dimensional effects are too strong to give accurate quantitative data of the zero streamline position.

The maximum reverse velocity at each x position in the recirculation zone for the non-reacting flow is given in Figure 3.16a. The maximum reverse velocity is $0.33U_0$ which is higher than reported by other researchers. A review of backward-facing step flows by Eaton and Johnston (1980b) reports a typical reverse velocity of $0.25U_0$. The higher value is probably due to the low aspect ratio of this flow. As seen in Figure 3.12b the reverse velocity is $0.3U_0$ on the centerline and decreases to $0.2U_0$ at $z/H = 2.0$.

The maximum reverse velocities of the reacting flow are higher due to heat release. The maximum reverse velocities range from $0.39U_0$ to $0.48U_0$ for the three Reynolds numbers. Since the flow is not adiabatic these depend on the amount of heat loss to the walls.

The streamwise volumetric recirculation at each x position is plotted in Figure 3.17. For the isothermal flow, the reversed flow per unit width is $0.16U_0H$. This compares with a value of $0.08U_0H$ reported by Moss and Baker (1980). Moss and Baker's reverse velocity ($0.2U_0$) is lower than normal ($0.25U_0$) which accounts for some of the difference. Most of the difference is a result of the low aspect ratio used here which causes three-dimensionalities in the recirculation zone. For example, the centerline profile in Figure 3.12a has a recirculation rate of $0.17U_0H$ and the off-center profile has a value of $0.09U_0H$.

The volumetric recirculation of the reacting flows are given in

Figure 3.17b for completeness. The mass recirculation rates are dependent on the local density. The volumetric recirculation values are higher at $0.16U_0H$ to $0.24U_0H$. The volumetric recirculation in the x direction drops off decisively to zero between $x/H = 4$ and 5 illustrating the shorter recirculation zone size for the reacting flow.

From the mean velocity profiles information on the shear layer boundaries, growth rate, fluid entrainment, and reattachment length can be deduced. The effects of the heat of reaction on these reattaching shear layer properties will be considered in the following sections.

3.3.2 Growth Rate. To quantify the growth of the layer one must consider its boundaries. One measure of the thickness of the layer is the vorticity thickness, δ_ω , given by,

$$\delta_\omega = \Delta U / \left(\frac{\partial u}{\partial y} \Big|_{\max} \right) \quad 3.1$$

where

$$\Delta U = U_1 - U_2 \quad 3.2$$

and U_1 and U_2 are the velocities in the upper and lower streams, respectively, and $\partial U / \partial y|_{\max}$ is the maximum slope in the layer. In half jet mixing layers ($U_2 = 0$) ΔU is identical to U_1 . In the rearward-facing step configuration U_2 varies due to the non-zero velocity in the recirculation zone (See Figure 3.16a). Here δ_ω is estimated using the maximum velocity in the recirculation zone near

the shear layer edge.

The vorticity thickness for the isothermal flows are plotted in Figure 3.18. The two lower Reynolds number flows grow more slowly initially. The lower Reynolds number shear layers are initially more stable and the layer breaks down farther downstream. This is confirmed by eddy formation position measurements made previously from schlieren observations (Ganji and Sawyer, 1980). All the growth curves have a fairly linear region and then drop off when wall interactions become important. Only the high Reynolds number data exhibit a truly linear growth and is fit with a slope of $\delta'_\omega = 0.28$ in Figure 3.18. Estimates of the growth rate in the linear region vary from 0.27 to 0.29. These growth rates are much higher than those reported previously (Batt, 1977). Only the growth rates of tripped half jet mixing layers (Batt, 1975, Wagnanski and Fiedler, 1970) approach this value ($\delta'_\omega = 0.23$). The excess growth can be traced to the non-zero velocities in the recirculation zone. Mixing layers at high Reynolds numbers are self similar and their growth rate is dependent on the parameters,

$$s = \rho_2 / \rho_1 \quad 3.3$$

$$\lambda = (U_1 - U_2) / (U_1 + U_2) \quad 3.4$$

For isothermal flow ($s = 1$) the growth rate is linearly dependent on λ according to (Brown and Roshko, 1974):

$$\delta_{\omega}' = 0.18 \lambda \quad 3.5$$

For half jet mixing layers ($\lambda = 1$) the growth rate is 0.18. In rearward-facing step flows the negative velocity in the recirculation zone causes the value of λ to vary between 1.2 and 2.0 in the mixing layer region of the flow. An average value of 1.6 could easily account for high growth rate reported ($\delta_{\omega}' = 0.28$).

Half jet flows with tripped boundary layers grow slower at first and then overshoot the asymptotic growth rate (Husain and Hussain, 1979, Birch, 1980). Overall the growth rate is high in the developing region and causes the virtual origin to appear downstream of the separation point. The isothermal mixing layers seem to follow this pattern here. All the virtual origins are downstream of the step which suggests that the boundary layer is indeed tripped. The virtual origin for flow developing from a laminar boundary layer is upstream of the separation point (Husain and Hussain, 1979, Birch, 1980). According to Birch (1980) at high enough Reynolds numbers ($Re_x > 2 \times 10^6$) the growth rate reaches an asymptotic value and the virtual origin is downstream of the separation point regardless of the initial conditions. The mixing layer region of the flow in this work is clearly not well developed. The Reynolds number is too low ($Re_x|_{\max} = 2 \times 10^5$), the growth rates are high, and the virtual origin is downstream of the step.

The vorticity thickness plots of the reacting layers are shown in Figure 3.19. The initial growth of the layer is delayed significantly over the isothermal case. Again this is a local Reynolds number

effect. The Reynolds number varies like $T^{-3/2}$. From thermocouple measurements in the layer (Ganji and Sawyer, 1980), there is about a factor of 4 increase in temperature, which results in an eightfold decrease in Reynolds number. Thus the shear layer breakdown is delayed over the nonreacting case, reducing the growth rate.

At $x/H = 2$, the vorticity thickness for $Re_H = 1.5 \times 10^4$ is much greater. This might be due, in part, to a low frequency instability of the reacting layer mentioned earlier. The ignition point which is located just upstream of the step expansion (see Figure 3.8b) is unstable for $Re_H \ll 1.5 \times 10^4$. The ignition point oscillates in the streamwise direction causing the whole reacting layer to flap at a low frequency. At $Re_H = 1.5 \times 10^4$, the layer seems stable but under close observation some movement of the ignition point is detected. This might result in a very slight low frequency flapping of the layer which gives the large value of δ_ω at $x/H = 2$.

Estimates of the growth rate of the reacting shear layers range from $\delta_\omega' = 0.26$ to 0.29 . Again only at $Re_H = 3.7 \times 10^4$ is the growth truly linear and the data is fit with $\delta_\omega' = 0.29$. A direct comparison of the vorticity thickness plots for the high Reynolds number case is shown in Figure 3.20. Initially the growth of the reacting layer is suppressed due to the lower Reynolds number in the reacting layer. Surprisingly, the growth rates of the two layers are nearly identical at 0.23 for the non-reacting layer and 0.29 for the reacting layer.

Brown and Roshko (1974) reported a 25% reduction in the growth rate for a half jet mixing layer ($\lambda = 1$) at high density differences ($\rho_2/\rho_1 = 1/7$). No reduction in growth rate was found in this study. This suggests that the effect of the density difference across the

layer is counter balanced by the effect of heat release and volumetric expansion.

For a reacting shear layer, the vorticity thickness is only one measure of the layer boundary. The vorticity thickness defines the region of strong momentum transfer but the regions of combustion and heat transfer can be quite different. As seen in Figures 3.13 - 3.15 the flame boundary is well above the edge of the shear layer. Schlieren pictures such as in Figure 3.40 show reaction taking place in the large scale structures propagating inside and above the shear layer. Thus combustion is not confined to the shear layer defined by the mean velocity flow field.

3.3.3 Entrainment. From Figure 3.13 - 3.15, it is evident that the reacting shear layer undergoes a shift downward into the recirculation zone. The upper boundary of the shear layer is plotted in Figure 3.21a for $Re_H = 3.7 \times 10^4$. The growth of the reattaching shear layer into the upper stream is dramatically reduced. All the reacting layers showed this behavior.

In the reacting flow, the flame extends above the upper boundary of the shear layer and the density above the shear layer is decreased. The upper stream velocity $U_1(x)$ is nearly identical for both the reacting and non-reacting flow. Thus the mass rate of entrainment of fluid from the upper stream into the shear layer is reduced for the reacting flow

3.3.4 Reattachment. The reattachment length is defined as the point in the separation region where there is no net flow reversal. The reattachment length is determined to a large extent by the growth of the mixing layer into the recirculation zone. The lower boundary

of the layer is difficult to assess due to the very gradual decrease in the slope. The center of the shear layer can be defined by the position where the velocity equals $\Delta U/2$. The centerline position of the reacting and non-reacting layers at $Re_H = 3.7 \times 10^4$ is presented in Figure 3.21b. The center of the reacting layer is shifted downward propagating toward the wall more rapidly.

The reattachment lengths can be estimated from the velocity flow field plots given in Figures 3.13 - 3.15. They are summarized in Table 3.2. Velocity profiles are taken in increments of H near the reattachment point making the values accurate to $\pm 0.5 H$. The reattachment lengths for the reacting layers are reduced by 20 - 30%. This affirms the general shift of the layer toward the lower wall.

The momentum thickness Reynolds number of the boundary layer at separation, Re_θ , is also given in Table 3.2. The reattachment length varies with the boundary layer state and therefore Re_θ . Eaton and Johnston (1980a) report a strong increase of x_R with Re_θ for a laminar boundary layer. The reattachment length peaks for a transitional boundary layer and decreases slightly to an asymptotic level for a turbulent boundary layer state. The reattachment lengths do not show a strong dependence on Re_θ here indicating that the boundary layer state is transitional.

The reattachment lengths for the reacting flow increase about 20% as Re increases. For a laminar boundary layer state at separation, Eaton and Johnston (1980a) found a 30% increase in the reattachment length with Re_θ . The high temperature in the initial shear layer region decreases the local Reynolds number and could have placed the functional variation of x_R in the laminar region.

With combustion, the reattachment lengths are shorter and the flow relaxes back to channel flow sooner (Figures 3.13 - 3.15). According to Bradshaw and Wong (1972), in isothermal flows complete relaxation occurs at a distance of 30 times the shear layer thickness at reattachment. This corresponds to 50 step heights downstream for this flow.

3.3.5 Transverse Velocity Flow Field. The transverse velocity, \bar{v} , is plotted for $Re_H = 2.2 \times 10^4$ in Figure 3.22. The isothermal profiles vary with y as expected. Initially the dividing streamline is parallel to the y axis, and \bar{v} is zero in the center of the layer. As the dividing streamline curves downward, \bar{v} is no longer perpendicular to it and there is a net downward flow in the center of the layer. In the mixing layer \bar{v} varies like y^2 near the centerline as predicted by a simple gradient diffusion model (Görtler, 1942).

The reacting layer profiles have a similar behavior except that heat release and density variation cause the profiles to be asymmetric. The center of the shear layer undergoes a shift downward consistent with the \bar{u} results.

3.4 Turbulence Development

3.4.1 Turbulence Intensity. The streamwise turbulence intensity profiles for are shown in Figures 3.23 - 3.25. In both the reacting and non-reacting flows the regions of high turbulence are bounded by the shear layer, broadening as the shear layer grows downstream. Near reattachment, the turbulence levels decrease and the turbulence profiles begin to take on the characteristics of turbulent channel flow. In the reacting flow, the reattachment lengths are shorter and more of the post-reattachment region can be seen. The downstream

profiles are ragged indicating that the 2048 point records are insufficient to produce a true average.

Gradient broadening of the turbulence intensity is removed in the shear layer (See Section 2.5.7). The velocity gradient is calculated by fitting an error function to the mean velocity data in the shear layer with a least squares fit routine. The broadening in the top and bottom boundary layers is not removed. The maximum correction in the shear layer at $|\partial u/\partial y|_{\max}$ is about $u_{\text{rms}}/U_0 = 0.03, 0.02, 0.005$ for $x/H = 0.5, 1.0, 2.0$, respectively.

The exact position of the maximum value of the turbulent intensity is difficult to determine but the general trend can be seen. In the isothermal flow the position of the maximum initially coincides with the centerline ($y/H = 0$). It then dips slightly toward the recirculation zone and rises back toward the centerline near reattachment. These same trends have been reported previously (Eaton and Johnston, 1980a). The reacting layer behaves the same way except the dip is much more dramatic. The maximum value follows the shifted shear approaching the bottom wall much more closely and then rises toward the centerline after reattachment.

The maximum turbulence value, $u_{\text{rms}}/U_0|_{\max}$, is plotted in Figure 3.26a for the non-reacting flow. The initial increase of the turbulence intensity is due to the formation of the large scale structures which form earlier for the high Reynolds number flows. The Kelvin-Helmholtz instability that results in the formation of the large structures is dependent on a critical Reynolds number based on x . The instability occurs first for the high Reynolds number flows. These results are confirmed by eddy formation position data deduced

from schlieren observations made in non-reacting flow by Ganji and Sawyer (1980). They found that the eddies formed at $x/H = 0.63$, 0.55 , 0.47 for $Re_H = 1.5 \times 10^4$, 2.2×10^4 , and 3.7×10^4 , respectively.

For all the non-reacting experiments, the turbulence intensity reaches a maximum 1 to 2 step heights before reattachment. The turbulence level for the low and medium Reynolds number cases gradually increase to this maximum. This monotonic increase of the turbulent intensity to a maximum 1 to 2 step heights before reattachment has been found in other rearward-facing step experiments such as Kim et al (1978), Eaton and Johnston (1980a), and Etheridge and Kemp (1978). A complete summary of backward-facing step turbulence levels has been given by Eaton and Johnston (1980b).

The turbulence development of the high Reynolds number flow does not reach a single peak. The levels peak early at $x/H = 0.5$ and then decay and reach a second maximum at $x/H = 4$. Bradshaw (1966) found a similar behavior in a mixing layer formed at the edge of a nozzle. Both the turbulent shear stress and u-turbulent intensity were double-peaked for the mixing layer formed from a laminar boundary layer. Bradshaw suggests that this second maximum "marks the establishment of the shear-producing part of the turbulence spectrum". Examining the full turbulent profiles for $Re_H = 3.7 \times 10^4$ in Figure 3.25a, one notices that the profiles at $x/H = 1-3$ are flat topped and even double-peaked in the shear layer. The rest of the data is single-peaked which make these profiles suspect. Thus more measurements need to be made to confirm whether the turbulence growth is double-peaked and whether the second peak marks the emergence of fully three-dimensional flow.

The maximum turbulence level in the shear layer for all three Reynolds numbers is $u_{rms}/U_0 = 0.28$. Turbulence intensity values of 0.21 are more typical for backward-facing step flows (Eaton and Johnston 1980a). A number of conditions lead to this high level. The freestream turbulence is high at 2-3%. Also the aspect ratio is low (6.9) which causes significant three-dimensional effects and results in a high reverse velocity. The velocity difference across the layer, ΔU , is $1.33U_0$ as opposed to $1.2U_0$ for typical flows. Renormalizing the turbulence levels would decrease the maximums by 10%.

Until curvature effects are strong, the shear layer formed at a rearward-facing step is very similar to a plane mixing layer. However, the maximum turbulence level found in backward-facing step flows ($u_{rms} = 0.21U_0$) is normally higher than plane mixing layers ($u_{rms} = 0.17U_0$, Batt, 1977). The higher turbulence levels for backward-facing steps is a result of the reentrainment of pressure driven, highly turbulent fluid into the recirculation zone (Bradshaw and Wong, 1972). For half jet mixing layers the fluid on one side is at rest and the turbulent intensities are normalized by the constant velocity difference across the layer $\Delta U = U_0$. In the backward-facing step flows ΔU is not constant and is typically $1.2U_0$ ($\Delta U = 1.3U_0$ in this experiment). Renormalizing by the local value of ΔU would decrease the turbulence levels. Not only is the fluid in the recirculation zone not at rest, but is highly turbulent ($u_{rms} = 0.1U_0$) which also increases the turbulence levels in the shear layer.

The turbulence levels for all three flows decrease rapidly 1-2 step heights before reattachment. This has been reported by other researchers (Eaton and Johnston, 1980a). The two explanations proposed

to explain this decrease are shear layer curvature and splitting of the eddies near reattachment (Eaton and Johnston, 1980a). Castro and Bradshaw (1976) found curvature in shear layers to be stabilizing and cause a rapid decay of turbulence. The curvature of the layer is strong in the reattachment region which decreases the turbulence levels. Bradshaw and Wong (1972) reported a splitting of the eddies near reattachment, calculating that the length scales decreased by a factor of two. These eddies produce most of the shear stress and their splitting results in a decrease of the turbulence near reattachment.

In this study, measurements of the eddy frequency (Section 3.5) show no reduction of the eddy wavelength in the reattachment region. The eddy structures as seen from the LDV and schlieren measurements maintain their integrity throughout the reattachment zone. Thus the primary mode for the turbulence decay is a result of the curvature of the shear layer.

The reacting flow (Figure 3.26b) has higher turbulent intensity values of 30-35% as a result of volumetric expansion in the layer. The data exhibits two separate growth and decay periods suggesting at least four mechanisms controlling the development of the turbulence. The first growth period is delayed over the isothermal flow as the large scale structures form later (Table 3.3). The subsequent turbulence decay is connected with the two-dimensional structures burning, coalescing, and growing as they are convected through the probe volume. The second growth region probably results from the introduction of small scale three-dimensional turbulence. Konrad (1976) found a three-dimensional instability in the large scale structures formed in a plane mixing layer that increased turbulent

mixing by 25%. Since the turbulent Schmidt number should be near unity this would also increase the turbulence intensity. For the three Reynolds numbers, the transition would occur at $x/H = 1.5 - 2.5$ for room temperature air. Heat release would delay the transition and the high turbulence in the boundary layer would tend to advance it. If the second growth period is due to Konrad's instability, the Reynolds number should affect its location. There is not enough data in Figure 3.26b to determine whether there is a Reynolds number effect. Again the turbulence decays as the curvature effects become strong, 1-2 step heights before reattachment.

The turbulence intensity profiles of the transverse velocity are given in Figure 3.27 for $Re_H = 2.2 \times 10^4$. The values of v_{rms} and u_{rms} are the same in the freestream but v_{rms} is much less nearly everywhere else. In the recirculation zone at $x/H = 2$ and 5, v_{rms} is as large as u_{rms} . The values of $v_{rms}/U_o|_{max}$ are given in Figure 3.26. The transverse turbulence does not grow significantly until well after the large structures are formed. The isothermal values are about 30% below the streamwise turbulence data but the maximum occur at the same position. These results are consistent with other backward-facing step data (i.e. Etheridge and Kemp, 1978, Kim, Kline, and Johnston, 1978). For the reacting flow at $x/H = 0.5$, the eddies have not formed yet and there is no clear maximum value of v_{rms} in the shear layer. The value of v_{rms}/U_o at the same y position as $u_{rms}/U_o|_{max}$ is given in Figure 3.26b. The downstream values of v_{rms} are similar to the streamwise data. The v_{rms} data at $x/H = 5$ which is about one step height beyond reattachment looks more developed than the u_{rms} data indicating that the reattachment affects v_{rms} more strongly.

3.4.2 Probability Density Functions. Typical PDFs of the streamwise velocity component for the isothermal layer are displayed in Figure 3.28. The probability density, P , on the vertical scale is unitless and defined such that the integral of $(P)d(U/U_0)$ is 1. The weighting factor used to correct the LDV counter biasing discussed in Section 2.5.4 is not exactly correct and the PDFs still have systematic noise. To correct this problem the PDFs of the Doppler burst period should be stored and the PDF of the velocity calculated with velocity intervals corresponding to unit increments of the digital burst period. All PDFs from counter processors will contain systematic noise independent of sample size unless PDFs are calculated in this fashion.

The positions of these Pdfs in the shear layer are indicated in Figure 3.29c. The skewness and flatness factors determined from the PDFs are displayed in Figures 3.29a and 3.29b. The skewness which is the third moment of the PDF indicates symmetry. The flatness factor or fourth moment describes how fast the distribution decreases in the wings. A Gaussian distribution has zero skewness and a flatness factor of 3. The PDFs above and below the shear layer are Gaussian ("a" and "f"). Near the edges of the shear layer (PDFs "b", "d", and "e") non-Gaussian behavior is seen. On the low velocity edge PDF "b" is positively skewed with a long tail on the high velocity side. PDFs "d" and "e" on the high velocity edge of the shear layer have tails on the low velocity side and are negatively skewed. The flatness factors are high at these positions as the distribution falls off more slowly than a Gaussian (>3). In the center of the layer (PDF "c") the turbulence is the highest but the distribution is Gaussian. All the

skewness and flatness factors are normalized by the turbulence intensity calculated from the PDFs.

The PDFs shown here are not corrected for velocity gradient broadening which will increase the width of the PDFs near the step. Gradient broadening will also affect the skewness and flatness factors and its contribution to these factors is given by Equations 2.13 and 2.14. Gradient broadening of the skewness is estimated from an error function fit of the \bar{u} -velocity data. The maximum contribution ($Re_H = 3.7 \times 10^4$, $x/H = 0.5$) is $\overline{u^3}/u_{rms}^3 = 0.04$ which is negligible. Gradient broadening of the flatness factor is removed by normalizing the flatness factor by the gradient broadened turbulence intensity. All the values of u_{rms} shown in this section are calculated from the PDFs and are gradient broadened near the step. The skewness is also normalized by this value of u_{rms} . In the center of the shear layer at $x/H = 0.5$, this causes a normalization error giving values of $\overline{u^3}$ which are smaller by factors of 1.8 to 4.1. Beyond one step height the normalization error is negligible. The normalization error near the step does not change the sign of $\overline{u^3}$ only its absolute magnitude. The character of the variation of the skewness in the layer is unchanged.

The non-Gaussian behavior of the turbulence near the edges of the shear layer in Figures 3.28 and 3.29 can be explained by considering the large scale structures. They form quasi-periodically at $x/H \cong 0.5$. The large structures intermittently grow to a sufficient size to affect the edges of the shear layer. When this happens they convect low velocity fluid to the upper edge ("d") and high velocity fluid to the lower edge ("b"). The velocity of the fluid converted by the large scale structures departs more radically from the mean

velocity than the velocity variation due to small scale turbulence and the tails are produced. The variation of skewness and flatness shown in Figures 3.29a and 3.29b is consistent with data in isothermal free shear layers (Spencer and Jones, 1971)

The skewness and flatness factors for the low Reynolds number flows are given in Figures 3.30 and 3.31. The non-reacting flow is negatively skewed in the upper edge of the shear layer and positively skewed in the lower edge. This behavior maintains itself even after reattachment. The non-Gaussian behavior is much stronger in the upper part of the layer where the gradients are stronger and the turbulence is lower. The flatness factor in the high velocity edge is much greater than 3. The flatness factor in the recirculation zone is nearly Gaussian except near the step ($x/H < 1$).

The skewness of the turbulence in the reacting flow looks quite different at first. However there are similarities when one considers that the reacting layer is shifted downward well below the centerline of the test section. Examining the \bar{u} -velocity profiles in Figure 3.13b, the PDFs are positively skewed at the lower edge of the shear layer and negatively skewed near the upper edge as in the isothermal layer.

The non-Gaussian behavior for non-reacting and reacting flow are very similar at $x/H = 1$. For comparison the reacting flow PDFs are shown in Figure 3.32 at similar locations as given for the non-reacting PDFs in Figure 3.28. The position of the PDFs in the shear layer, the skewness and flatness factors, and the turbulence intensity are given in Figures 3.33a thru 3.33d. The variation of the skewness and flatness factors is the same as the non-reacting flow at

$x/H = 1$.

There are two major differences in the non-Gaussian behavior in the reacting flow. In Figure 3.30b, for $x/H > 1$, the skewness has a positive peak at the upper boundary of the shear layer given by the \bar{u} -velocity profiles. The negative peak in the skewness is slightly below this boundary. To illustrate this behavior, the PDFs and their moments are displayed in Figures 3.34 and 3.35. As before PDF "b" is skewed positively at the lower edge of the shear layer. However, just below the upper edge the skewness is negative ("c") and at the upper boundary the skewness is positive ("e").

The existence of this second positive peak is a result of combustion in the layer. As seen from schlieren observations, combustion occurs within the large scale structures as they convect downstream. The upper boundary on the growth of these large scale structures can be determined from long exposure schlieren photographs such as Figure 3.44. This boundary represents the farthest excursion of the eddies into the upper inviscid stream and is the edge of the flame. The boundary as seen in Figure 3.13 is above the shear layer given by the \bar{u} -velocity profiles. The expansion of the eddies due to reaction fills out the upper part of the shear layer and feeds the momentum transfer across the shear layer. At the same time the semi-periodic passing of the expanding fluid between the top of the shear layer and the upper flame boundary produces a high velocity tail on the PDFs (See Figure 3.34, PDF "c"). The positive peak occurs between the upper edge of the flame and the top of the shear layer (See Figures 3.30b, 3.34 and 3.35). Thus the second positive skewness peak results from the impelling effect of the large scale structures

expanding between the top of the shear layer and the upper boundary of the flame.

The flatness factor in the reacting layer is high from the top of the shear layer to the upper thermal boundary even though the skewness changes sign (Figure 3.31b). For example, PDF "d" in Figure 3.34 has nearly zero skewness but tails on both wings of the PDF produce a high flatness factor. At this position the large scale structures convect both high speed fluid from reaction and low speed fluid from the recirculation zone. Similar behavior in the skewness and flatness factors for reacting flow can be seen at the medium and high Reynolds numbers in Figures 3.36 and 3.37 except that the positive skewness peaks above the shear layer for the high Reynolds number flows are not as evident in the downstream positions.

The second major difference is near the step at $x/H = 0.5$. In all the reacting flows the skewness has negative peaks at both the lower and upper edges. The skewness has a positive peak near the center of the layer. This region is more clearly examined in Figures 3.38 and 3.39. Typical PDFs are given in Figure 3.38. At the lower edge of the layer ("b") the PDFs are negatively skewed. The PDFs are positively skewed just below the center of the layer ("d"), Gaussian in the center (between "d" and "e"), and negatively skewed near the top ("e"). The positively skewed PDFs near "d" are all bimodal. All PDFs at this location in the reacting flows are bimodal. Everywhere else the PDFs are single-peaked.

Two explanations for the double-peaked nature of the PDFs near the step can be given. The intermittent formation of the large scale structures due to the instability of the shear layer could cause a

bimodal PDF. The formation of the structures produces rapid burning, high local heat release, and expansion. The average velocity of this event would be higher than the velocity in the laminar layer when there is no breakdown.

Secondly, the bimodal behavior could be a result of low frequency flapping. As discussed earlier, the reacting layer flaps slightly at the low Reynolds number condition. Slight flapping of the thin shear layer at this position could produce a double-peaked velocity distribution. Since the bimodal PDFs are found for all three Reynolds numbers and from the schlieren movies there does not seem to be any flapping at the higher Reynolds numbers, the first explanation is more plausible.

3.5 Large Scale Structures

The presence of large scale structures in free shear layers and in reacting shear layers has been firmly established (Brown and Roshko, 1974, Ganji and Sawyer, 1980). The large scale structures form early in the shear layer from a Kelvin-Helmholtz instability (Sherman, 1976). The structures are two-dimensional in nature and grow by coalescence and entrainment as they are convected through the layer. For premixed combustion in the layer, the reaction occurs in the eddies as they entrain premixed reactants and hot products. Heat release expands the structures and contributes to the growth of the layer.

Since the large scale structures control to a great extent the turbulence structure, a major goal in this study is to assess the effect of combustion on their evolution. The large scale structures are analyzed with high speed schlieren photography and spectral

analysis of the LDV signal.

3.5.1 Schlieren Photographic Observations. Schlieren photographs of the reacting flow at the three entrance Reynolds numbers are shown in Figure 3.40. The exposure time varies from 49 to 74 μ s. The large scale structures are prominent throughout the flow field. The rod shaped object protruding from the top is the ignitor. The dark bands highlight the high temperature gradients due to combustion. The combustion is taking place in large scale structures forming near the step. The fluid above and below the layer is fairly isothermal.

The initial shear layer can be seen more clearly in Figure 3.8. The schlieren is desensitized in 3.8b and shows the point of ignition at the edge of the step. The large scale structures form as the initial shear layer breaks down. The structures grow by fluid entrainment, heat expansion, and coalescence.

The mechanism of coalescence is illustrated in Figure 3.41. The sequence of photographs are spaced 0.3 ms apart. The coalescence process which is the combining of two neighboring eddies is also called amalgamation or pairing. The pairing process is found in isothermal free shear layers (Winant and Browand, 1974) and in reacting shear layers (Ganji and Sawyer, 1980). The upstream eddy overtakes the downstream eddy and the two combine into one eddy with twice the original size. Brown and Roshko (1974) reported eddy pairing to be one of the major growth mechanisms in free shear layers.

At the high Reynolds number flow, the large scale structures do not appear to be as ordered as the low Reynolds number flow (Figures 3.8c and 3.42). This is probably due to three-dimensionalities in the breakdown of the layer near the step. For all the reacting flows the

flame appears to stabilize at more than one region on the step edge allowing the layer to break down at different times across the flow. The high Reynolds number flow seems more susceptible to this three-dimensional breakdown causing the blurred pictures in Figures 3.8c and 3.42.

The average shedding position is determined from the schlieren movies. Histograms of the shedding position (Figure 3.43) from movies at $Re_H = 1.5 \times 10^4$ and 2.2×10^4 are Gaussian. The shedding position decreases with Reynolds number as the shear layer is less stable at higher Reynolds numbers.

Long exposure photographs are taken to deduce the flame boundary. Figure 3.44 shows a schlieren photograph of the flame where the bright areas indicate high temperature gradients. The top edge is the flame boundary and is uppermost propagation of the large scale structures into the upper free stream. This boundary also represents the upper boundary of the thermal layer since the primary mode of heat transfer is convection of burning gases in the large scale structures.

The flame boundary of the three Reynolds number flows is shown in Figure 3.45. The vertical scale is greatly expanded to emphasize the differences in the spreading rates. The flame spread decreases for the higher Reynolds numbers since the stoichiometric ratio is constant ($\phi = 0.57$). The flame spread for the low Reynolds number flow is higher than one would expect from the Reynolds number decrease. Slight low frequency flapping is observed at this condition which results in the higher flame spread. No flapping is observed at the other conditions.

The average passing frequency of the eddies is measured at ~~the~~

different downstream positions. Using a motion analyzer a vertical line is positioned at a specified location on the movie frame. Each time an eddy passes the line, the frame number is recorded. The passing frequency is calculated as the inverse of the time between eddies. Histograms of the passing frequency are shown in Figure 3.47a and 3.48a. The histograms are positively skewed near the step and more Gaussian downstream. This passing frequency data is compared with the passing frequency determined from LDV spectra in the next section.

3.5.2 LDV Spectra. The frequency spectra of the vertical velocity component is recorded to measure the large scale passing frequency in the layer. The structures are most easily detected by positioning the LDV probe volume in the center of the shear layer and measuring the vertical velocity component. A spectrum taken in the isothermal layer is shown in Figure 3.46. The broad peak in the spectrum is generated by the large scale structure.

The LDV spectrum for the reacting flow at the same position (Figure 3.47b, $x/H = 2$) has a broad peak superimposed with narrow acoustic peaks. The evolution of the large scale structure in the reacting flow is more clearly revealed in Figure 3.49. A broad peak in the spectra is first seen at $x/H = 1$ and the peak decreases in frequency with downstream distance. The width of the broad peak is about the same as found in the non-reacting flow where no acoustic peaks are evident. Narrow peaks in the spectrum from acoustic resonances in the combustor are more pronounced near the step and increase in amplitude as x/H increases.

Acoustic resonances do not seem to affect the

development of the large scale structures. The broad peak corresponding to the large scale passing frequency appears at $x/H = 1$ and smoothly decreases in frequency through the layer. The broad peak is always much wider than the narrow acoustic peaks indicating that the large scale structures are never completely coupled with the acoustics. The acoustic modes are fixed in frequency throughout the layer.

When coupling of acoustics and the large scale development does occur, the effects are dramatic. Keller et al (1981) excited the reacting shear layer in this apparatus with a loud speaker. Using a driving frequency of 200 Hz at a relatively small power level, they were able to couple the large scale passing frequency with the acoustic frequency. High speed movies of the reacting shear layer disclosed that the large scale structures were completely coherent. A large increase of the growth rate took place when the eddy passing frequency matched the acoustic driving frequency. The structures had a constant wavelength beyond this point and no coalescence is observed. Coupling of acoustic perturbations and the large scale structure passing frequency has also been reported in mixing layers (Fielder et al, 1977). None of these coupling effects are observed here.

The eddy formation position, x_g/H , is estimated from the LDV spectra. The first appearance of a broad peak in the spectra is approximately the average eddy shedding position. The estimated values are given in Table 3.3 along with the more accurate schlieren determinations. Measurements of the LDV spectra are taken every 1/2 step height near the step and the shedding positions match within that uncertainty. Again the shedding position increases with decreasing

Reynolds number. In the reacting flow the local Reynolds number is decreased by a factor of eight from the fourfold increase in temperature. The decrease in Reynolds number increases x_g/H for the reacting flow.

The passing frequency from both the schlieren movies and LDV spectra are compared in Figures 3.47 and 3.48. Near the step for the medium Reynolds number flow (Figure 3.47) the schlieren measurements give a passing frequency 50% higher than the passing frequency measured from the LDV. At $x/H = 7$ the difference is still 35% (Figure 3.48). The Strouhal number, $Str_H = H\bar{f}/U_c$, is compared for the two measurements in Figure 3.50. The Strouhal number data from the schlieren movies does not have a similar shape for the two entrance Reynolds numbers and is consistently higher than the LDV data. Three-dimensional breakdown of the reacting layer probably causes some of the discrepancy. As mentioned before, the flame seems to stabilize at more than one location across the step. A close examination of the schlieren movies indicate that the layer breakdown is not always two-dimensional. Since the LDV measurements of the passing frequency are made at a single point, they are not effected by the three-dimensionalities. The second problem with the schlieren histograms is that they are not true spectra of the passing frequency. There is no correlation of motion with wavelengths longer than the distance between eddies. Thus the estimated passing frequency is higher than one determined from a true frequency analysis.

The Strouhal number, Str_H , for both non-reacting and reacting flow are plotted in Figure 3.51. The eddies in the reacting layer form later but at the same frequency, $Str_H = 2.0$, as the isothermal

flow. This suggests that the acoustic peaks which are visible only in the reacting flow do not affect the eddy formation frequency. The isothermal data appears to vary like a mixing layer $Str_H \sim 1/x$ between $x/H = 1 - 4$. Specifically the Strouhal number should be given by (Brown and Roshko, 1974),

$$Str_H = \frac{H f}{U_c} = \frac{\alpha H}{(x - x_0)} \quad 3.6$$

where x_0 is the virtual origin and α is a constant. In order to determine the virtual origin, Equation 3.6 is rearranged as,

$$\frac{U_c}{H f} = \frac{1}{\alpha} \left(\frac{x}{H} \right) - \frac{1}{\alpha} \left(\frac{x_0}{H} \right) \quad 3.7$$

The isothermal data is plotted in that form in Figure 3.52. The values of α and x_0 are determined from a least square fit of the data between $x/H = 1 - 4$. The growth rate of the shear layer (Figure 3.18) is only linear in that region. The virtual origin in Figure 3.52 is downstream of the step as in the growth rate data suggesting that the boundary layer is tripped (See Section 3.3.2). The slope of the least squares fit is nearly identical for the two different entrance conditions.

The Strouhal number, Str_H , in the isothermal layer is plotted with respect to the virtual origin in Figure 3.53 for $x/H = 1 - 4$. The Strouhal number clearly has a $1/(x - x_0)$ dependence given by,

$$Str_H = \frac{1.28 H}{(x - x_0)} \quad 3.8$$

On the average everytime the distance from the virtual origin is

increased by 2.6 the Strouhal number is halved.

In the isothermal layer coalescence seems to continue beyond $x/H = 4$ (Figure 3.51). There is not a clear trend in Str_H for $x/H > 5$, as the convection velocity of the eddies, U_c , is difficult to estimate near reattachment. Bradshaw and Wong (1972) reported that the eddies are split in two near reattachment. The rapid decrease in turbulence near reattachment is attributed to the "bifurcation of the shear layer at reattachment". They found at reattachment the length scale of the energy producing eddies is halved. As seen in Figure 3.51 eddy splitting does not take place. The data suggests that the wavelength actually increases slightly through the reattachment region. Thus the rapid decrease in shear stress near reattachment is not a result of eddy splitting.

The Strouhal number of the reacting data (Figure 3.51) does not show the simple $1/(x - x_0)$ dependence in the linear growth region ($x/H = 1 - 3$, Figure 3.19). The Strouhal number only decreases slightly between $x/H = 1 - 3$. In Figure 3.54 the Strouhal number is reported with respect to the virtual origin of the layer estimated from the growth rate data (Figure 3.19). Only the data in the linear growth region ($x/H = 1 - 3$) is used in the curve fit. The coalescence rate is much lower than the isothermal layer having a weak dependence on the streamwise coordinate:

$$Str_H = \frac{1.79 H}{(x - x_0)^{0.117}} \quad 3.9$$

Thus the effect of combustion and volumetric expansion is to greatly reduce the pairing process as a growth mechanism in the shear layer.

The shear layer grows primarily by entrainment of fluid and volumetric expansion as the fluid reacts.

After the fairly constant region in the reacting shear layer, Str_H decreases from $x/H = 3$ to $x/H = 7$ (Figure 3.51). The eddy wavelength increases in this region from heat expansion. The eddies are no longer retarded by the recirculation zone as they continue to burn and accelerate.

The mean spacing, \bar{l} , between the eddies in mixing layers is just $\bar{l} = Uc/\bar{f}$. For the isothermal layer the spacing will be (Equation 3.8):

$$\bar{l} = 0.78 (x - x_0) \quad 3.10$$

This is a larger spacing than found in two-stream mixing layers but similar to a single stream mixing layer formed at a round jet. Brown and Roshko (1974) estimated the mean spacing to be $\bar{l} = 0.92x$ from Kolpin's (1964) data.

The mean spacing in the reacting layer ($x/H = 1 - 3$) is nearly constant (Equation 3.9),

$$\bar{l} = 0.56 (x - x_0)^{0.117} \quad 3.11$$

emphasizing the low rate of coalescence.

The mean eddy spacing in isothermal layers is linearly dependent on δ_ω , $\bar{l} = c\delta_\omega$. Brown and Roshko (1974) compiled mixing layer data and estimated the constant, c , to be about 3. This constant can be written in terms of the passing frequency as,

$$c = \bar{l} / \delta_{\omega} = U_c / (\bar{f} \delta_{\omega}) \quad 3.12$$

The inverse Strouhal number based on vorticity thickness, $U_c / (\bar{f} \delta_{\omega})$, is shown in Figure 3.55 for the non-reacting and reacting shear layer. The isothermal data approaches a value of $c = 2.5$, which means the eddy mean spacing is 2.5 times the vorticity thickness. The reacting shear layer shows no constant value since the coalescence rate is very small and the wavelength, \bar{l} , is nearly constant with distance.

Table 3.1 Entry Flow Conditions

U_0 (M/s)	ϕ	Re_H	Re_θ	δ^* (mm)	H_{12}	u_{rms}/U_0 Free- Strv	Bound. Layer
9.1	0.0	1.5×10^4	140	0.63	2.58	0.015	0.040
9.1	0.57	1.5×10^4	150	0.62	2.50	0.030	0.045
13.3	0.0	2.2×10^4	180	0.50	2.46	0.020	0.050
13.3	0.57	2.2×10^4	190	0.55	2.48	0.030	0.055
22.2	0.0	3.7×10^4	280	0.47	2.42	0.020	0.080
22.2	0.57	3.7×10^4	250	0.42	2.41	0.030	0.070

Table 3.2 Reattachment Lengths

Re_H	ϕ	Re_θ	x_R/H
1.5×10^4	0	140	6.5
1.5×10^4	.57	150	4.3
2.2×10^4	0	180	7.0
2.2×10^4	.57	190	4.5
3.7×10^4	0	280	6.8
3.7×10^4	.57	250	5.3

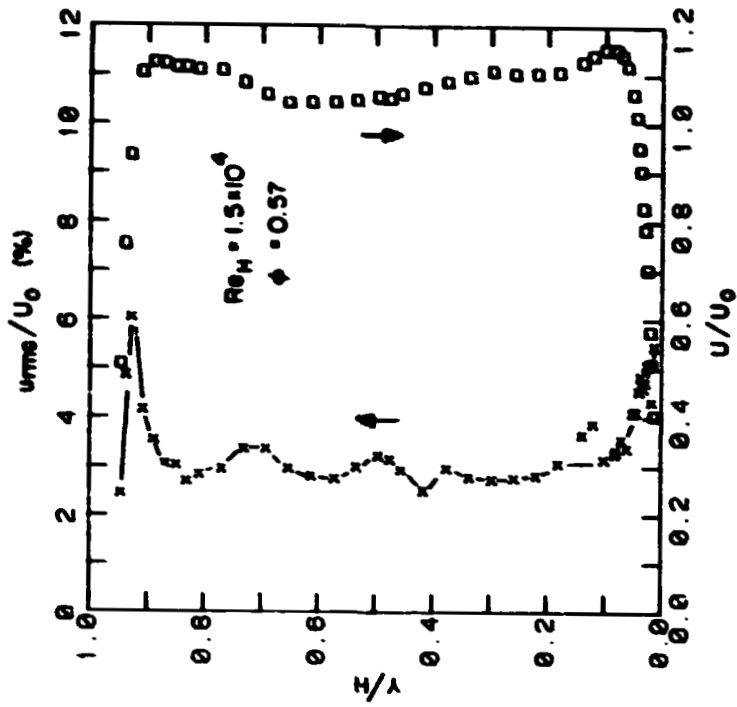
Table 3.3 Eddy Formation Position

Re_H	x_s/H		
	(LDV)	(Sch.)	
1.5×10^4	0.0	$0.5 \pm .3$	
1.5×10^4	0.57	$1.0 \pm .3$	$0.89 \pm .14$
2.2×10^4	0.0	$0.5 \pm .3$	
2.2×10^4	0.57	$1.0 \pm .3$	$0.67 \pm .08$

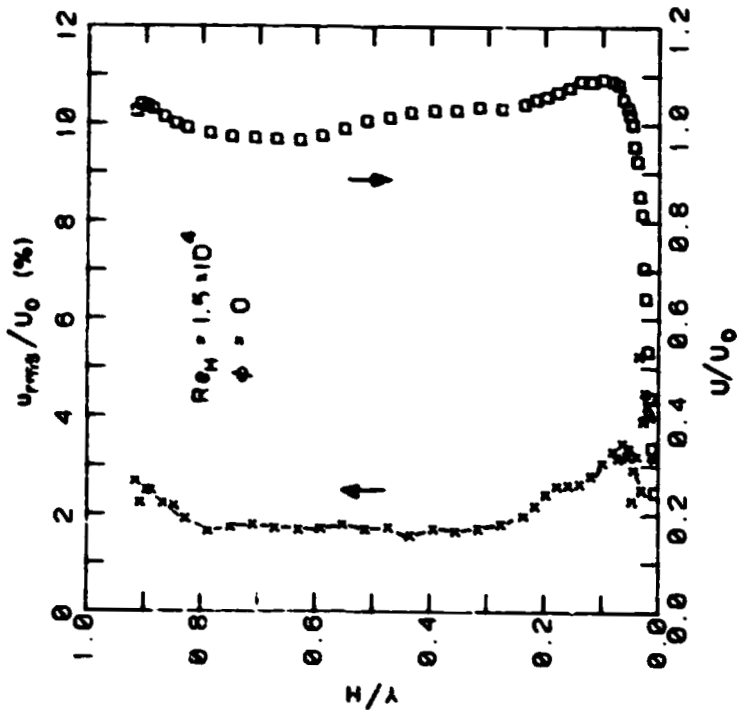
ORIGINAL PAGE IS
OF POOR QUALITY

C-2

ORIGINAL PAGE IS
OF POOR QUALITY



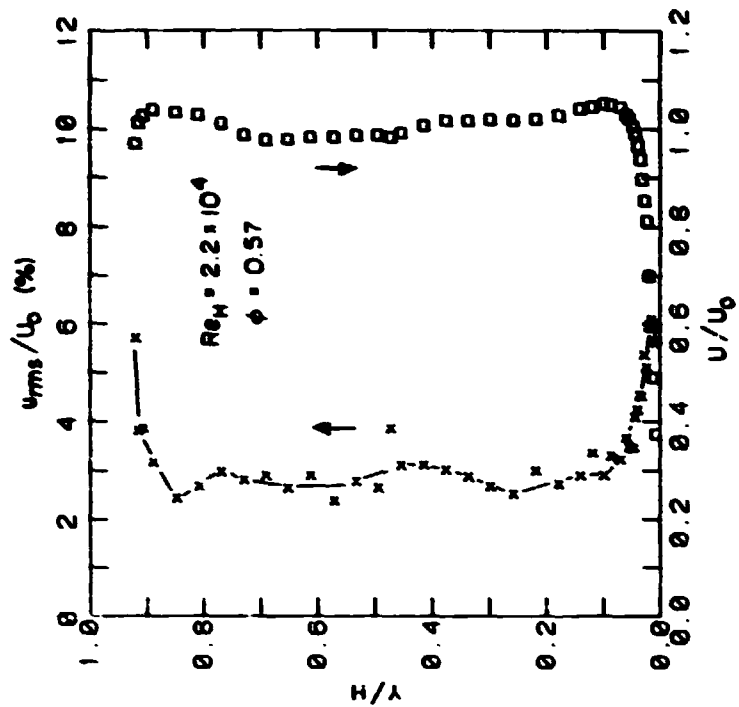
a) Non-reacting.



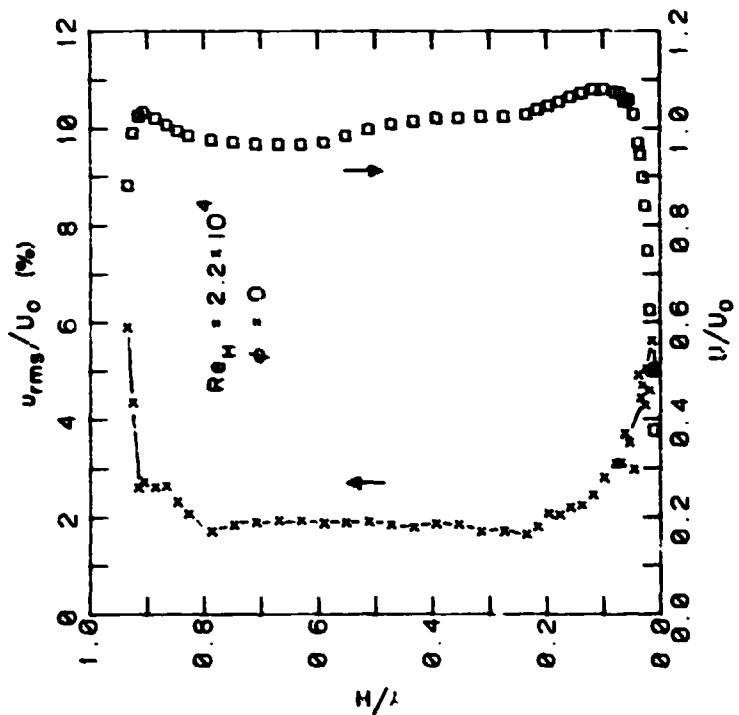
b) Reacting.

Figure 3.1 Entry velocity profile -- low Reynolds number.
($x/H = 0$, $z/H = 0$)

ORIGINAL PAGE IS
OF POOR QUALITY

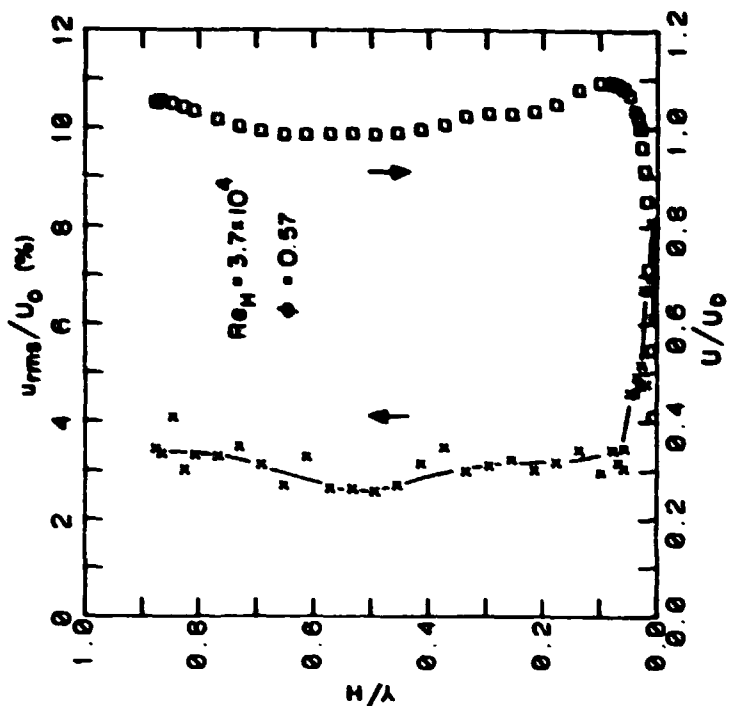


a) Non-reacting.

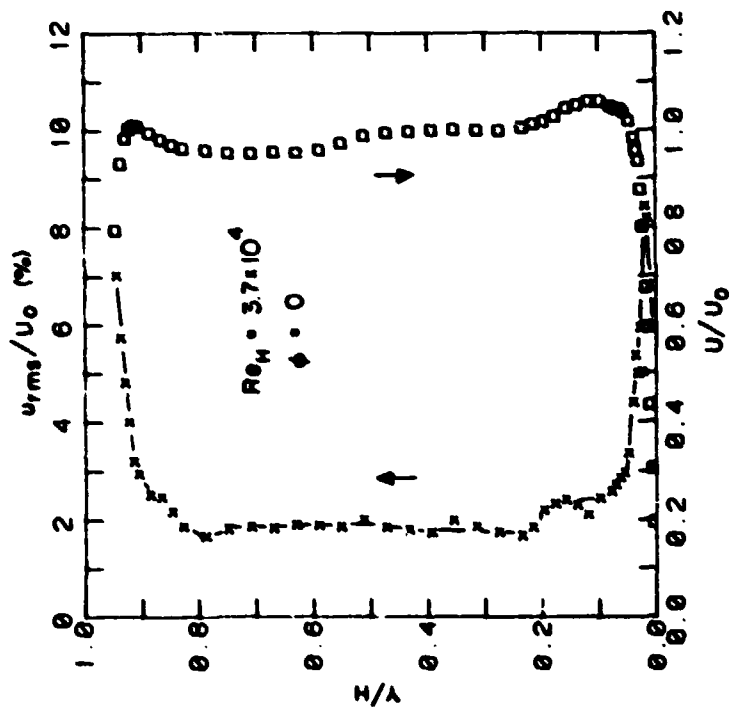


b) Reacting.

Figure 3.2 Entry velocity profile -- medium Reynolds number.
($x/H = 0$, $z/H = 0$).



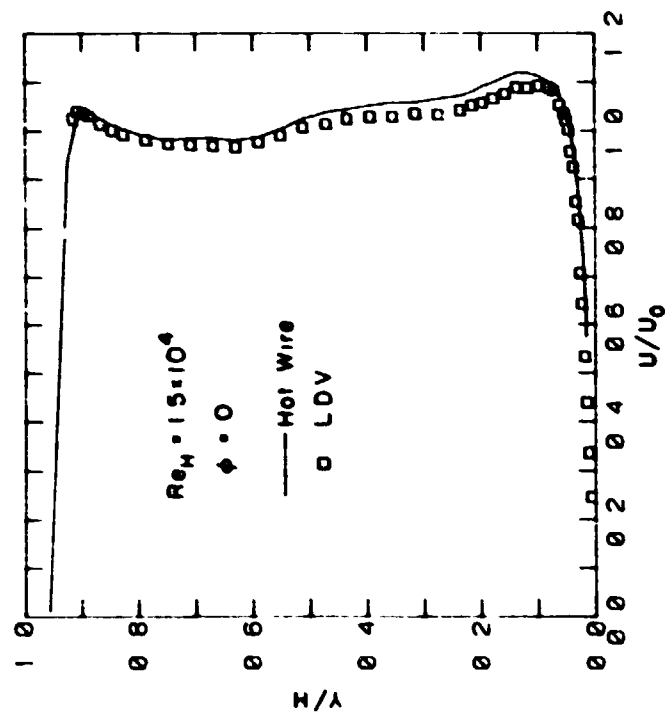
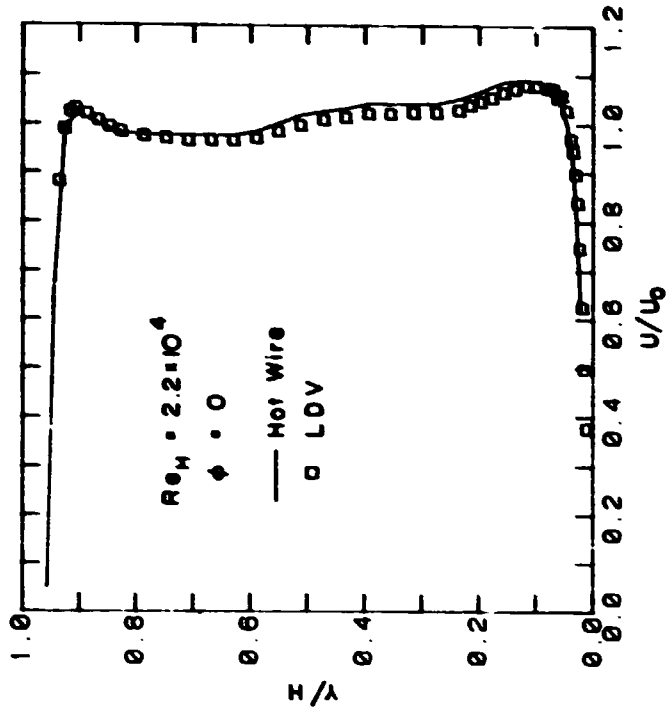
a) Non-reacting.



b) Reacting.

Figure 3.3 Entry velocity profile -- high Reynolds number.
($x/H = 0$, $z/H = 0$).

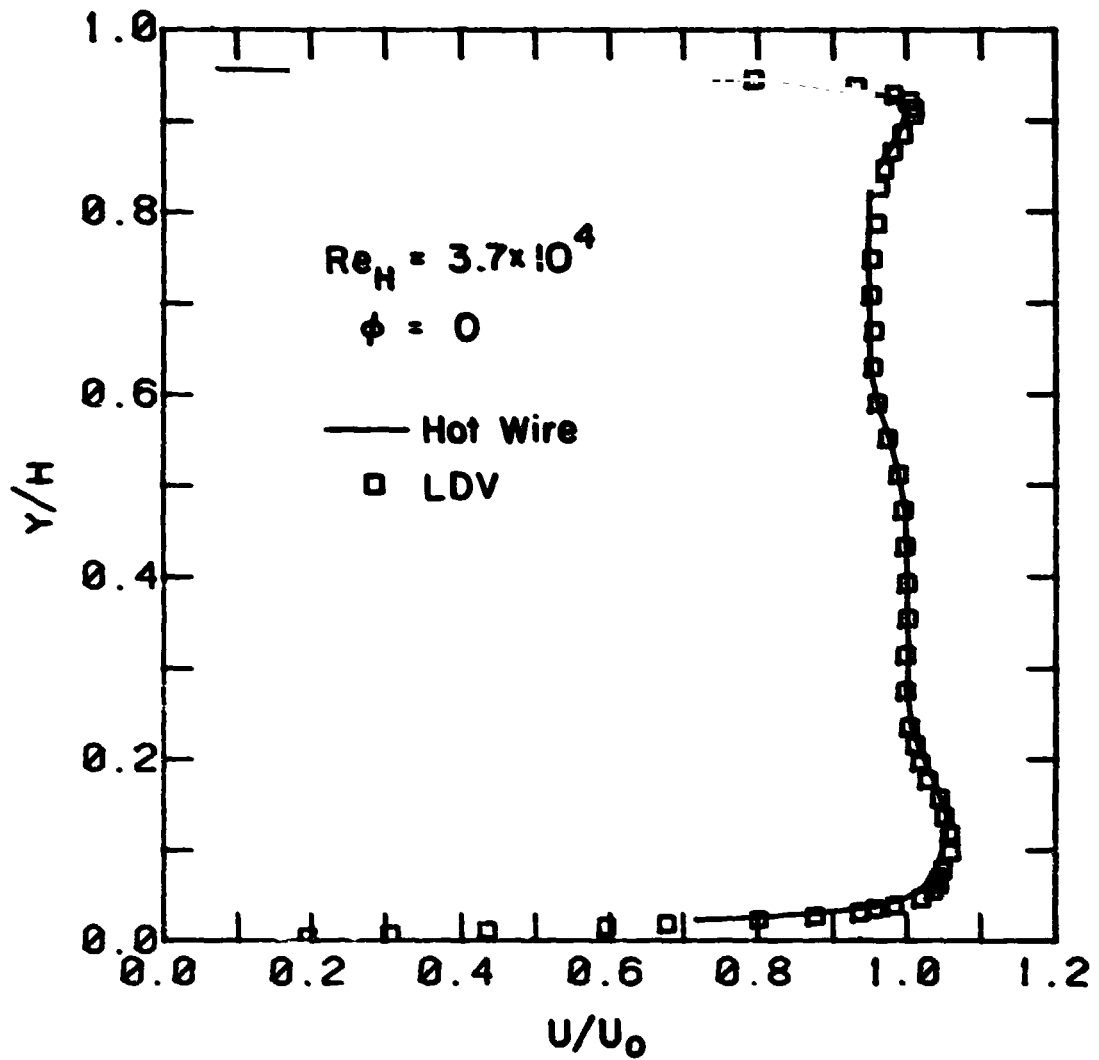
ORIGINAL PAGE IS
OF POOR QUALITY.



a) Low Reynolds number.

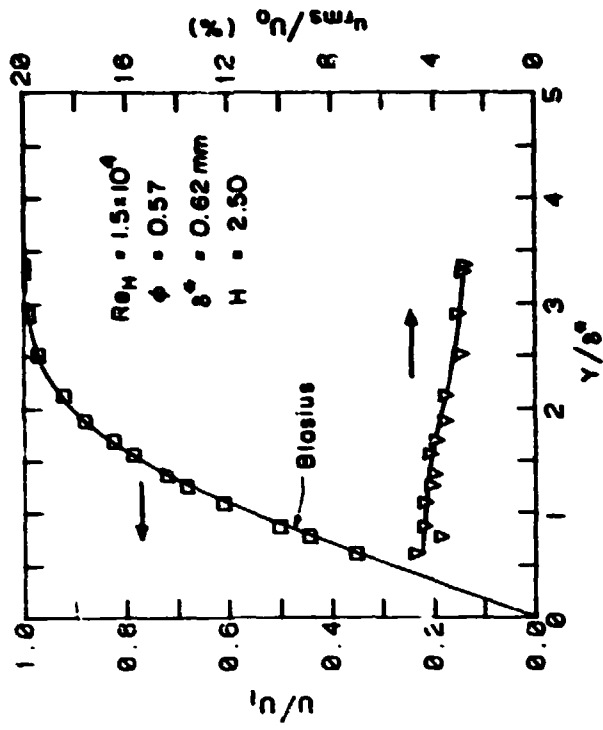
b) Medium Reynolds number.

Figure 3.4 Comparison of LDV and hot wire velocity measurements in the entry flow.
($x/H = 0$, $z/H = 0$).

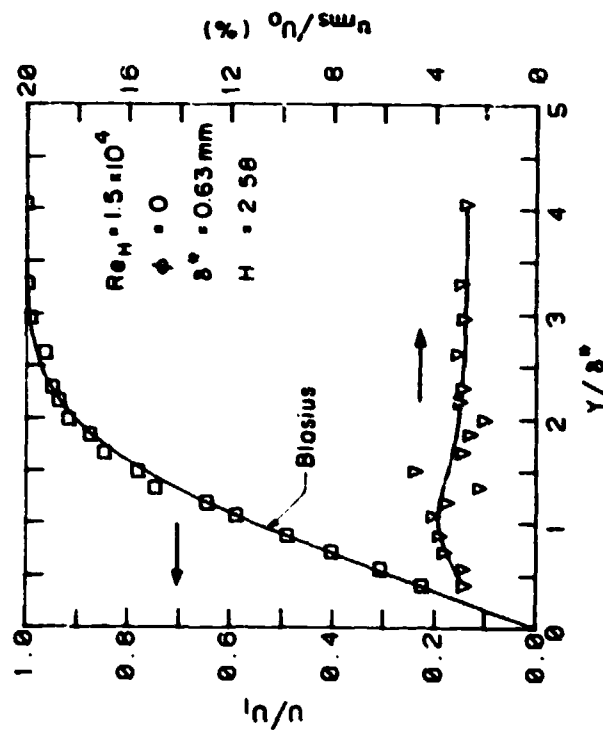
COMPARISONS
OF POOR QUALITY

c) High Reynolds number.

Figure 3.4 Comparison of LDV and hot wire velocity measurements in the entry flow. ($x/H = 0$, $z/H = 0$).

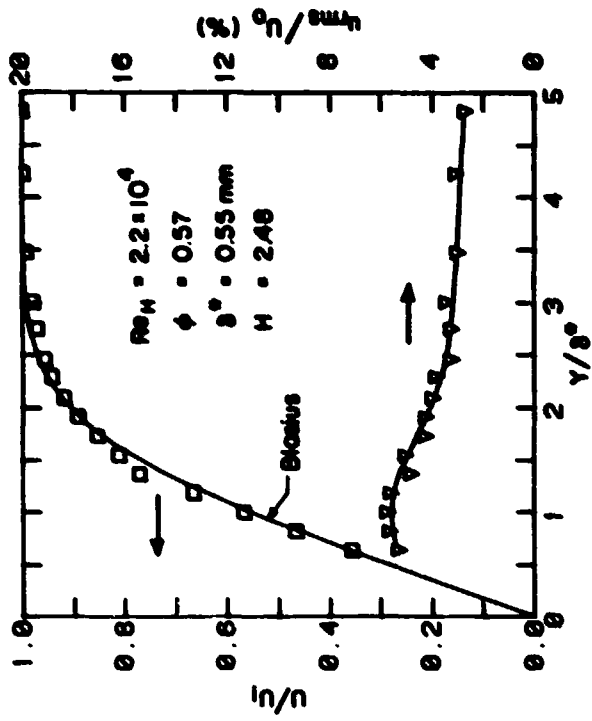


a) Non-reacting.

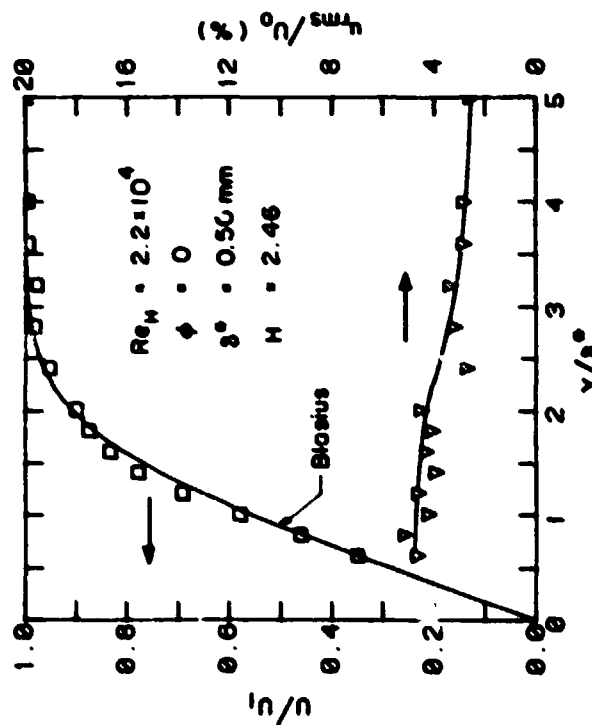


b) Reacting.

Figure 3.5 Boundary layer at separation -- low Reynolds number.
($x/H = 0$, $z/H = 0$)

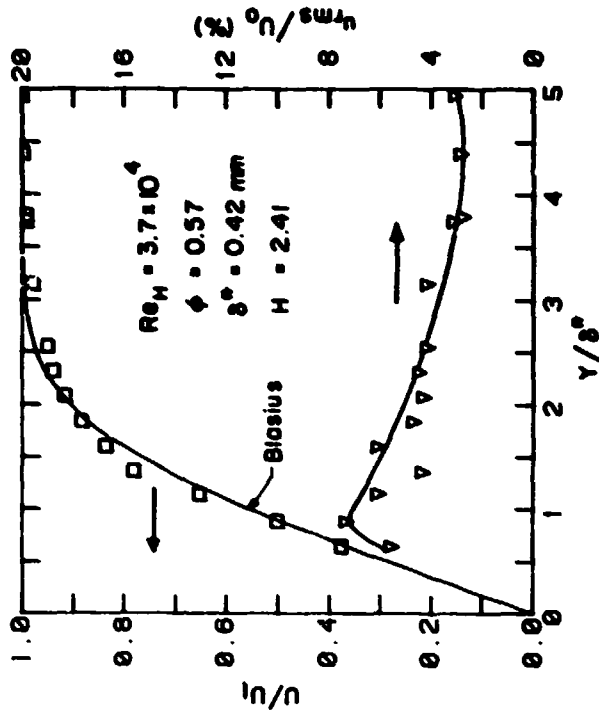


a) Non-reacting.

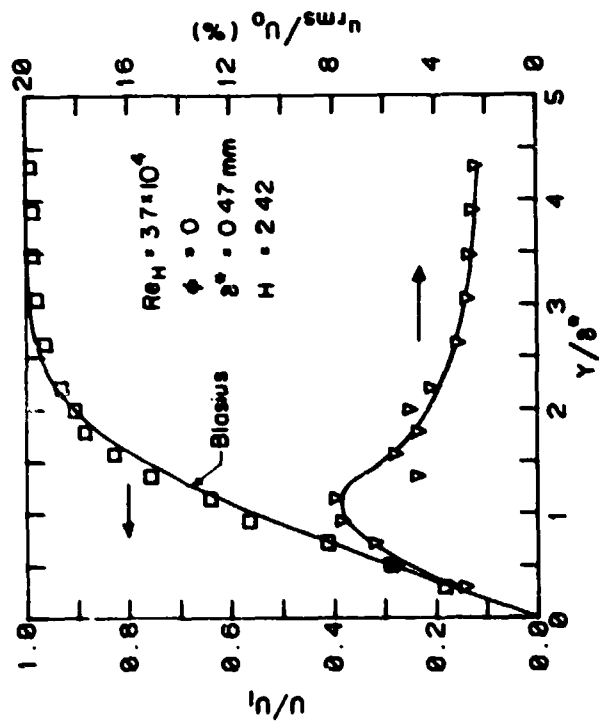


b) Reacting.

Figure 3.6 Boundary layer at separation -- medium Reynolds number.
($x/H = 0$, $z/H = 0$)



a) Non-reacting.



b) Reacting.

Figure 3.7 Boundary layer at separation -- high Reynolds number.
($x/H = 0$, $z/H = 0$)

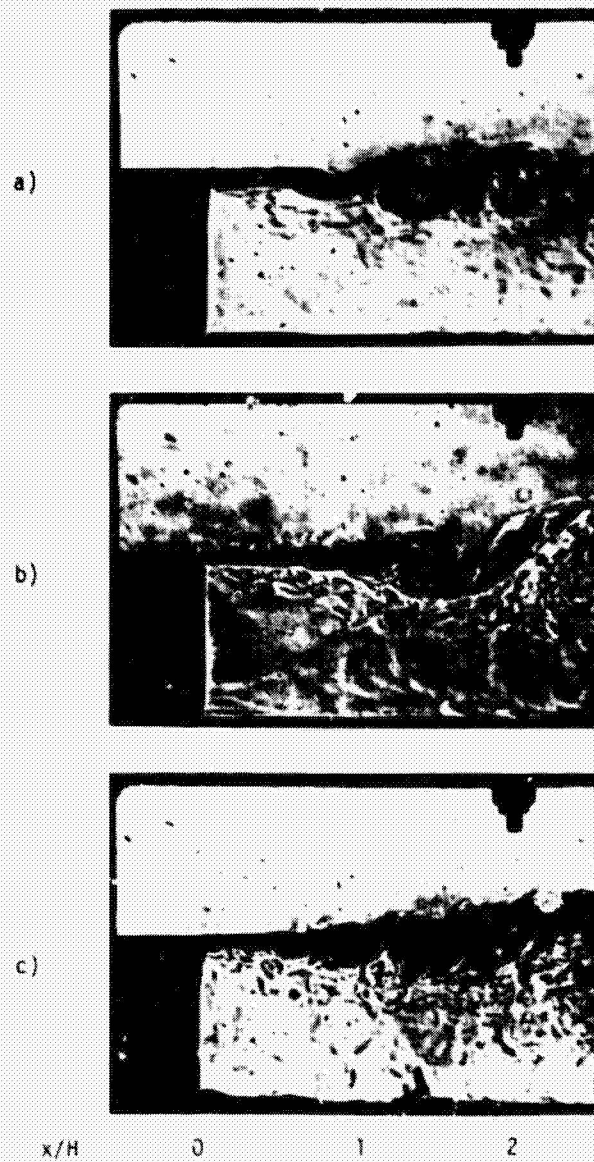


Figure 3.8 Schlieren photographs of the initial shear layer for reacting flow [$\phi = 0.57$, a) $Re_H = 1.5 \times 10^4$, $\tau_{exp} = 80 \mu s$, b) $Re_H = 2.2 \times 10^4$, $\tau_{exp} = 60 \mu s$, c) $Re_H = 3.7 \times 10^4$, $\tau_{exp} = 60 \mu s$].

ORIGINAL PAGE IS
OF POOR QUALITY

ORIGINAL PAGE IS
OF POOR QUALITY

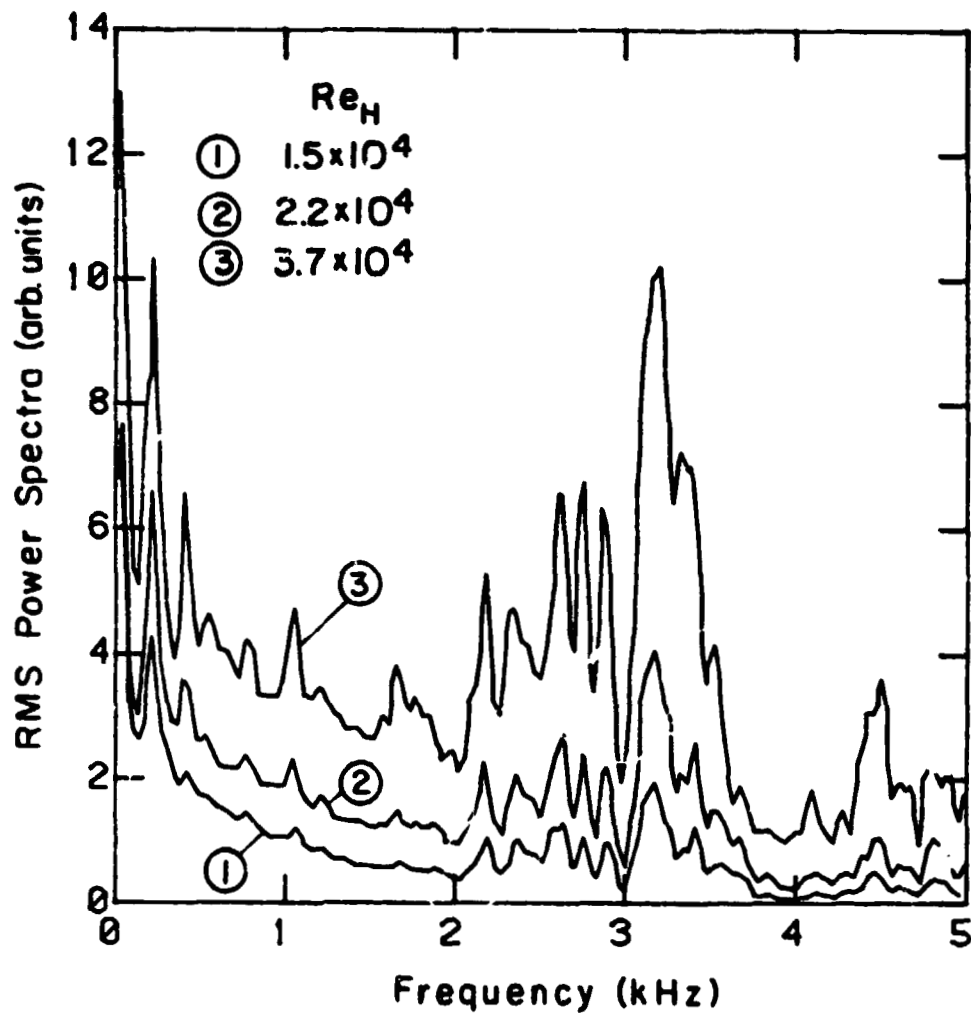


Figure 3.9 Hot wire spectra of the u-velocity at the step without packing as used by Ganji and Sawyer (1980) ($x/H = 0$, $y/H = 0.5$, $z/H = 0$, $\phi = 0$).

ORIGINAL PAGE IS
OF POOR QUALITY

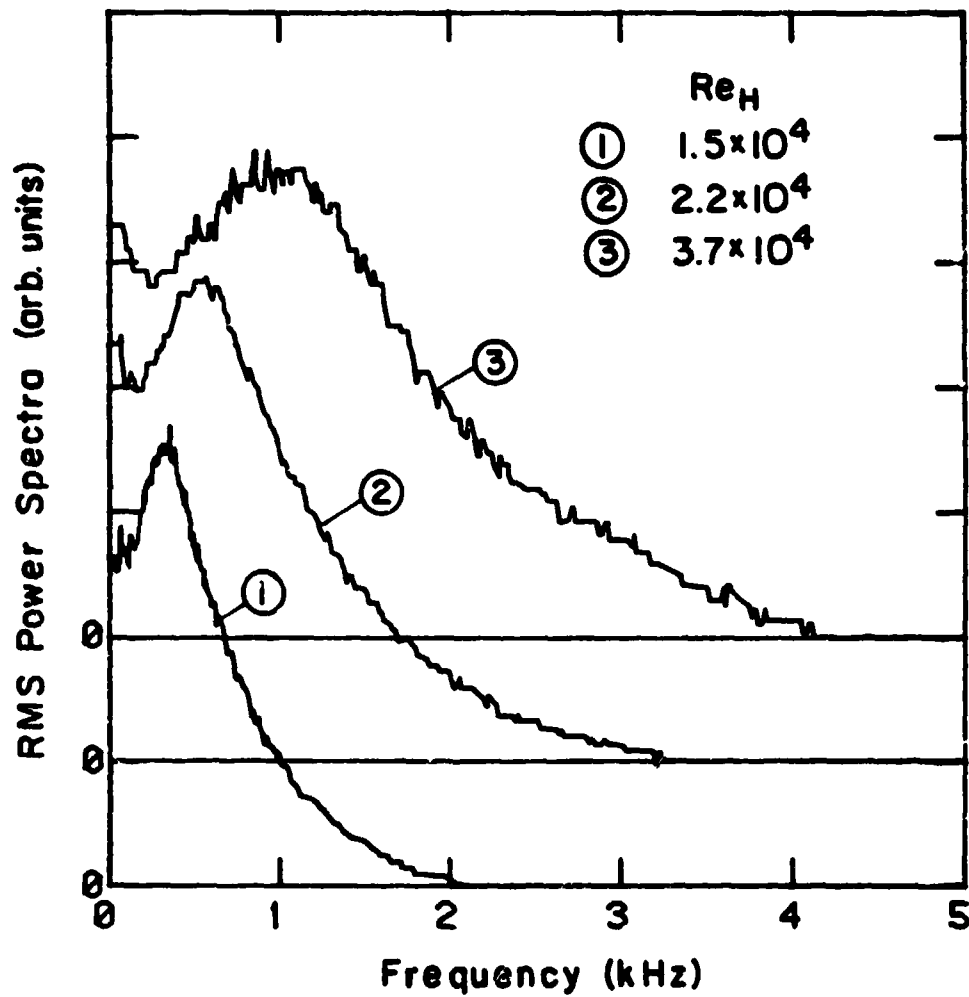


Figure 3.10 Hot wire spectra of the u -velocity at the step, with stainless steel packing and screens ($x/H = 0$, $y/H = 0.5$, $z/H = 0$, $\phi = 0$).

ORIGINAL INTENT
OF POOR QUALITY

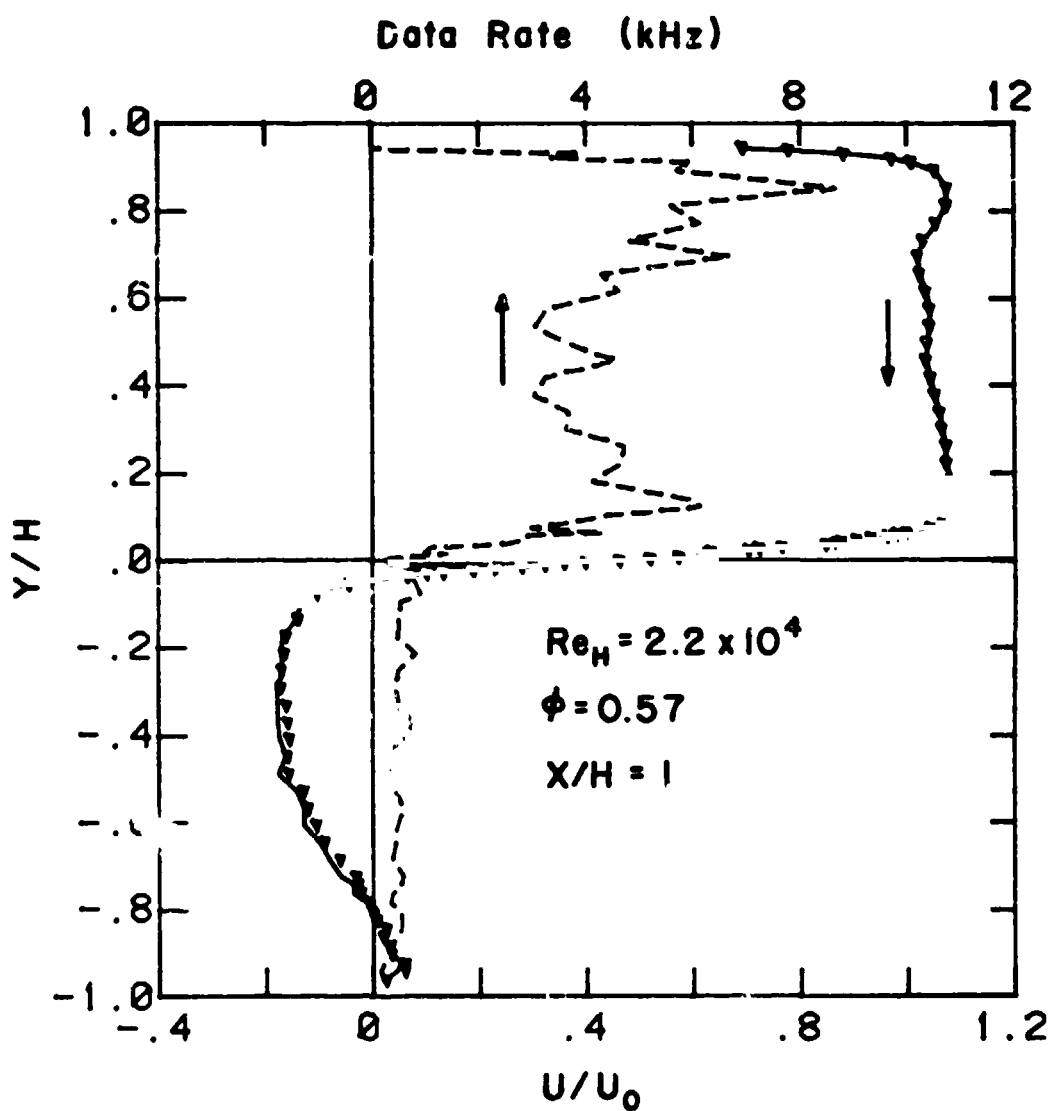
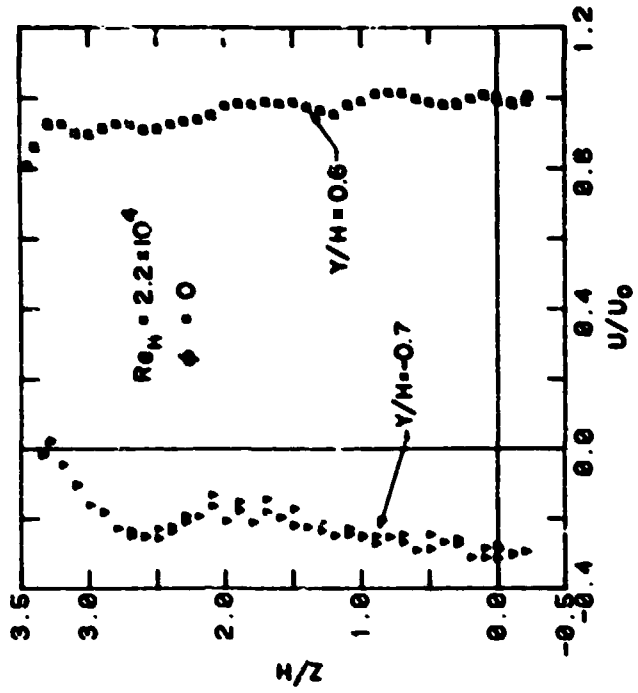
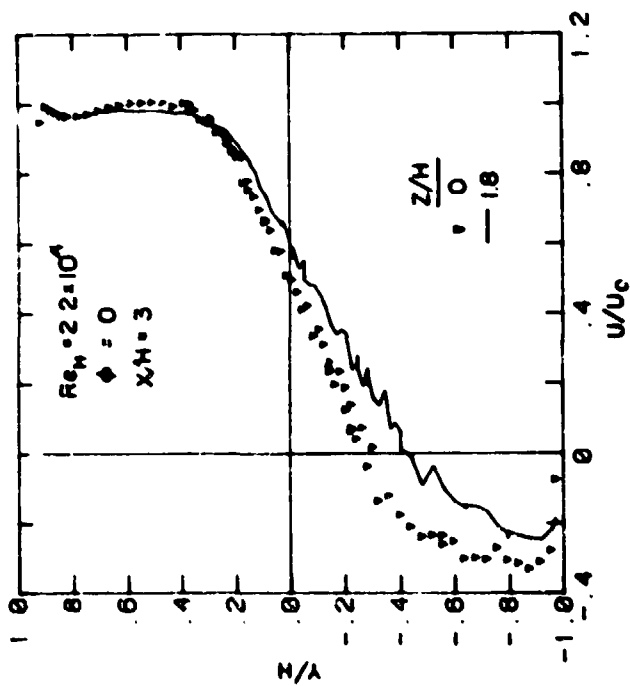


Figure 3.11 Typical centerline streamwise velocity profile in the shear layer (∇ time integrated mean velocity, — numerical mean velocity).



b) Z-scan of velocity above and below the shear layer.



a) Y-scan of velocity on and off centerline.

Figure 3.12 Two-dimensionality of flow field.

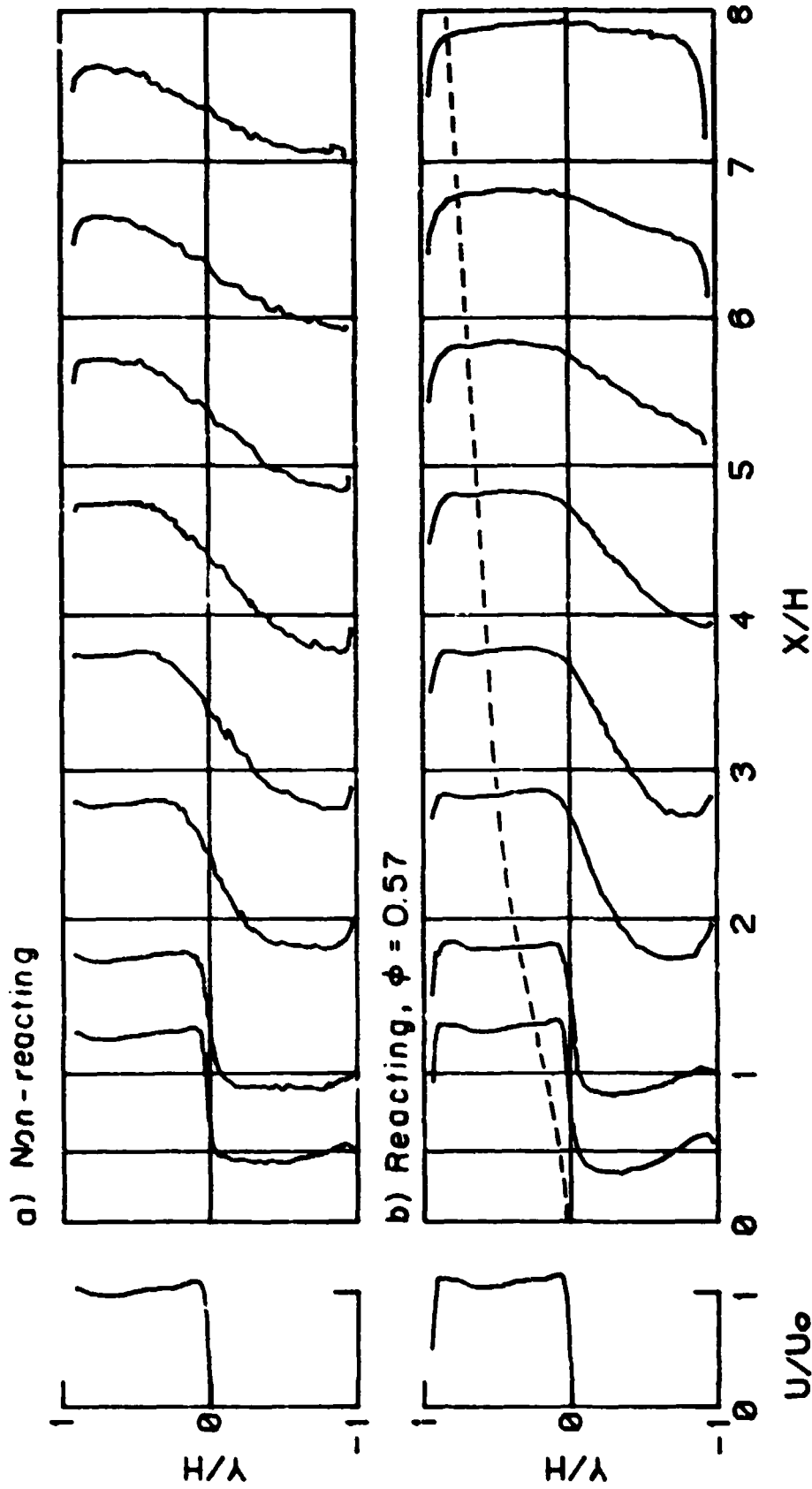


Figure 3.13 Streamwise velocity flowfield -- low Reynolds number ($Re_H = 1.5 \times 10^4$, $U_0 = 9.12$ m/s, --- flame boundary).

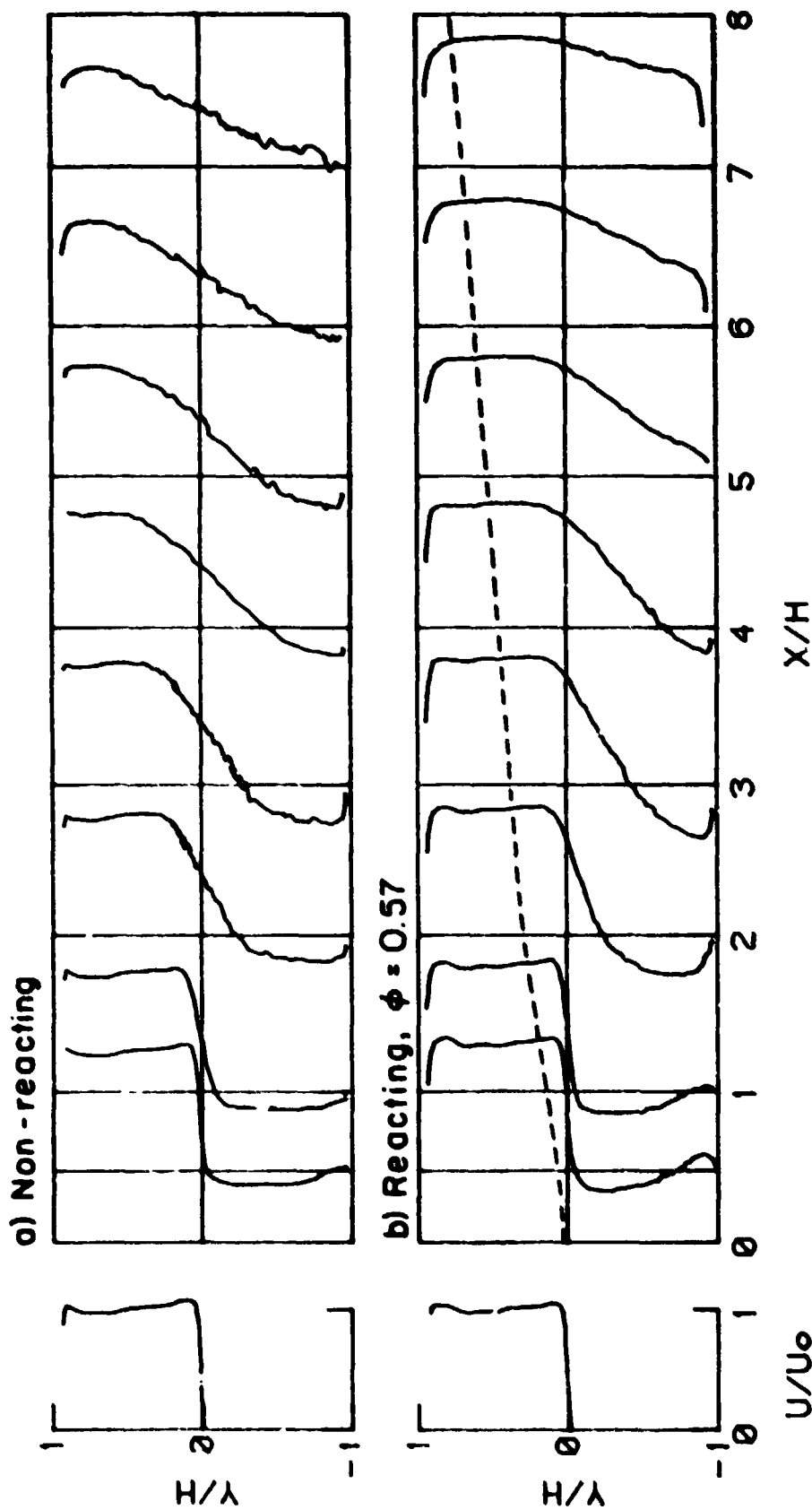


Figure 3.14 Streamwise velocity flowfield -- medium Reynolds number ($Re_H = 2.2 \times 10^4$, $U_0 = 13.3$ m/s, --- flame boundary).

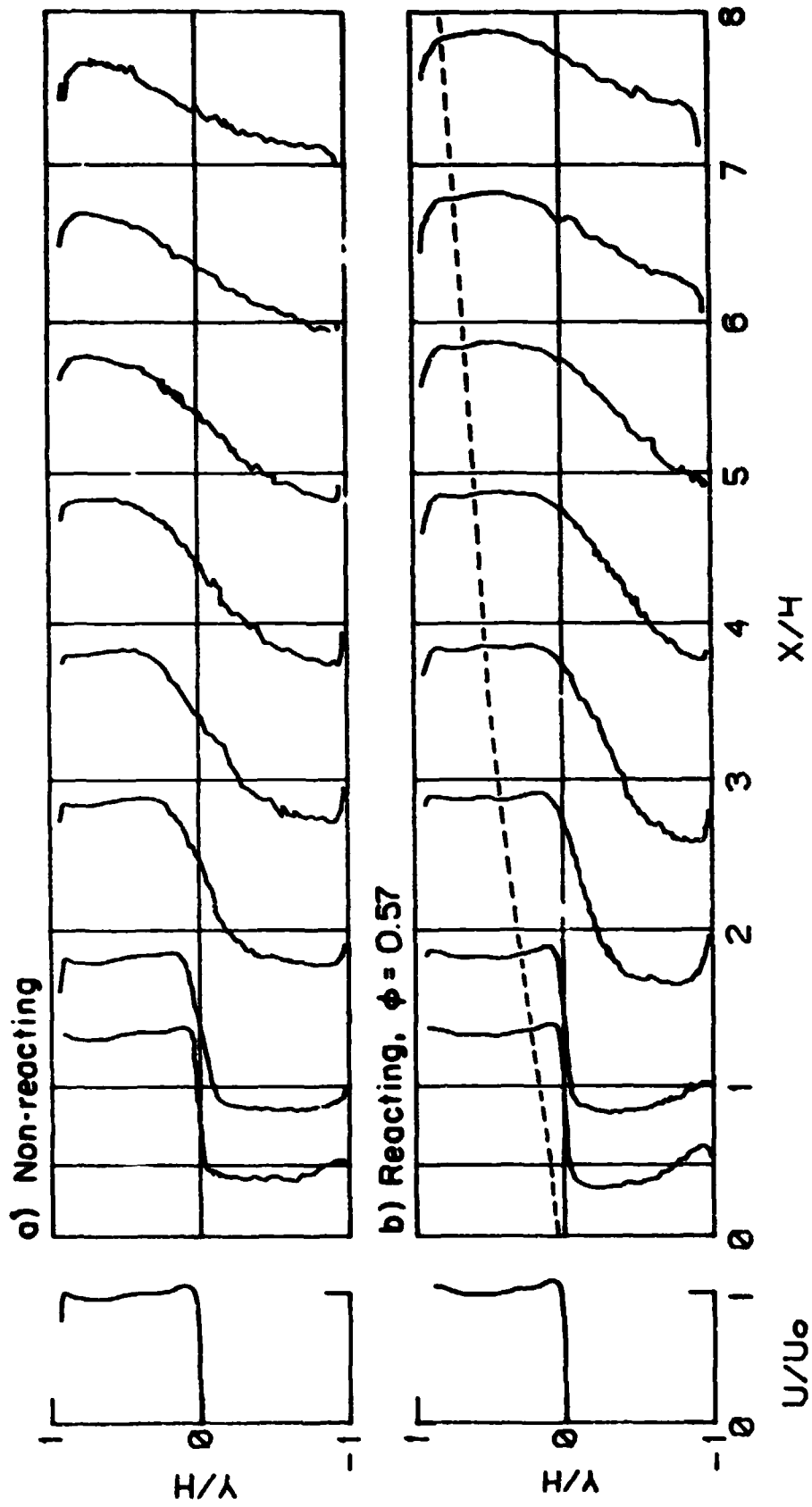
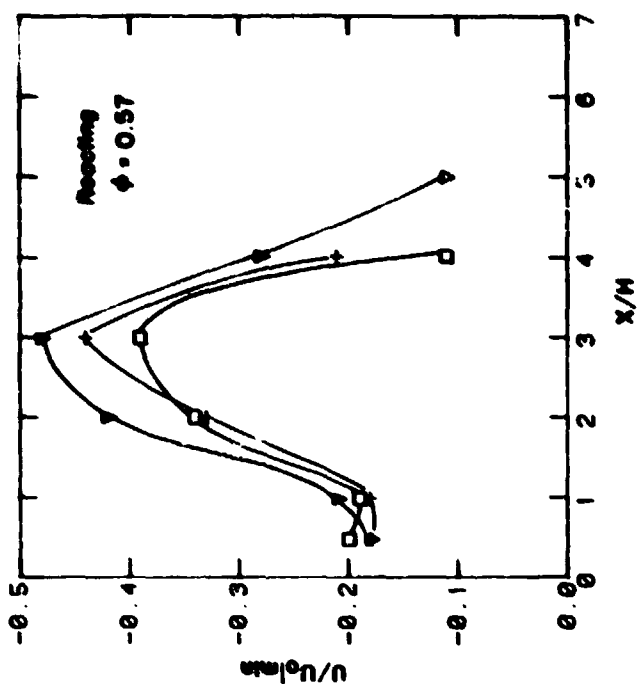
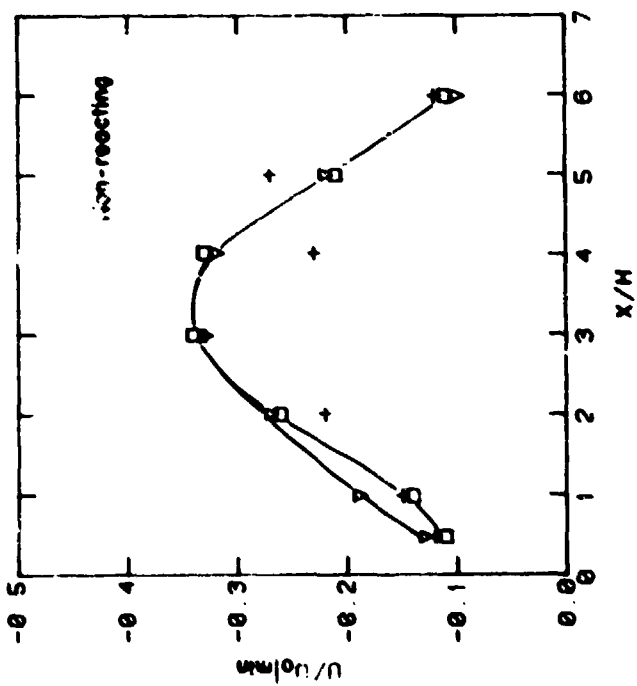


Figure 3.15 Streamwise velocity flowfield -- high Reynolds number
($Re_H = 3.7 \times 10^4$, $U_0 = 22.2$ m/s, --- flame boundary).



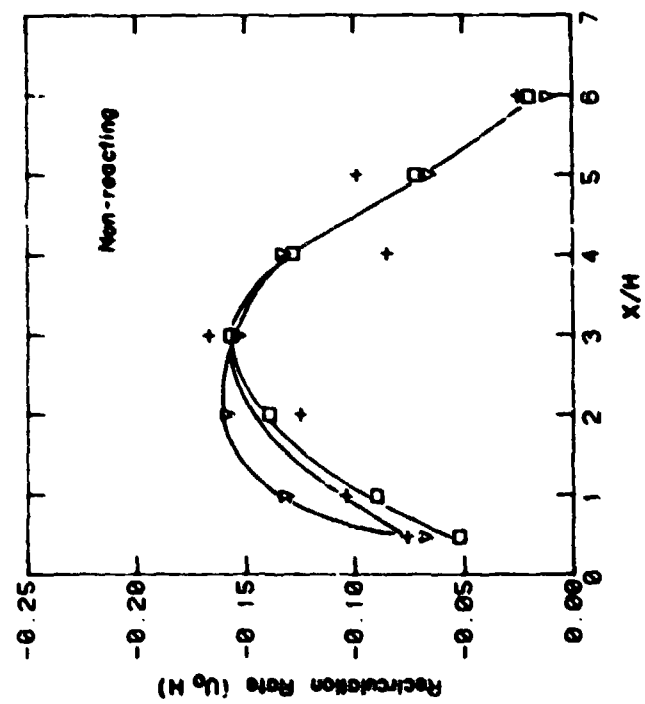
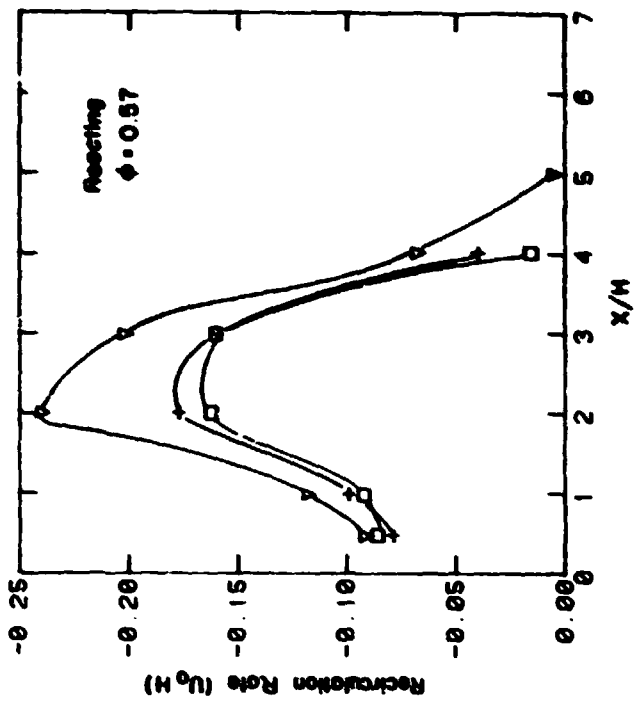
a) Non-reacting.



b) Reacting.

Figure 3.16 Maximum reverse velocity in the recirculation zone.
(□ $U_0 = 9.12$ m/s, + $U_0 = 13.3$ m/s, ▽ $U_0 = 22.2$ m/s).

ORIGINAL FILE IS
OF POOR QUALITY



a) Non-reacting.

b) Reacting.

Figure 3.17 Streamwise volumetric recirculation rate.
(□ $U_0 = 9.12$ m/s, + $U_0 = 13.3$ m/s, ▽ $U_0 = 22.2$ m/s).

CHARACTERISTICS
OF POOR QUALITY

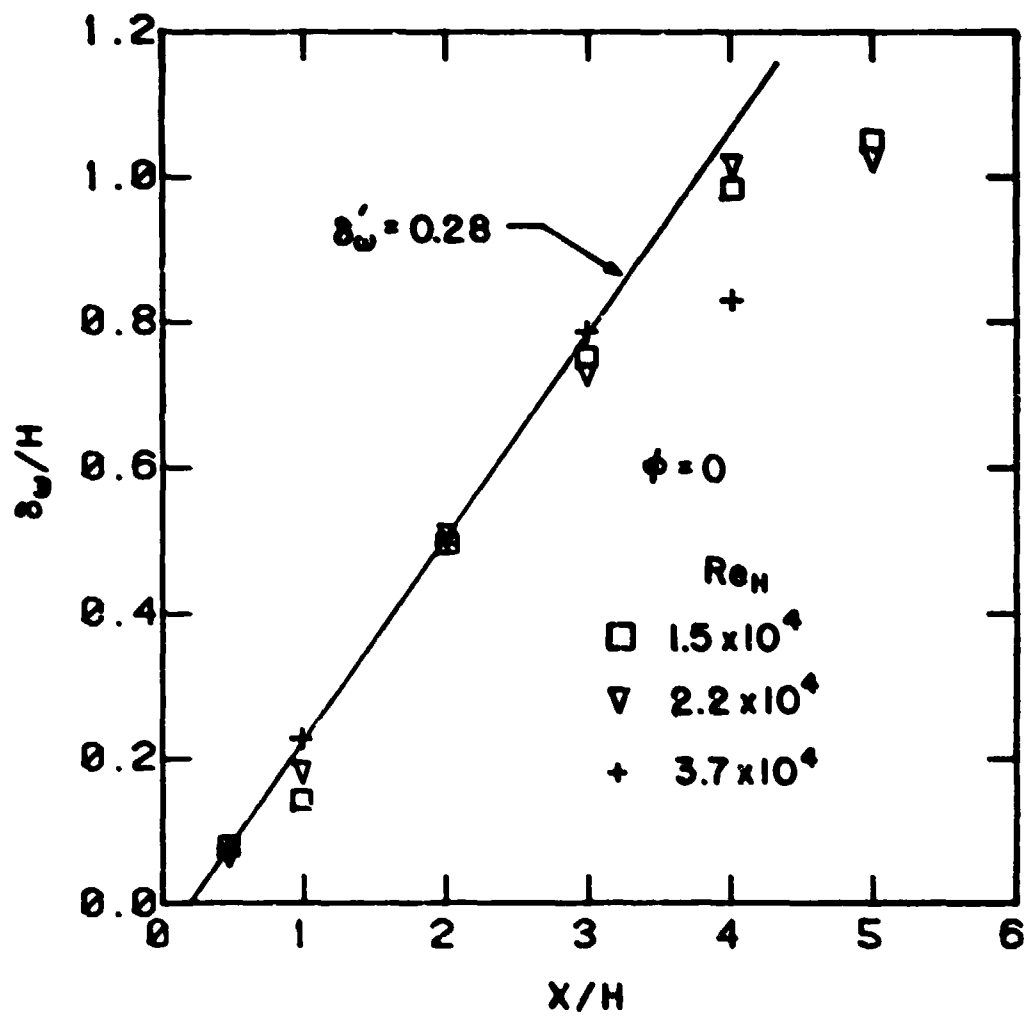


Figure 3.18 Vorticity thickness of the non-reacting shear layers.

ORIGINAL PAGE IS
OF POOR QUALITY

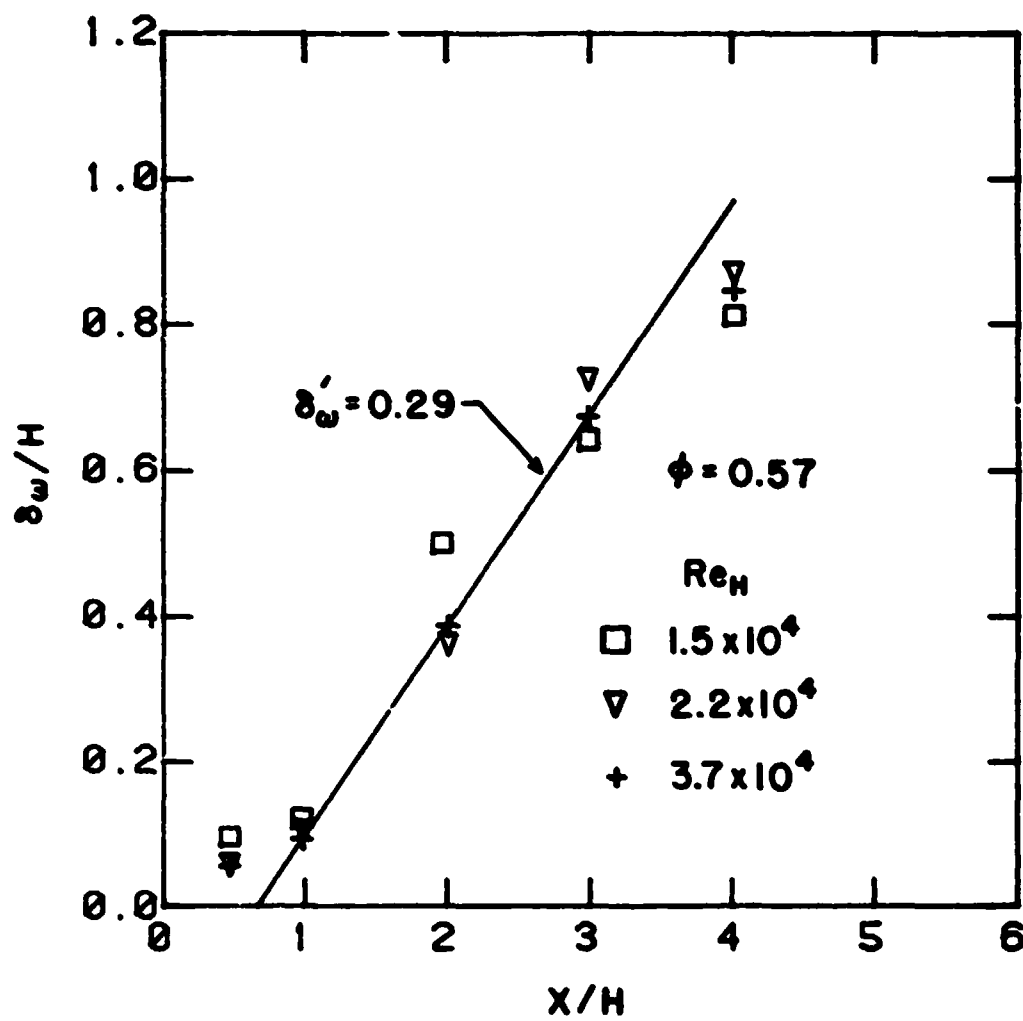


Figure 3.19 Vorticity thickness of the reacting shear layers.

CHARACTERISTICS
OF POOR QUALITY

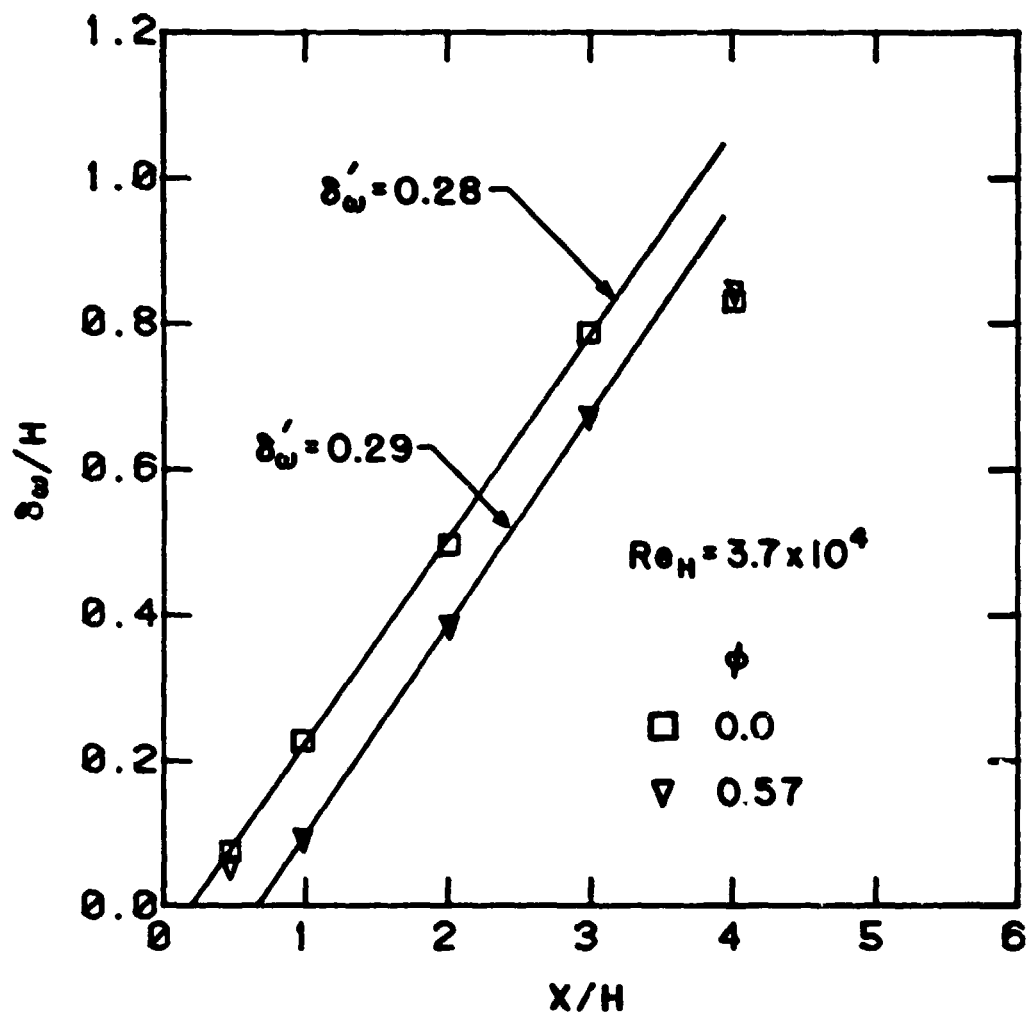


Figure 3.20 Comparison of vorticity thickness for reacting and non-reacting shear layers.

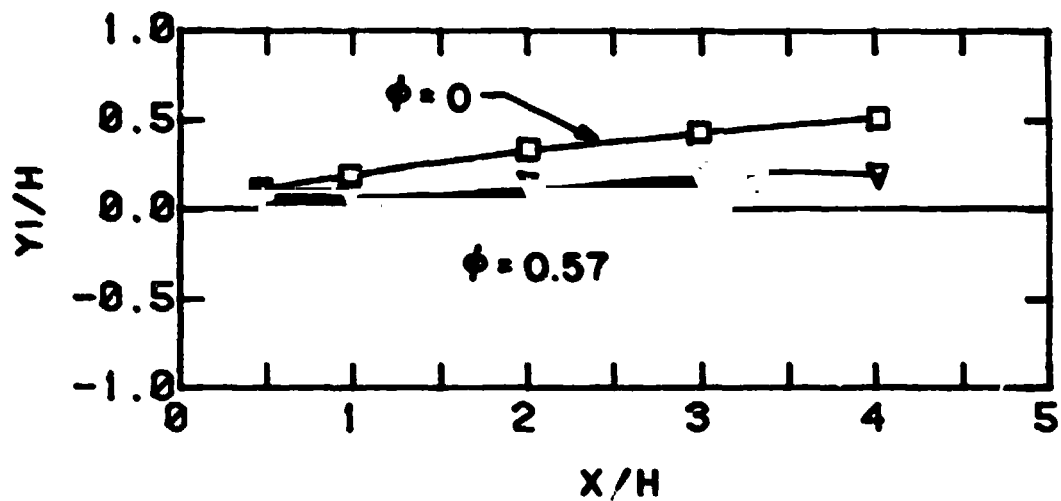


Figure 3.21a Upper boundary of shear layer for $Re_H = 3.7 \times 10^4$.

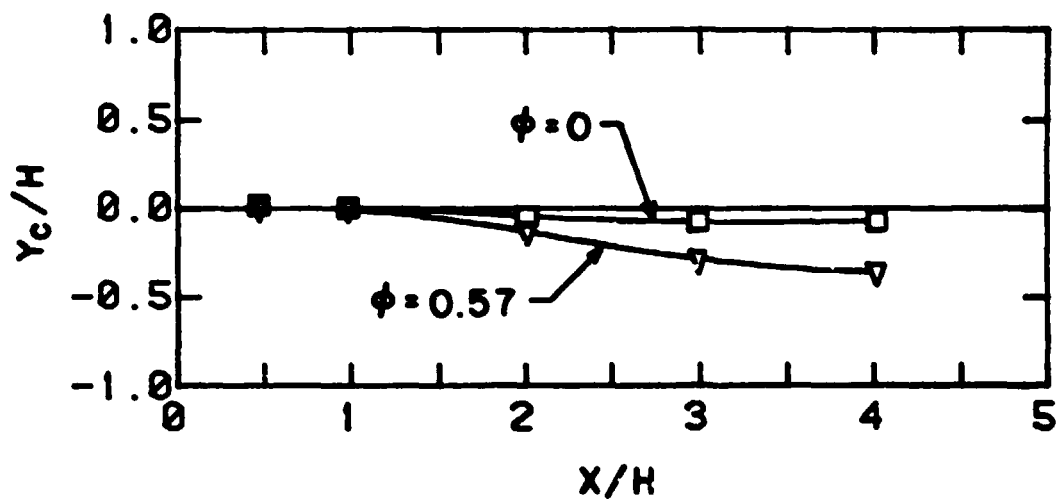


Figure 3.21b Centerline position of shear layer for $Re_H = 3.7 \times 10^4$.

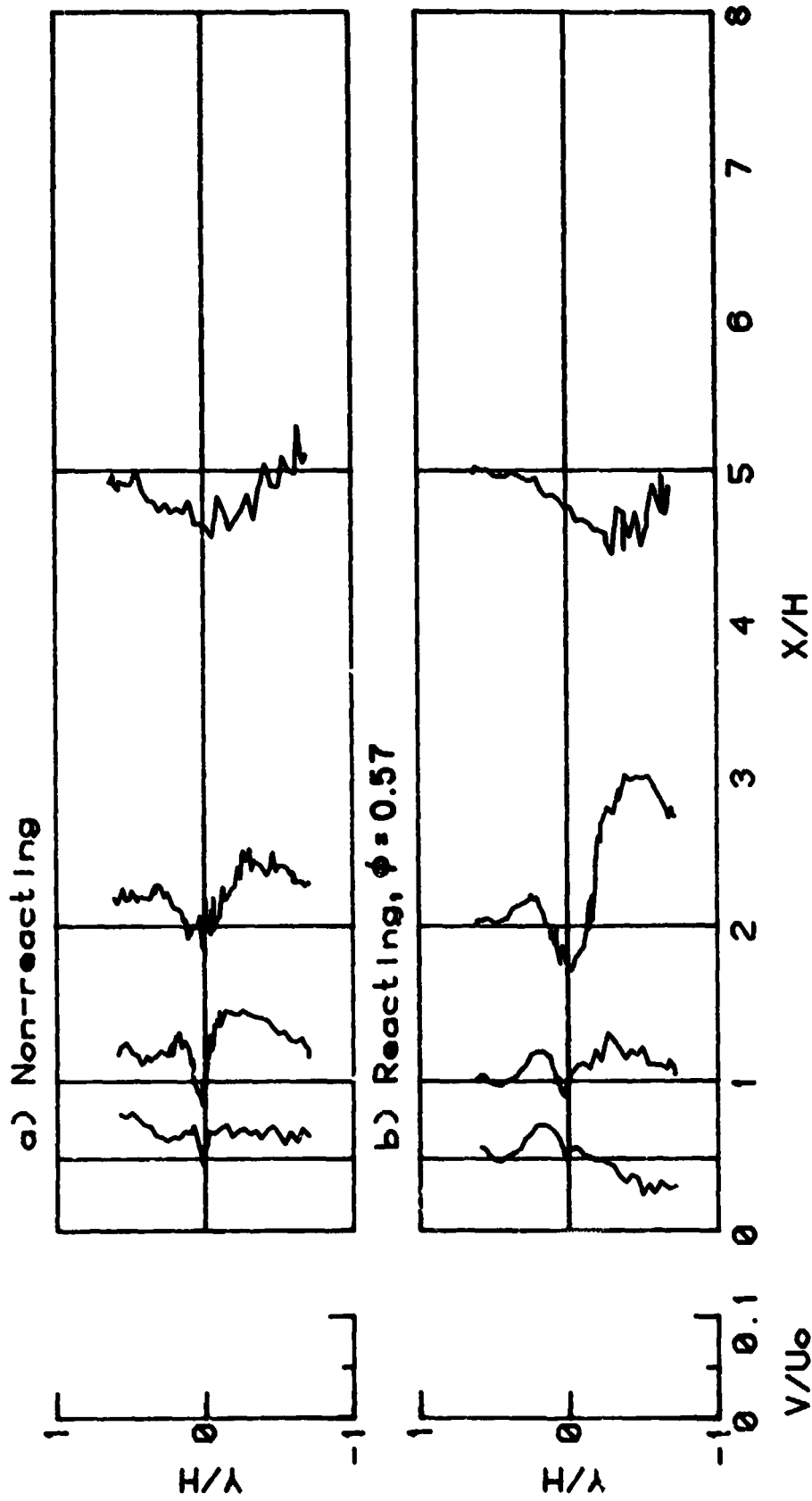


Figure 3.22 Transverse velocity flowfield ($Re_H = 2.2 \times 10^4$, $U_0 = 13.3$ m/s).

ORIGINAL PAGE IS
OF POOR QUALITY

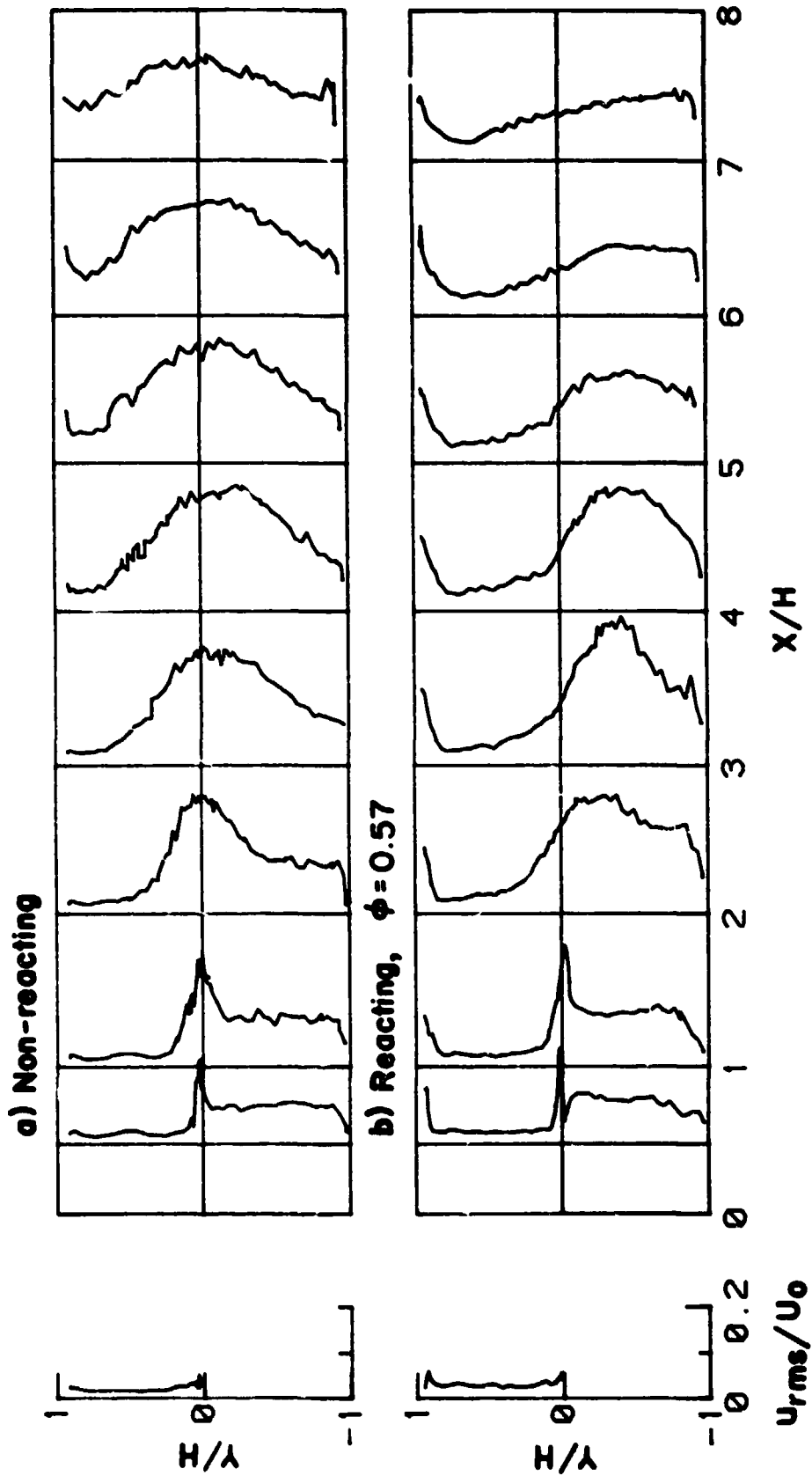


Figure 3.23 Streamwise turbulence intensity profiles -- low Reynolds number
($Re_H = 1.5 \times 10^4$, $U_0 = 9.12$ m/s).

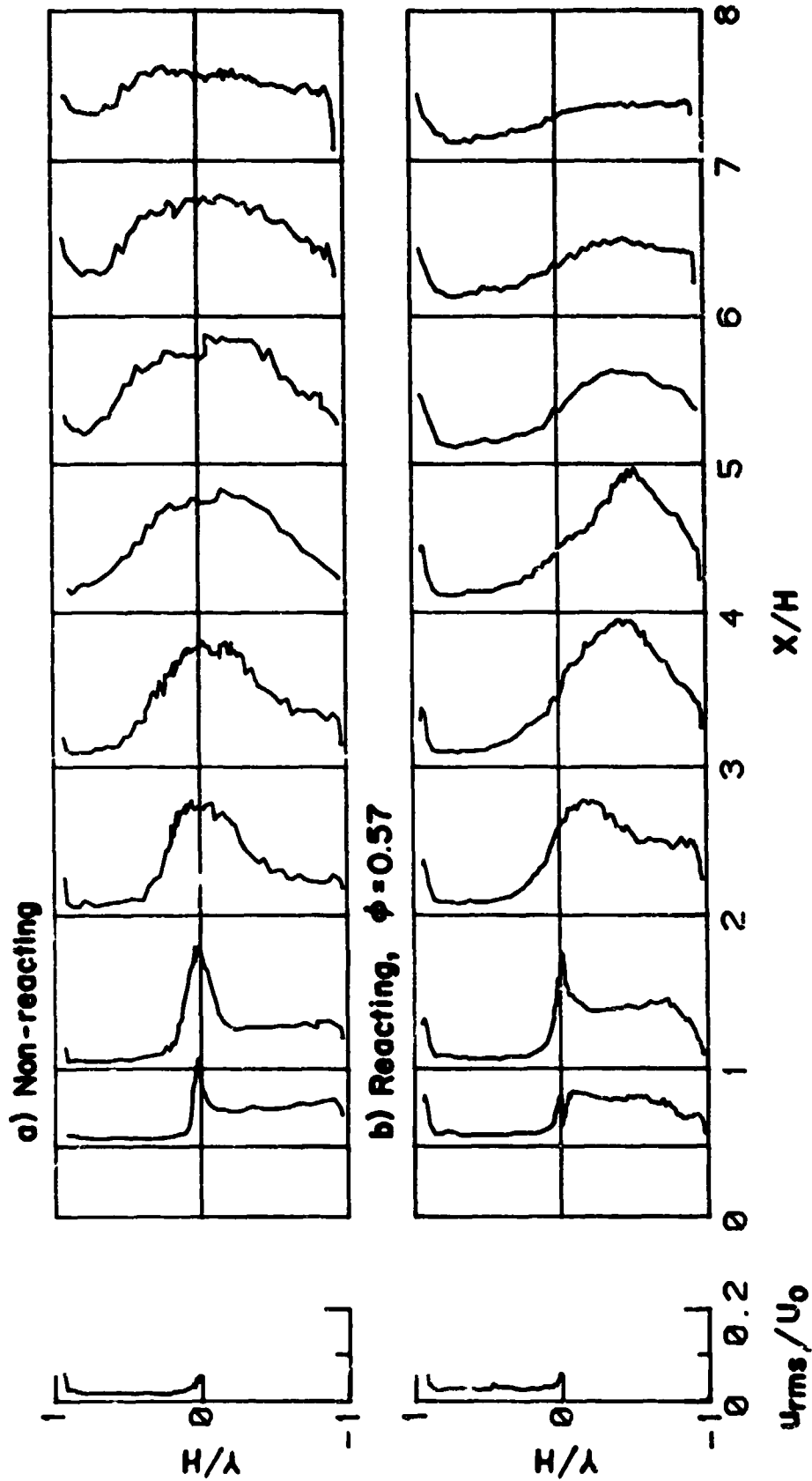


Figure 3.24 Streamwise turbulence intensity profiles -- medium Reynolds number
($Re_H = 2.2 \times 10^4$, $U_0 = 13.3$ m/s).

ORIGINAL IMAGE IS
OF POOR QUALITY

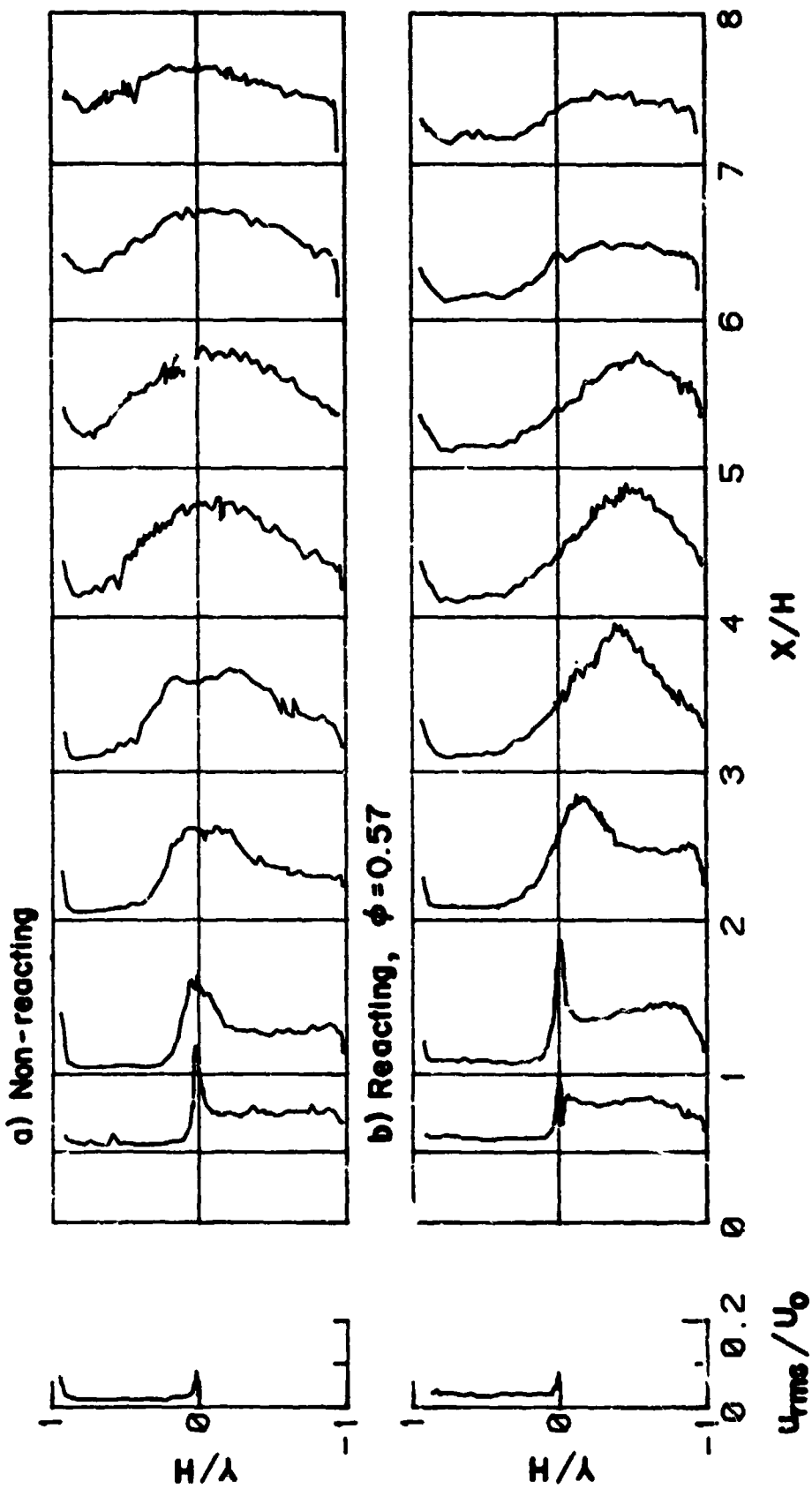
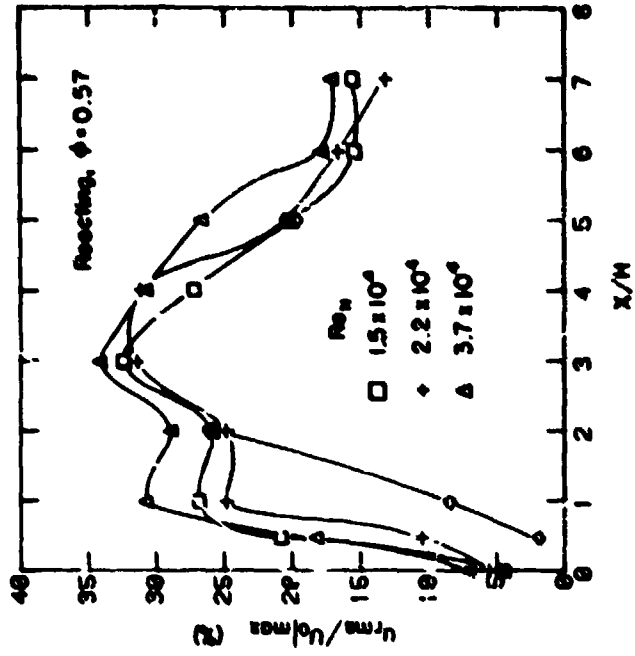
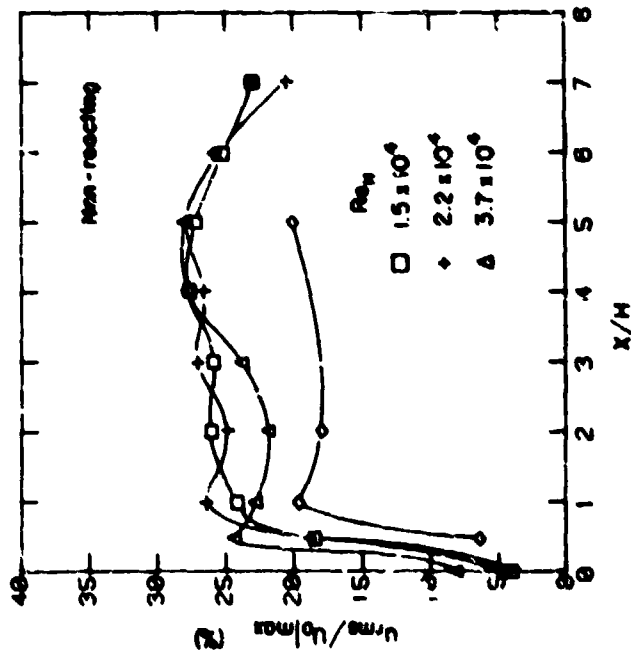


Figure 3.25 Streamwise turbulence intensity profiles -- high Reynolds number
($Re_h = 3.7 \times 10^4$, $U_0 = 22.2$ m/s).

ORIGINAL FIGURES
OF POOR QUALITY



b) Reacting.



a) Non-reacting.

Figure 3.26 Maximum turbulent intensities
($\langle \diamond \rangle v_{rms}$, $Re_M = 2.2 \times 10^6$).

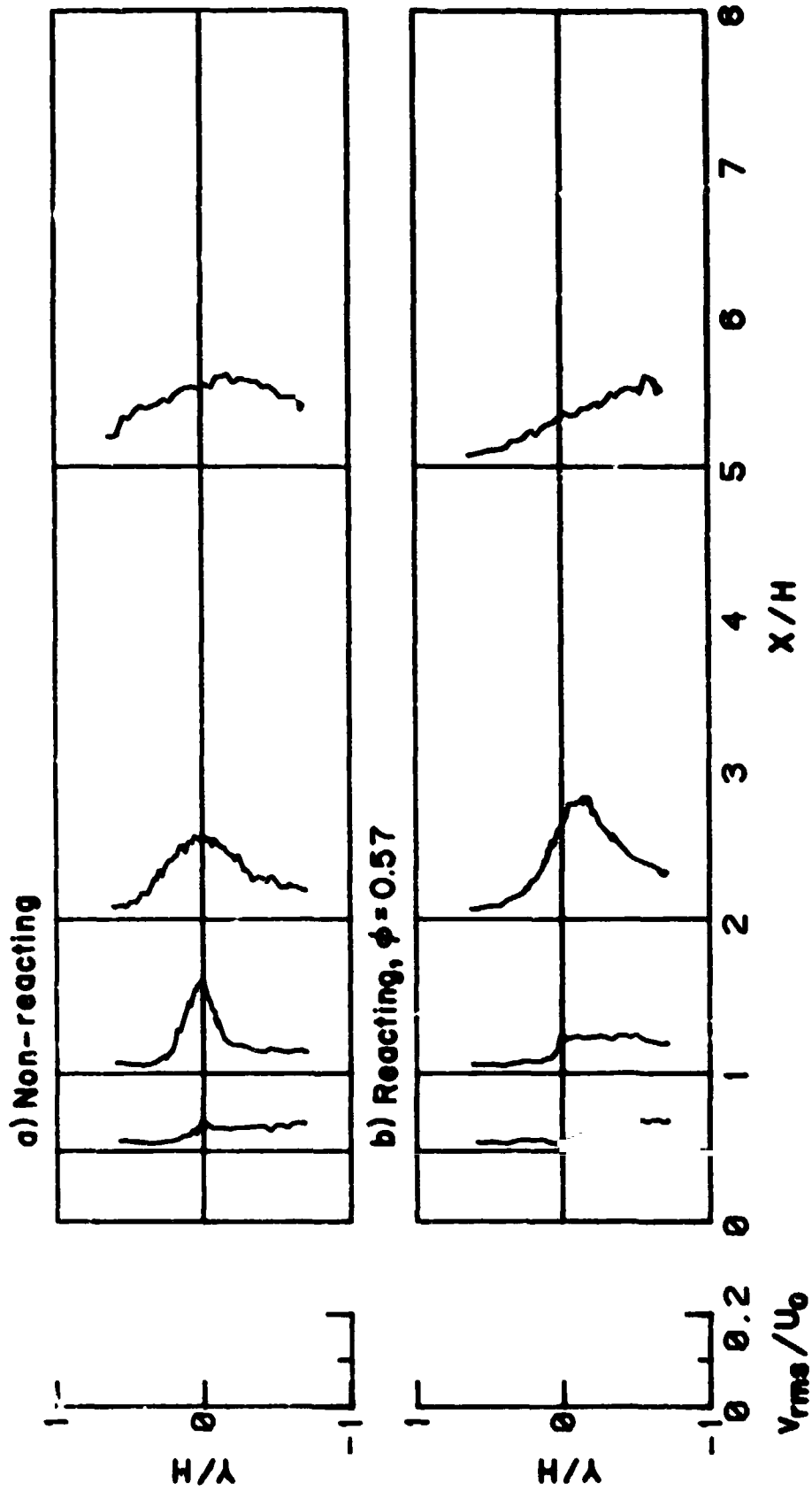


Figure 3.27 Transverse turbulence intensity profiles ($Re_H = 2.2 \times 10^4$, $U_0 = 13.3 \text{ m/s}$).

ORIGINAL PAGE IS
OF POOR QUALITY

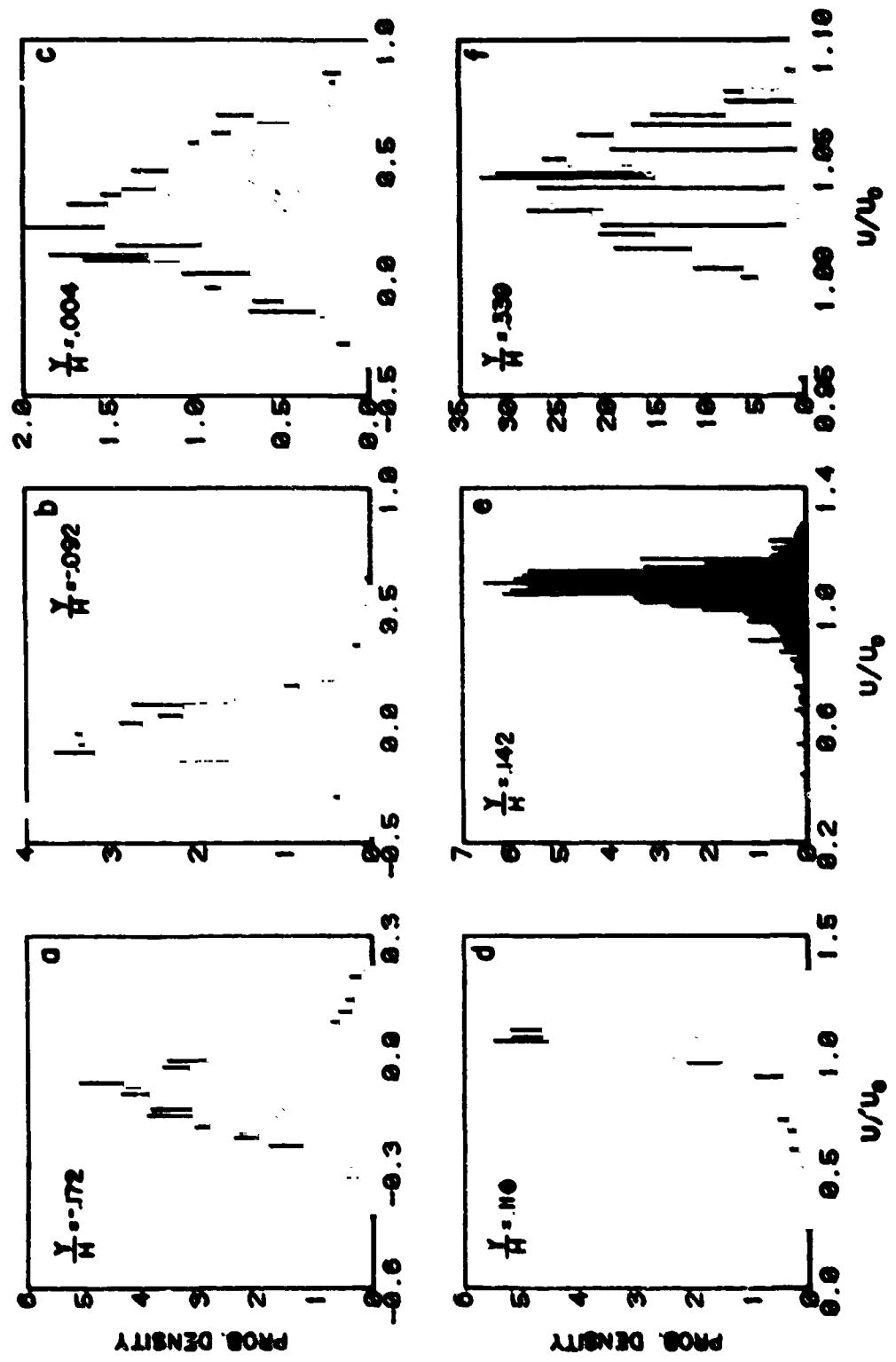
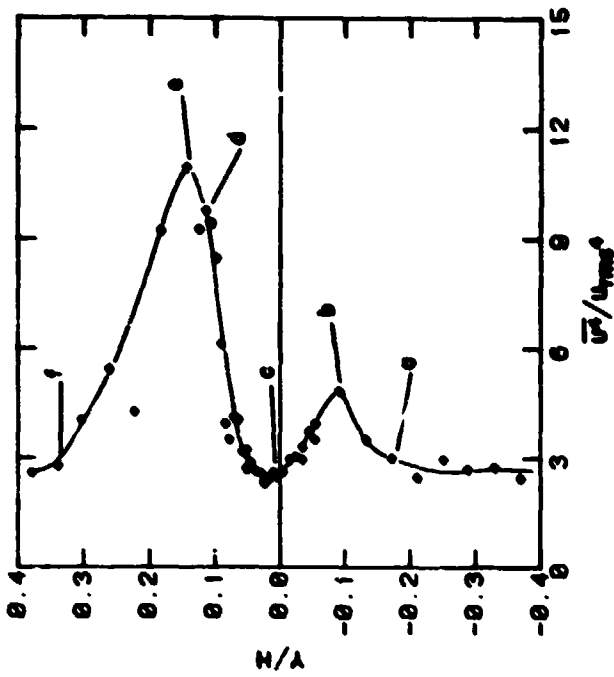
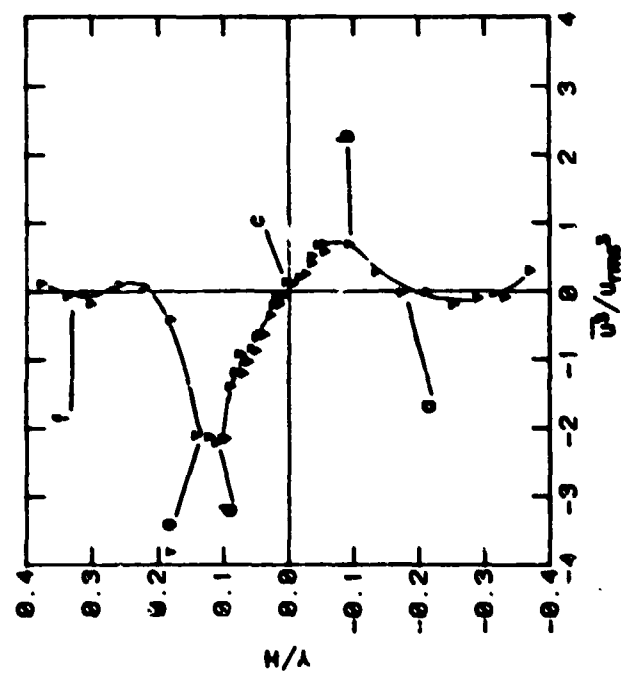


Figure 3.28 Streamwise velocity PDFs in the isothermal layer at $x/H = 1.0$
($Re_H = 1.5 \times 10^4$, $U_0 = 9.12$ m/s, $\phi = 0$).



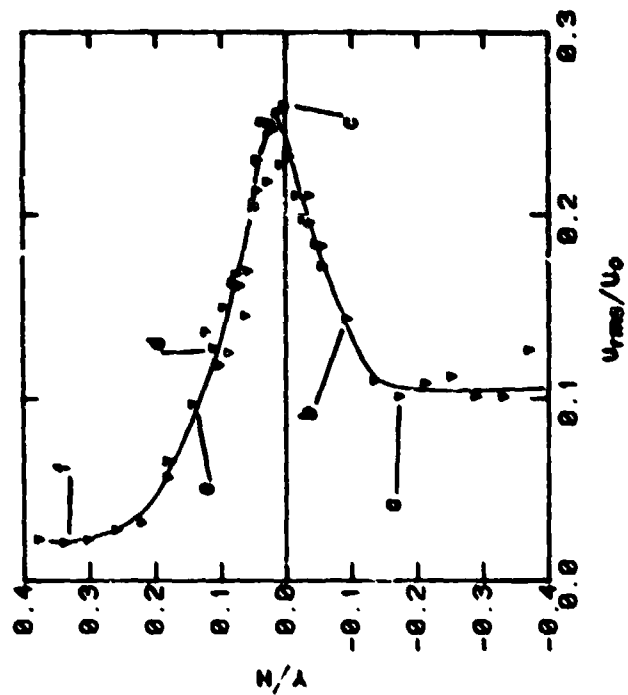
a) Skewness factor.



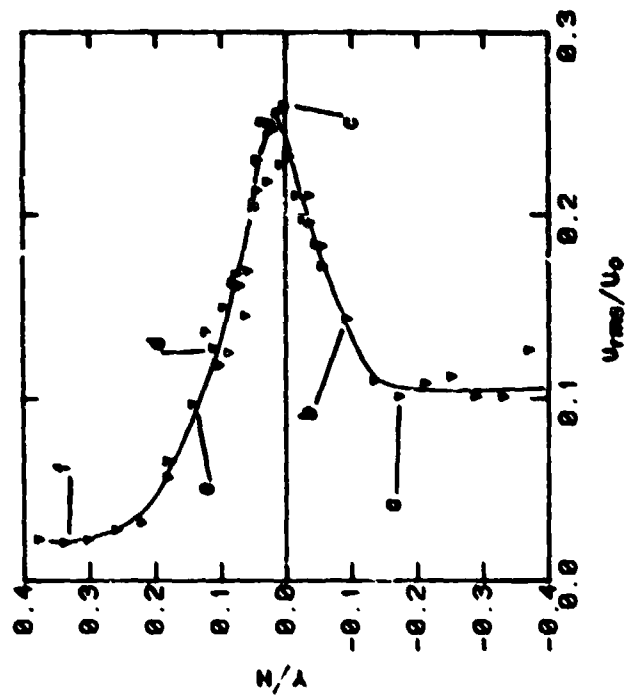
b) Flatness factor.

Figure 3.29 Streamwise velocity PDF moments in the isothermal layer at $x/H = 1.0$
($Re_H = 1.5 \times 10^6$, $U_0 = 9.12$ m/s, $\phi = 0$).

ORIGINAL FIGURES
OF POOR QUALITY



c) Mean velocity.



d) Turbulence intensity.

Figure 3.29 (See page 124 for caption).

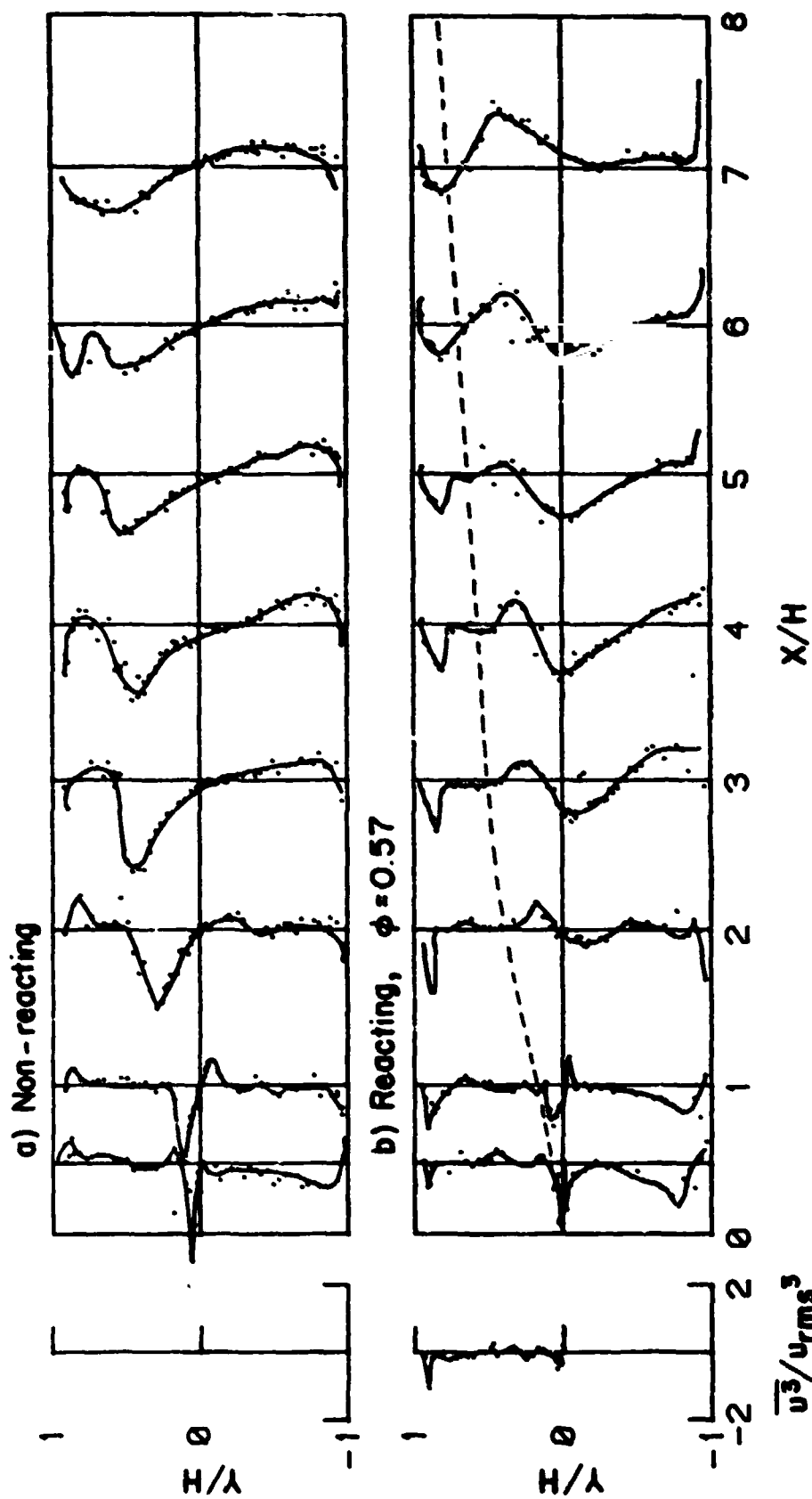


Figure 3.30 Skewness factors for the low Reynolds number flow
($Re_H = 1.5 \times 10^4$, $U_0 = 9.12$ m/s, --- flame boundary).

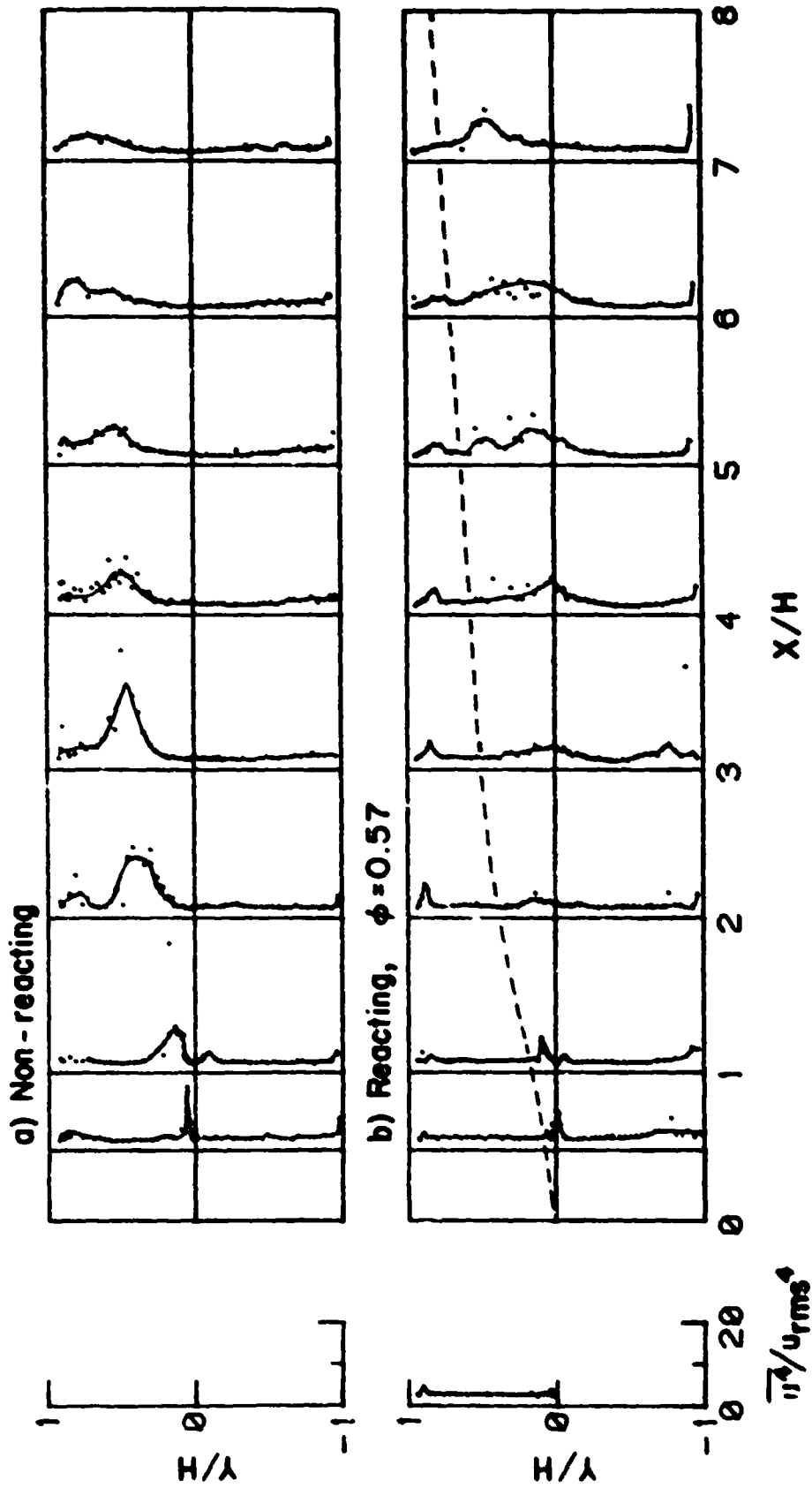


Figure 3.31 Flatness factors for the low Reynolds number flow
($Re_H = 1.5 \times 10^4$, $U_0 = 9.12$ m/s, --- flame boundary).

ORIGINAL PAGE IS
OF POOR QUALITY.

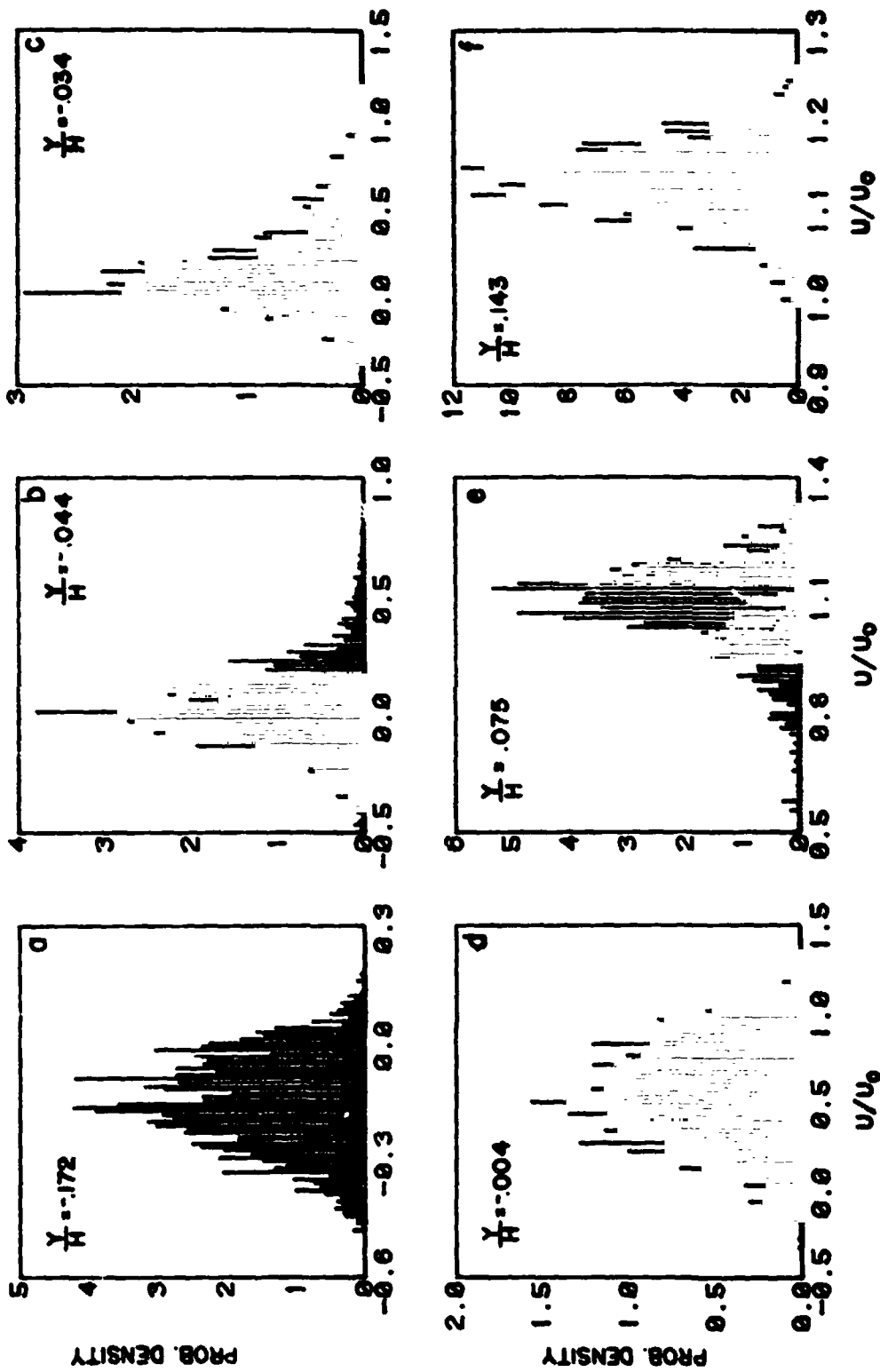
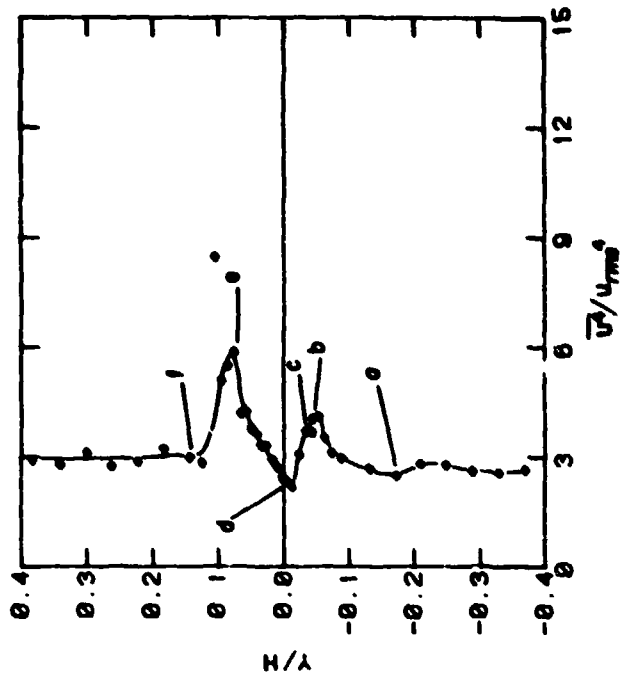
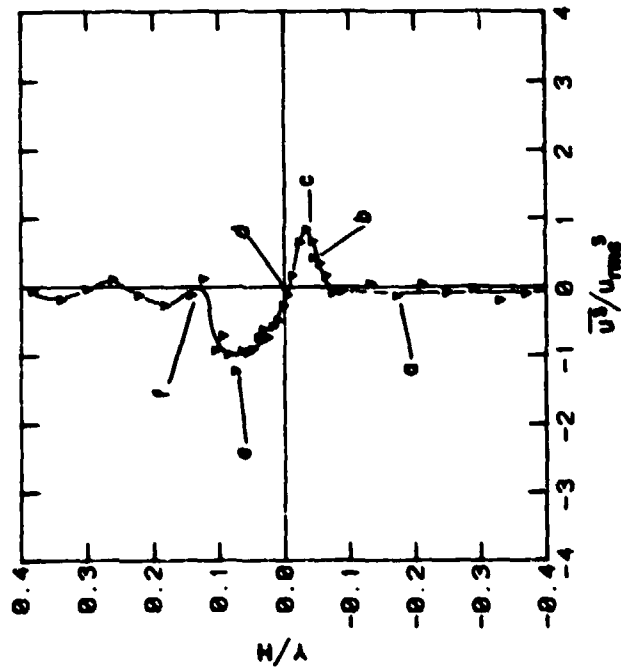


Figure 3.32 Streamwise velocity PDFs in the reacting layer at $x/H = 1.0$
($Re_H = 1.5 \times 10^4$, $U_0 = 9.12$ m/s, $\phi = 0.57$).

ORIGINAL PAGE IS
OF POOR QUALITY.



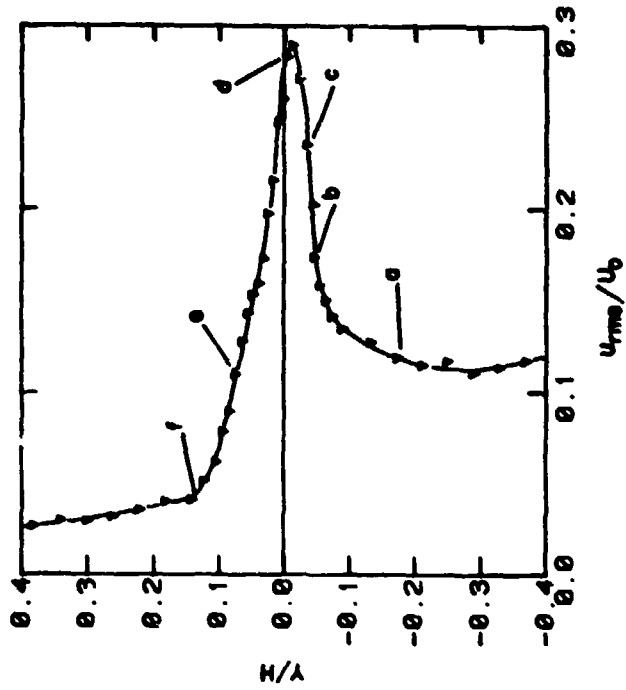
a) Skewness factor.



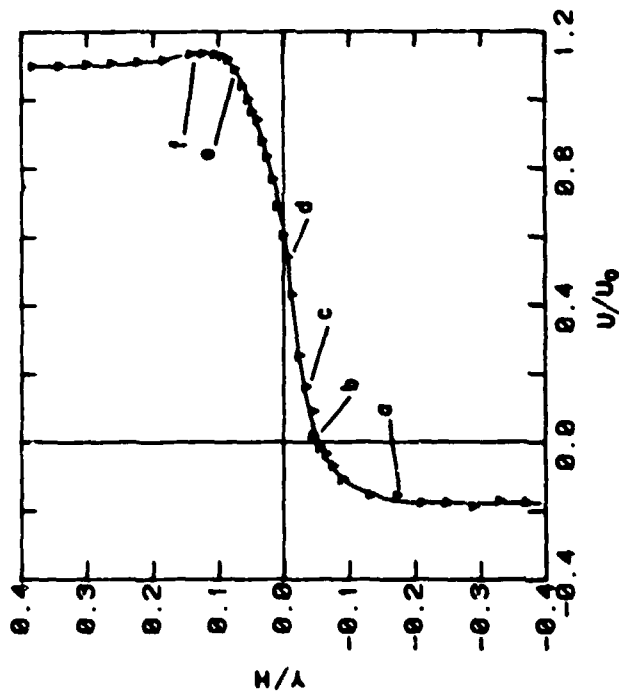
b) Flatness factor.

Figure 3.33 Streamwise velocity PDF moments in the reacting layer at $x/H = 1.0$
($Re_H = 1.5 \times 10^4$, $U_0 = 9.12$ m/s, $\phi = 0.57$).

ORIGINAL IMAGE IS
OF POOR QUALITY



d) Turbulence intensity.



c) Mean velocity.

Figure 3.33 (See page 129 for caption).

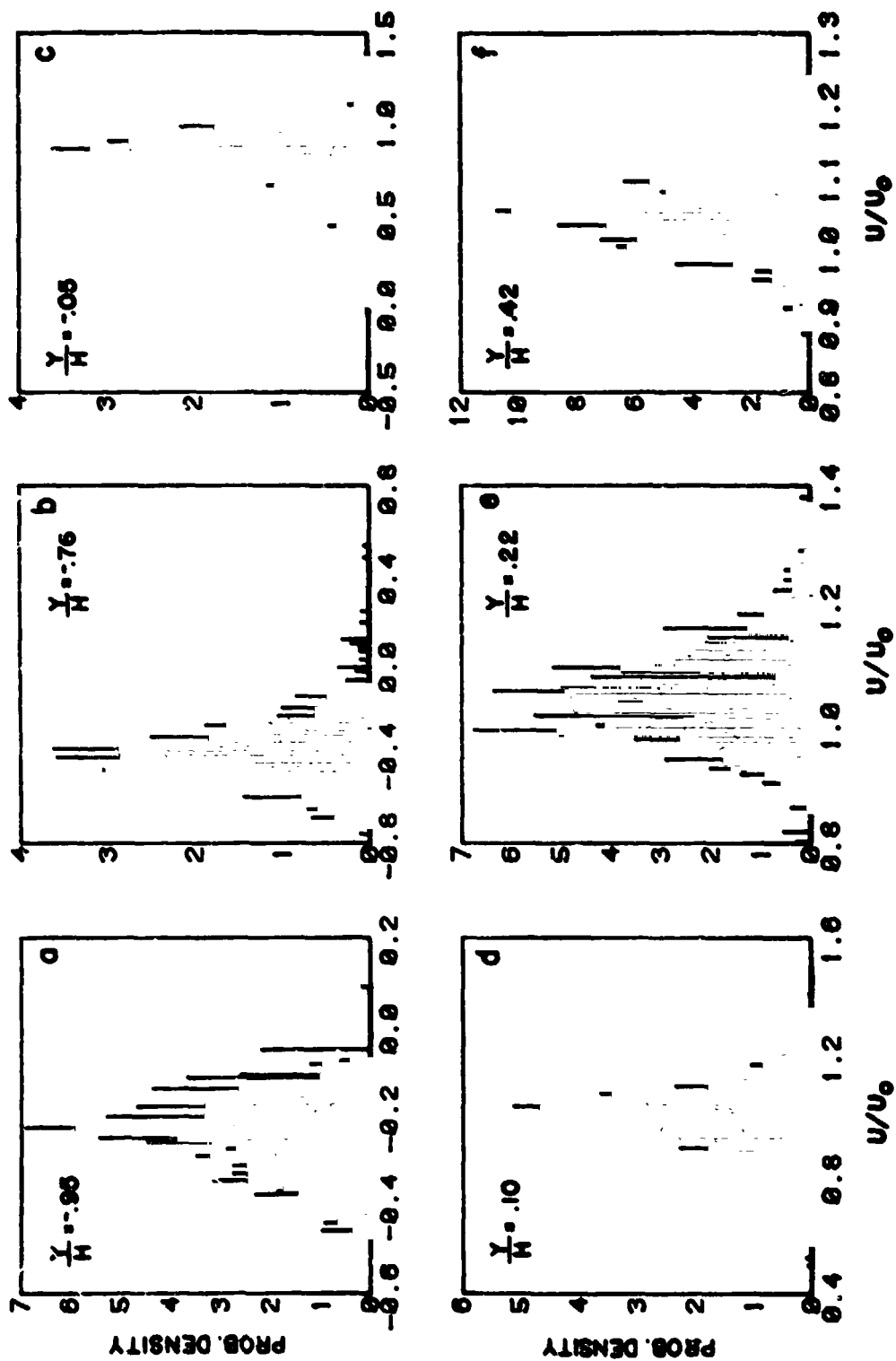
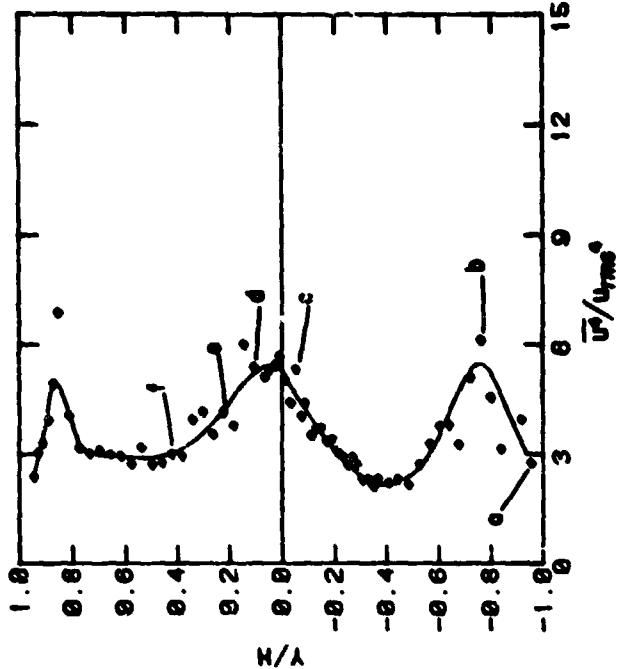
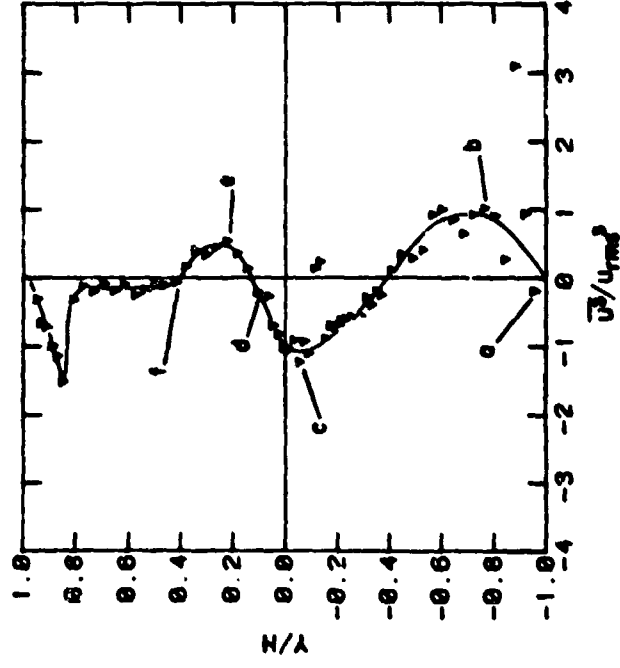


Figure 3.34 Streamwise velocity PDFs in the reacting flow at $x/H = 3.0$
($Re_H = 1.5 \times 10^4$, $U_0 = 9.12$ m/s, $\phi = 0.57$).

ORIGINAL PAGE IS
OF POOR QUALITY



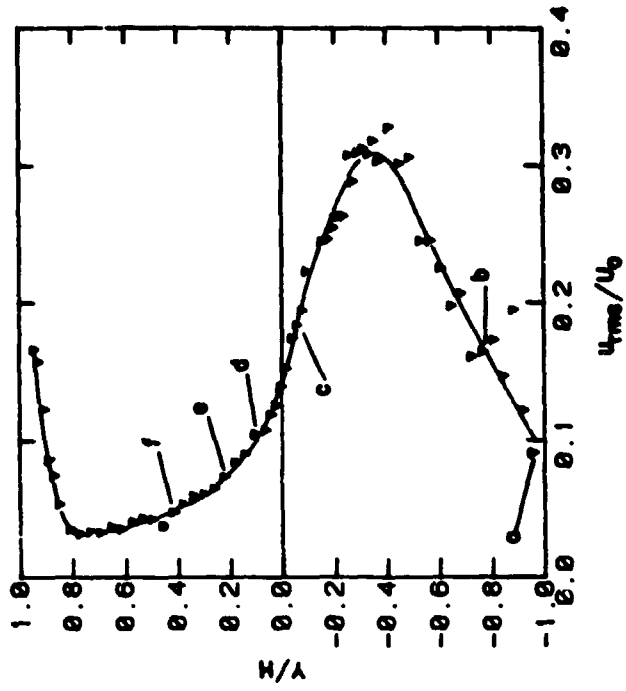
a) Skewness factor.



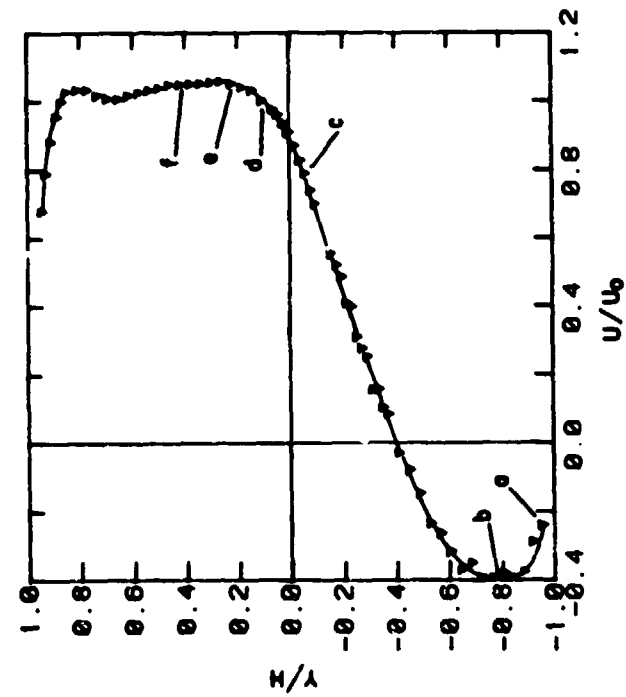
b) Flatness factor.

Figure 3.35 Streamwise velocity PDF moments in the reacting flow at $x/H = 3.0$
($ReH = 1.5 \times 10^4$, $U_0 = 9.12$ m/s, $\phi = 0.57$).

ORIGINAL FILE IS
OF POOR QUALITY.



c) Mean velocity.



d) Turbulence intensity.

Figure 3.35 (See page 132 for caption).

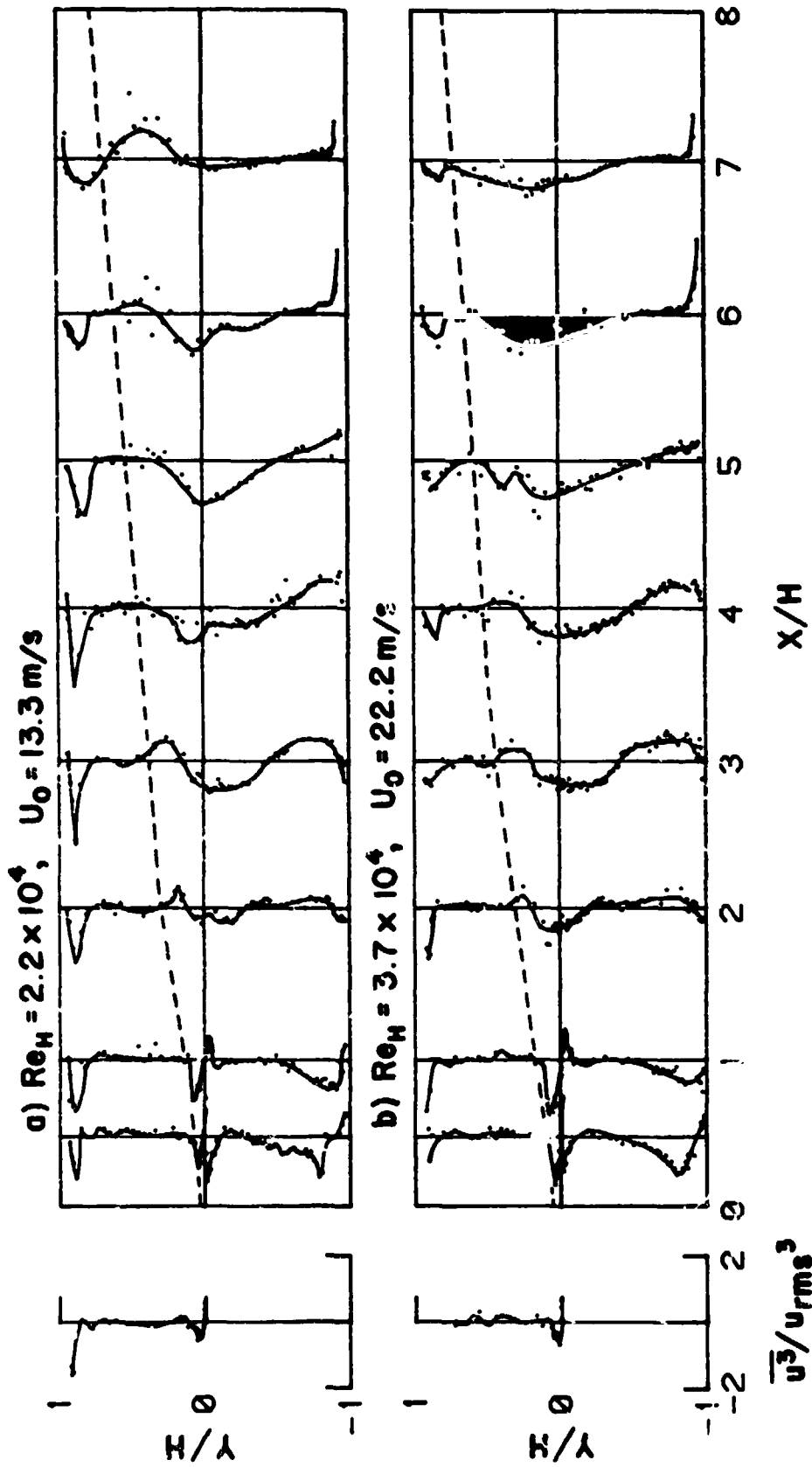


Figure 3.36 Skewness factors for the reacting flow at higher Reynolds numbers ($\phi = 0.57$, --- flame boundary).

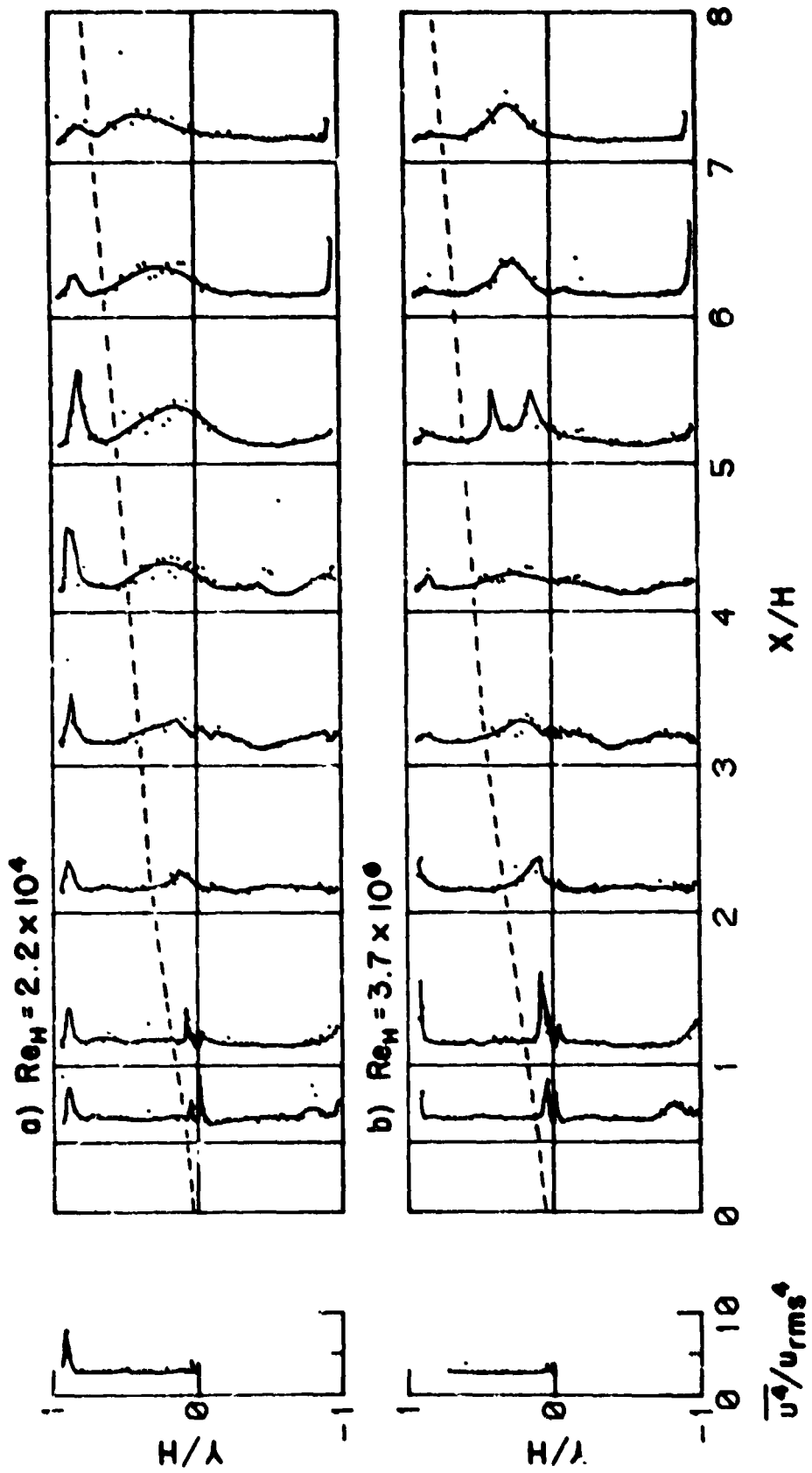


Figure 3.37 Flatness factors for the reacting flow at higher Reynolds numbers ($\phi = 0.57$, --- flame boundary).

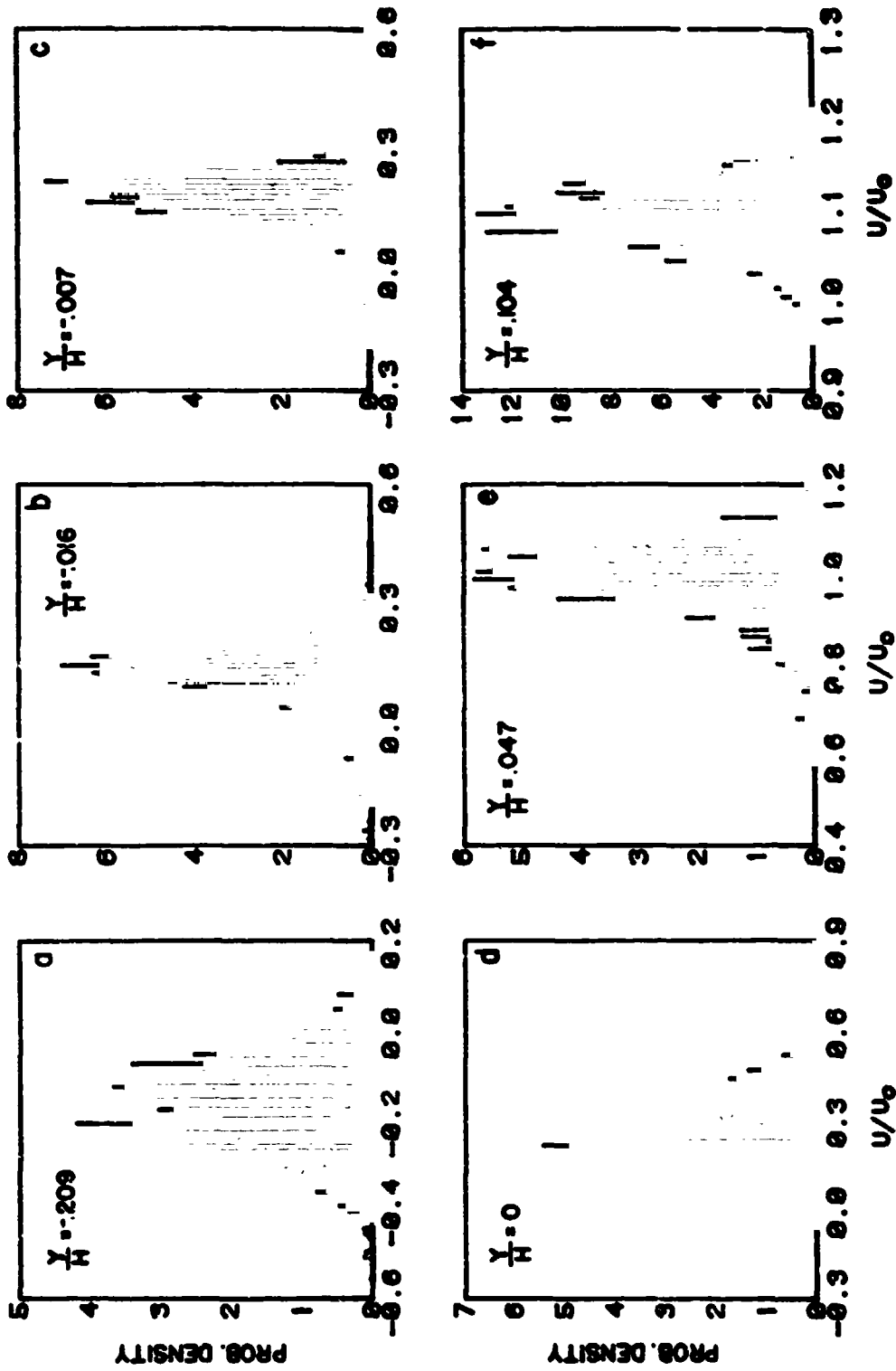
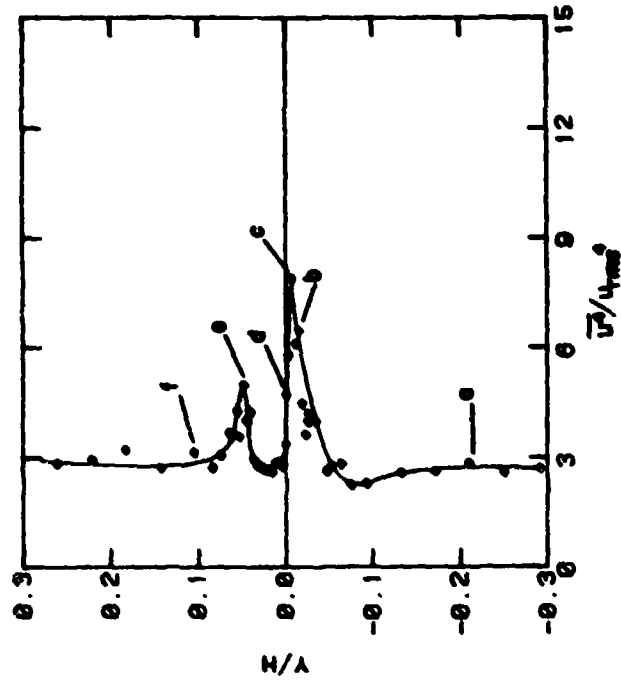
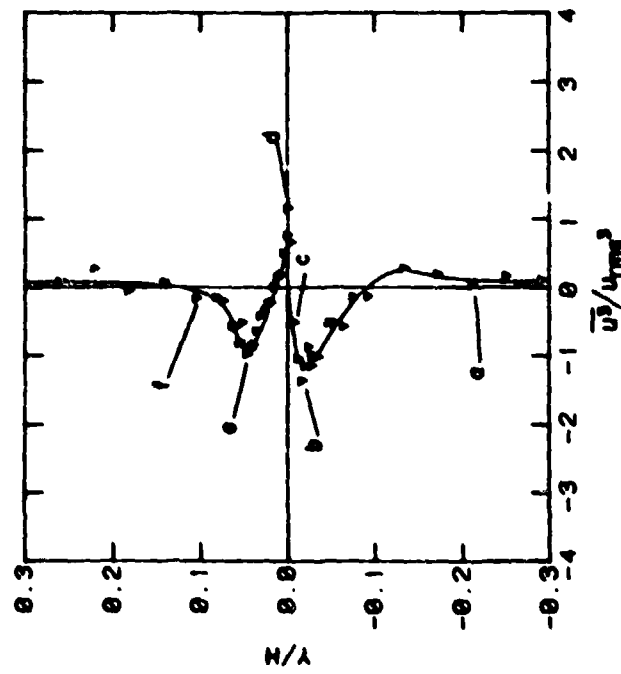


Figure 3.38 Streamwise velocity PDFs in the reacting layer at $x/H = 0.5$
($Re_H = 2.2 \times 10^4$, $U_0 = 13.3$ m/s, $\phi = 0.57$).

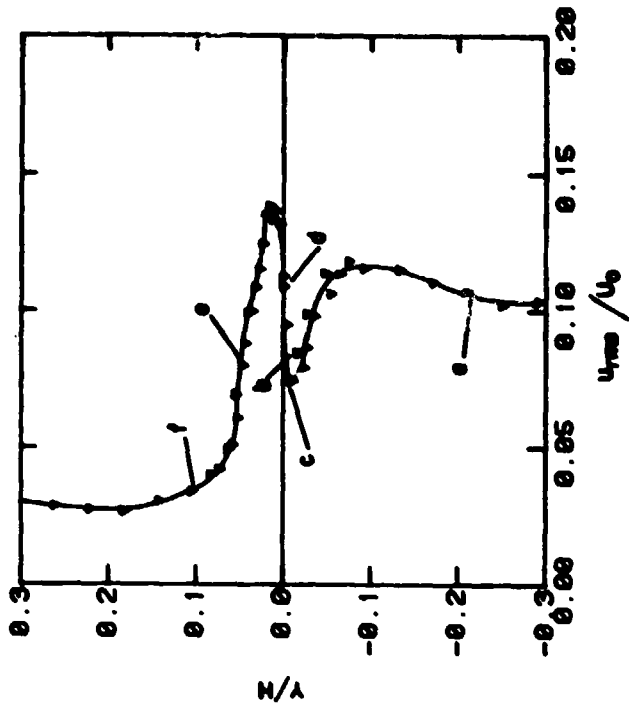


a) Skewness factor.

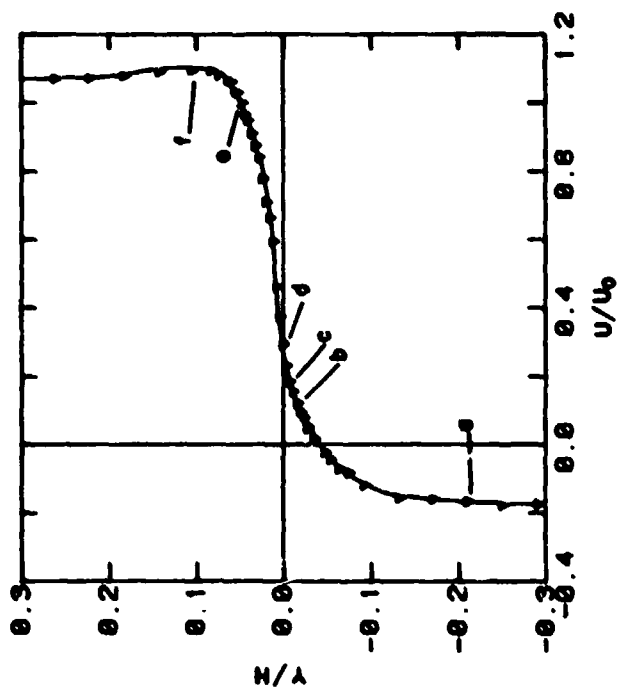


b) Flatness factor.

Figure 3.39 Streamwise velocity PDF moments in the reacting layer at $x/H = 0.5$
($Re_H = 2.2 \times 10^4$, $U_0 = 13.3$ m/s, $\phi = 0.57$).



d) Turbulence intensity.



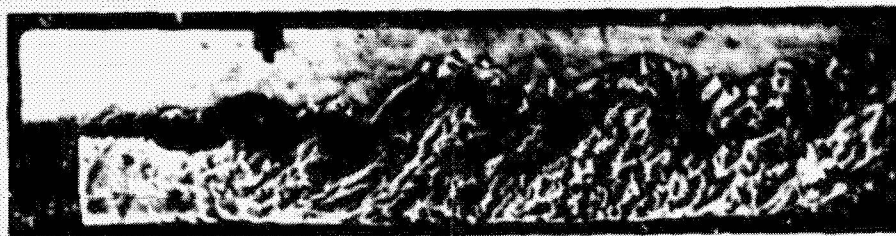
c) Mean velocity.

Figure 3.39 (See page 137 for caption).

a) $Re_H = 1.5 \times 10^4$, $\tau_{exp} = 74 \mu s$



b) $Re_H = 2.2 \times 10^4$, $\tau_{exp} = 49 \mu s$



c) $Re_H = 3.7 \times 10^4$, $\tau_{exp} = 51 \mu s$



0 2 4 6 8

Figure 3.40 Schlieren photographs of the reacting flow ($\phi = 0.57$).

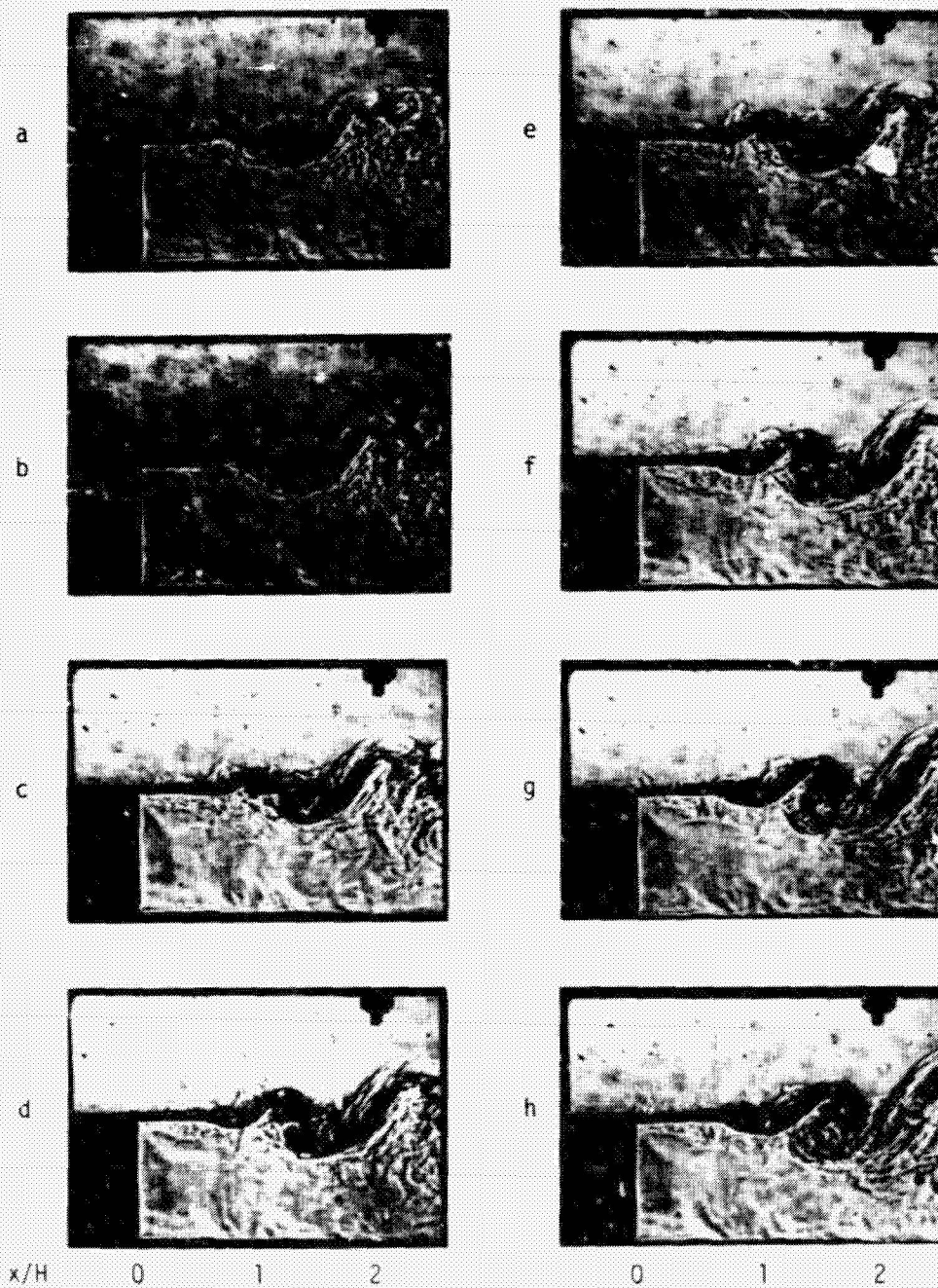


Figure 3.41 Sequence of schlieren photographs showing eddy coalescence ($Re_H = 2.2 \times 10^4$, $c = 0.57$, $\tau_{exp} = 5 \mu s$, 0.3 ms apart).

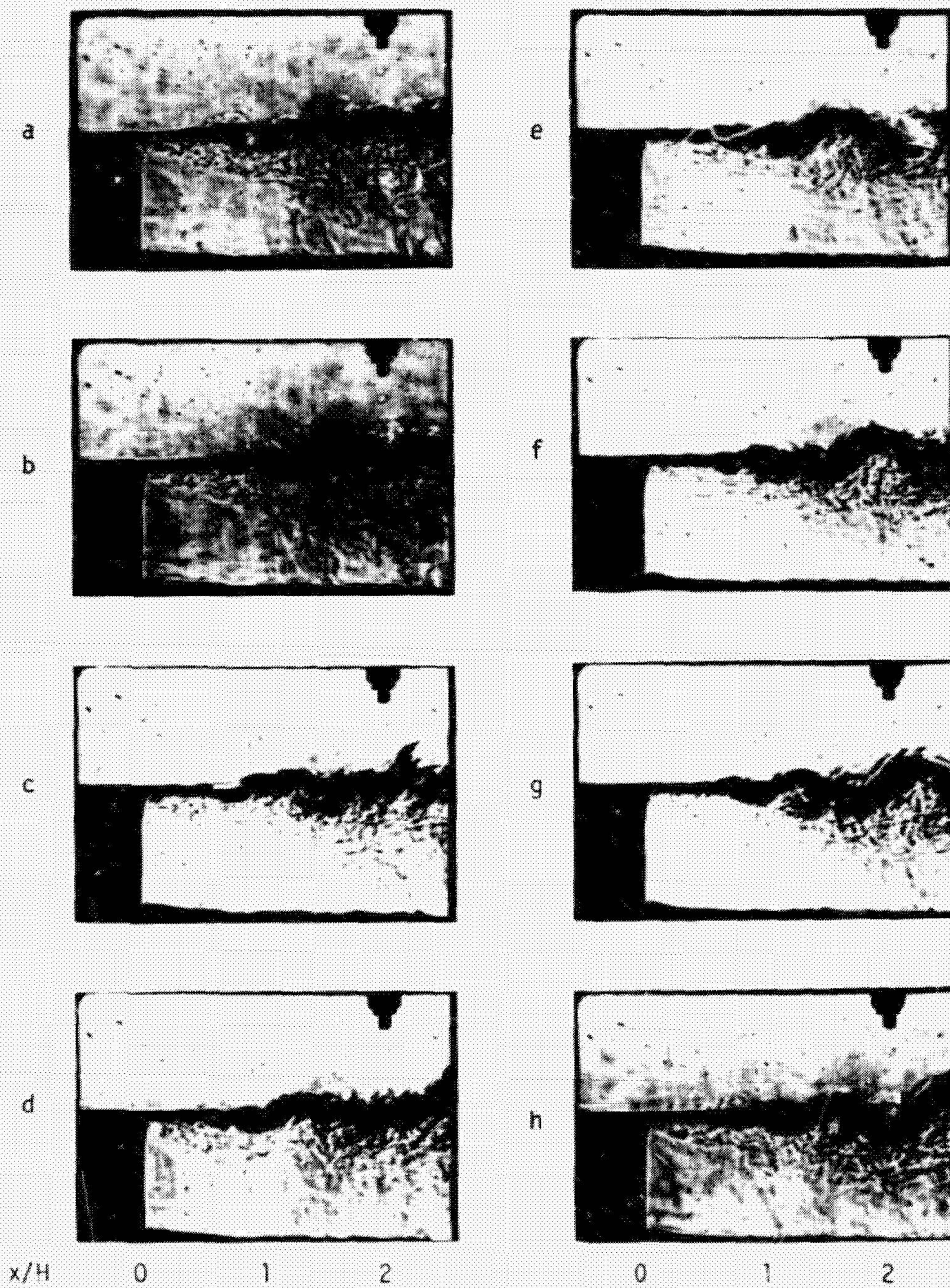
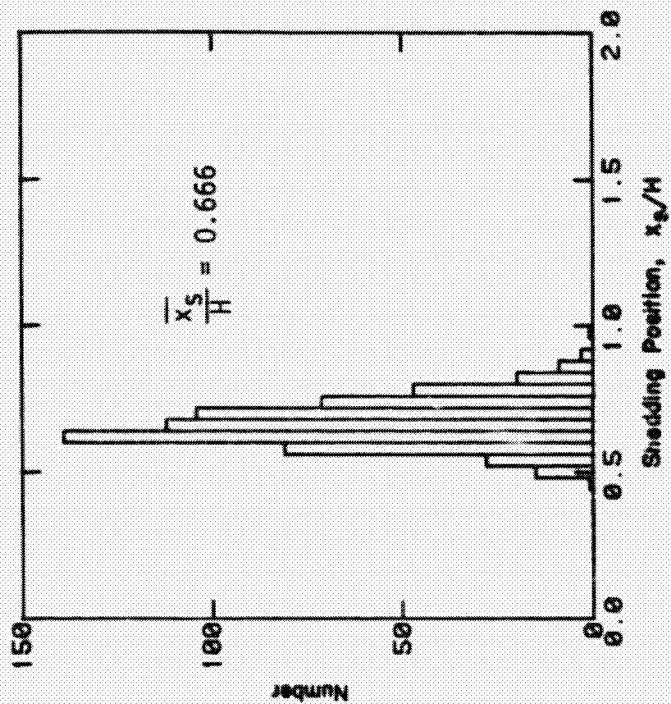
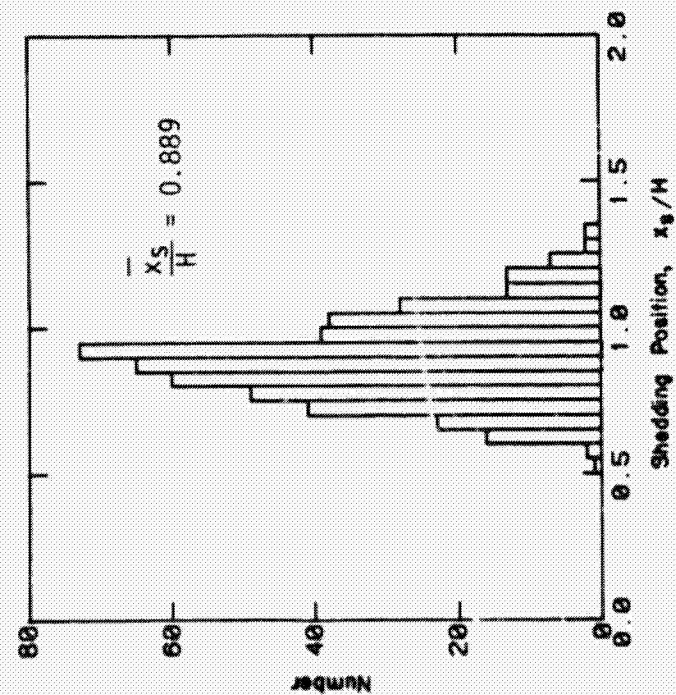


Figure 3.42 Sequence of schlieren photographs at the high entrance Reynolds number ($Re_H = 3.7 \times 10^4$, $\phi = 0.57$, $\tau_{exp} = 58\mu s$, 0.6 ms apart).

ORIGINAL PAGE IS
OF POOR QUALITY



a) $Re_H = 1.5 \times 10^4$



b) $Re_H = 2.2 \times 10^4$

Figure 3.43 Histograms of the eddy shedding position in the reacting shear layer ($\phi = 0.57$).

ORIGINAL PAGE IS
OF POOR QUALITY

143



Figure 3.44 Long exposure schlieren photograph of the reacting flow
($Re_H = 2.2 \times 10^5$, $\phi = 0.57$, $\tau_{exp} = 33$ ms).

ORIGINAL PAGE IS
OF POOR QUALITY

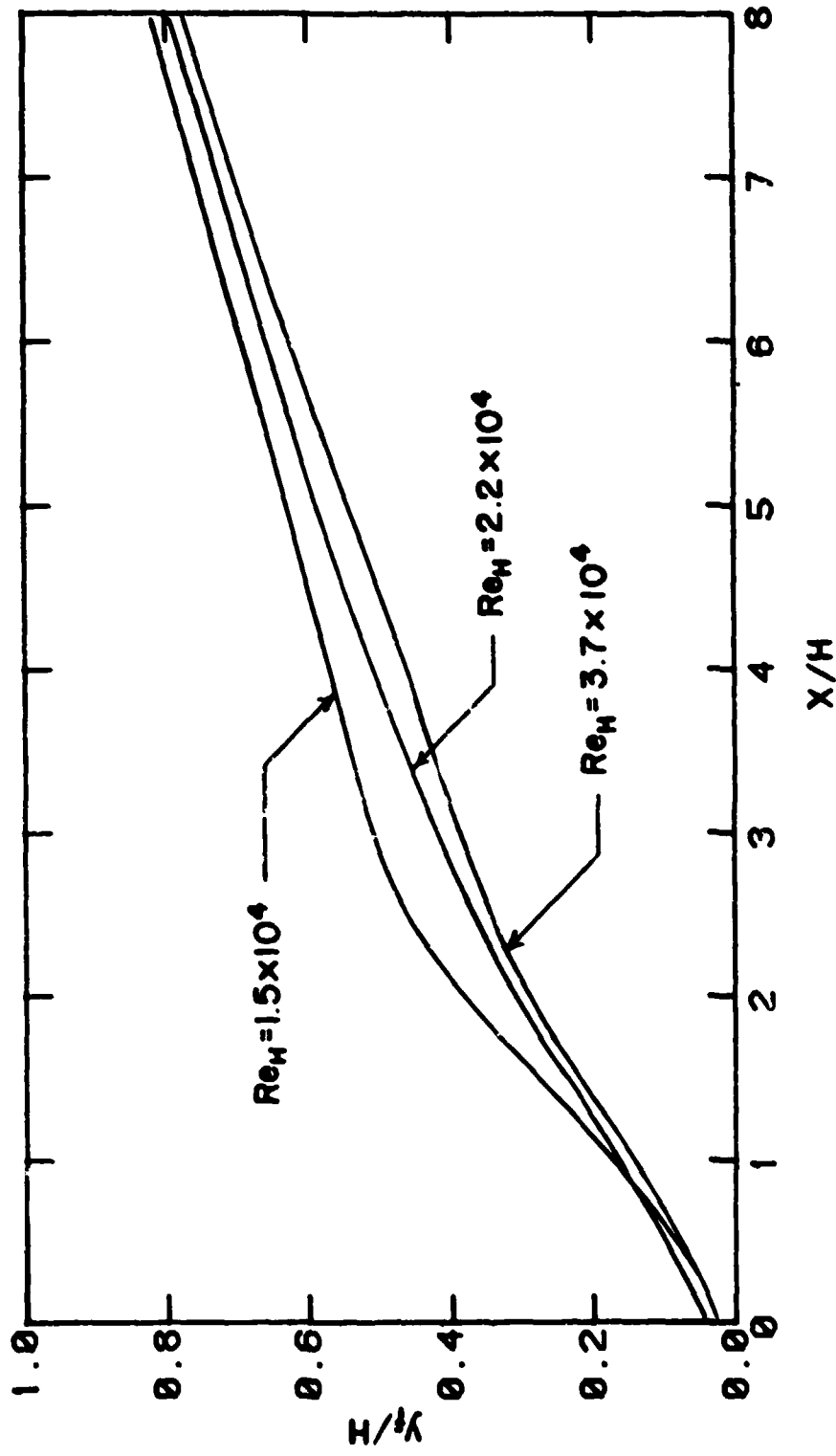


Figure 3.45 The upper boundary of the flame from long exposure schlieren photographs ($\phi = 0.57$).

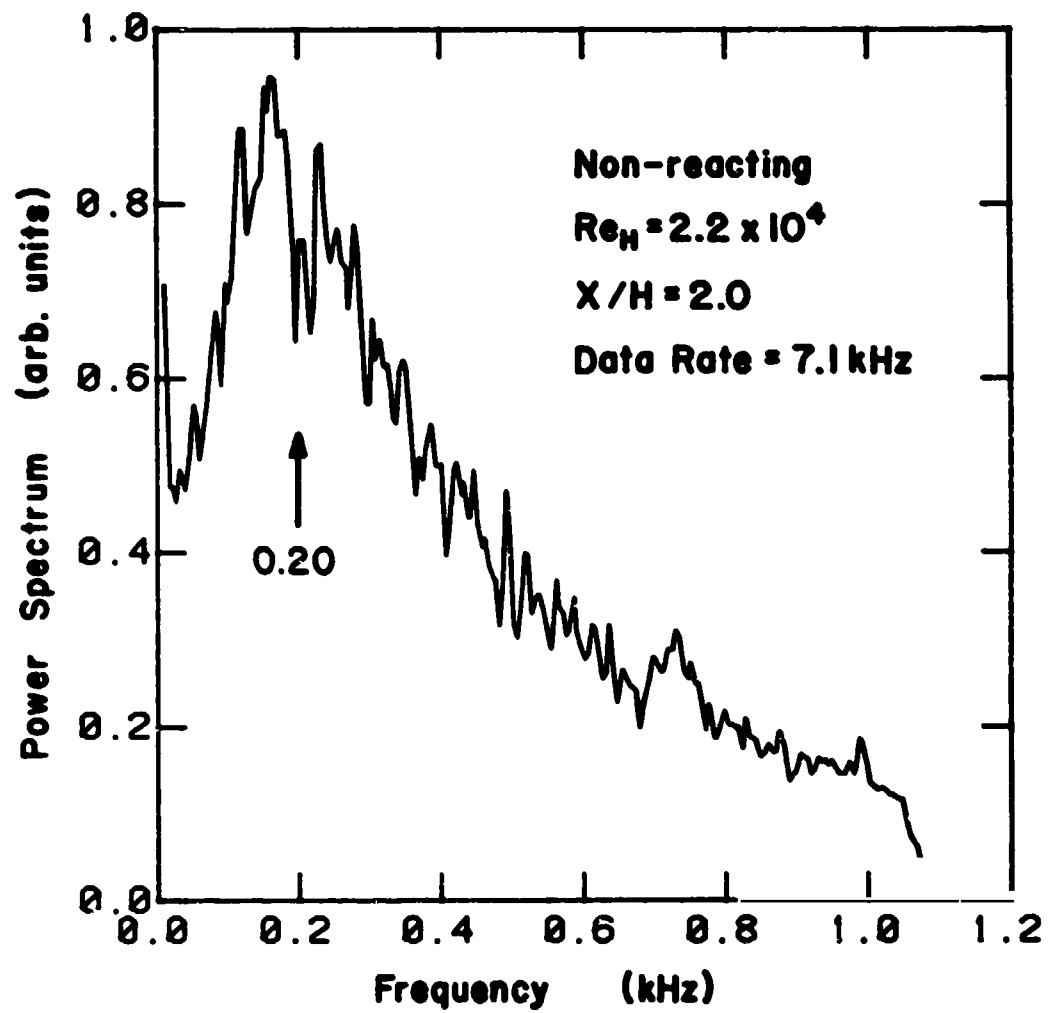
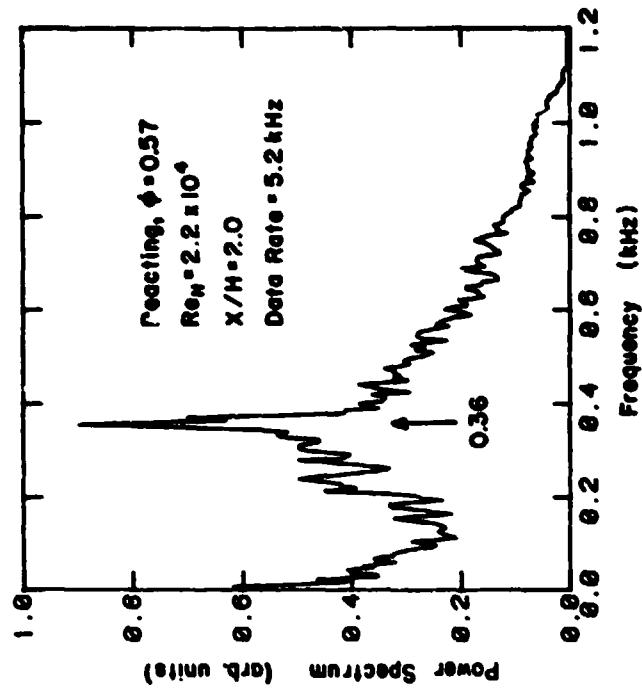
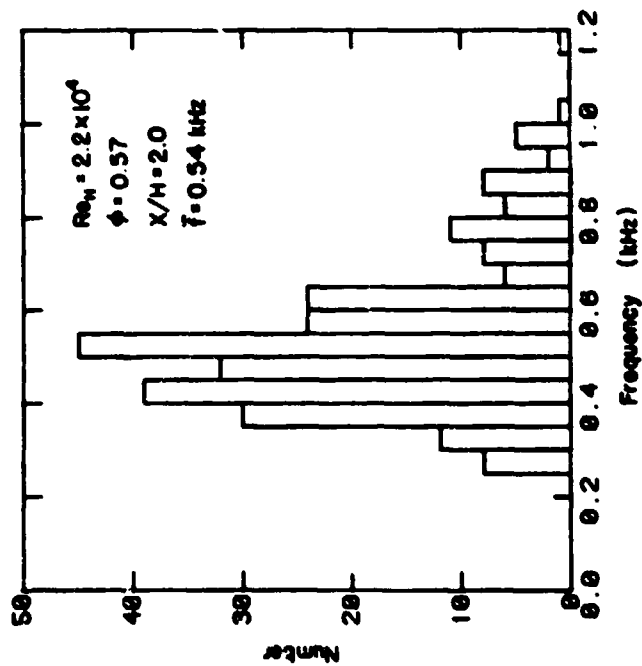
OF THE SPECTRUM
OF POOR QUALITY.

Figure 3.46 Frequency spectrum of the v-velocity in the non-reacting shear layer.

ORIGINAL RECORD
OF POOR QUALITY

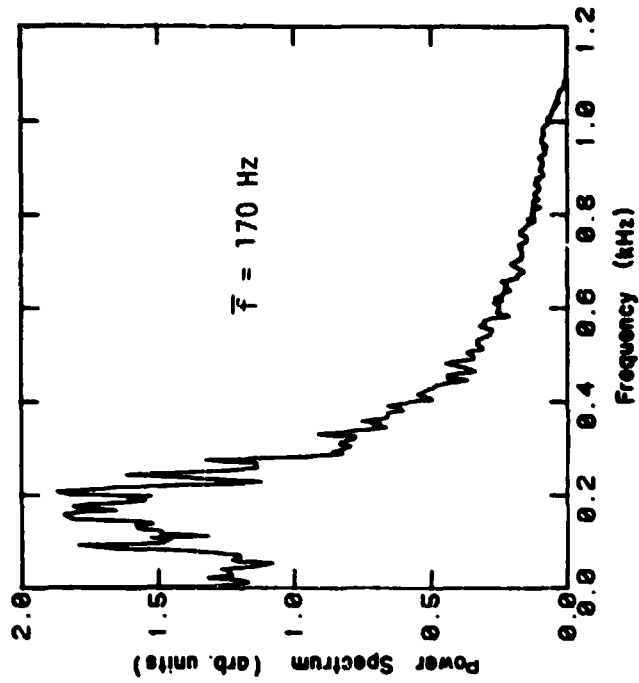


b) LDV spectra of v-velocity component.

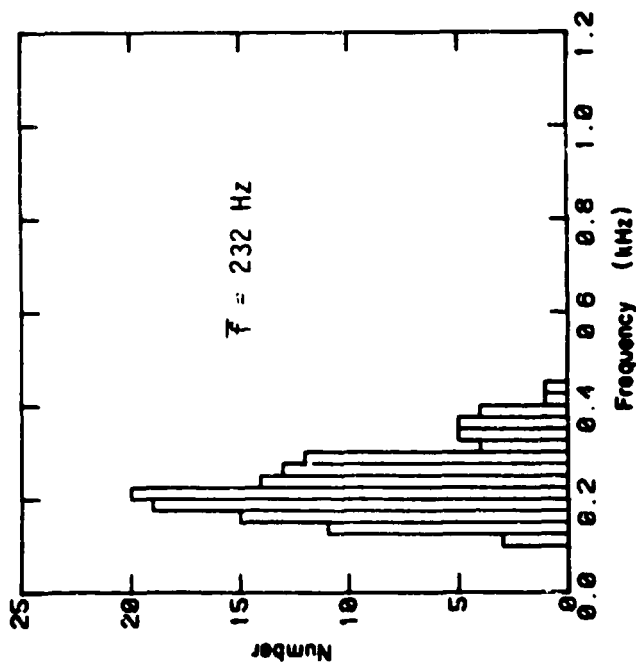


a) Histogram from schlieren movies.

Figure 3.47 Passing frequency of the large scale structures in the reacting shear layer.



b) LDV spectra of the v-velocity component.



a) Histogram from schlieren movies.

Figure 3.48 Passing frequency of the large scale structures in the reacting flow beyond reattachment ($x/H = 7$, $\phi = 0.57$).

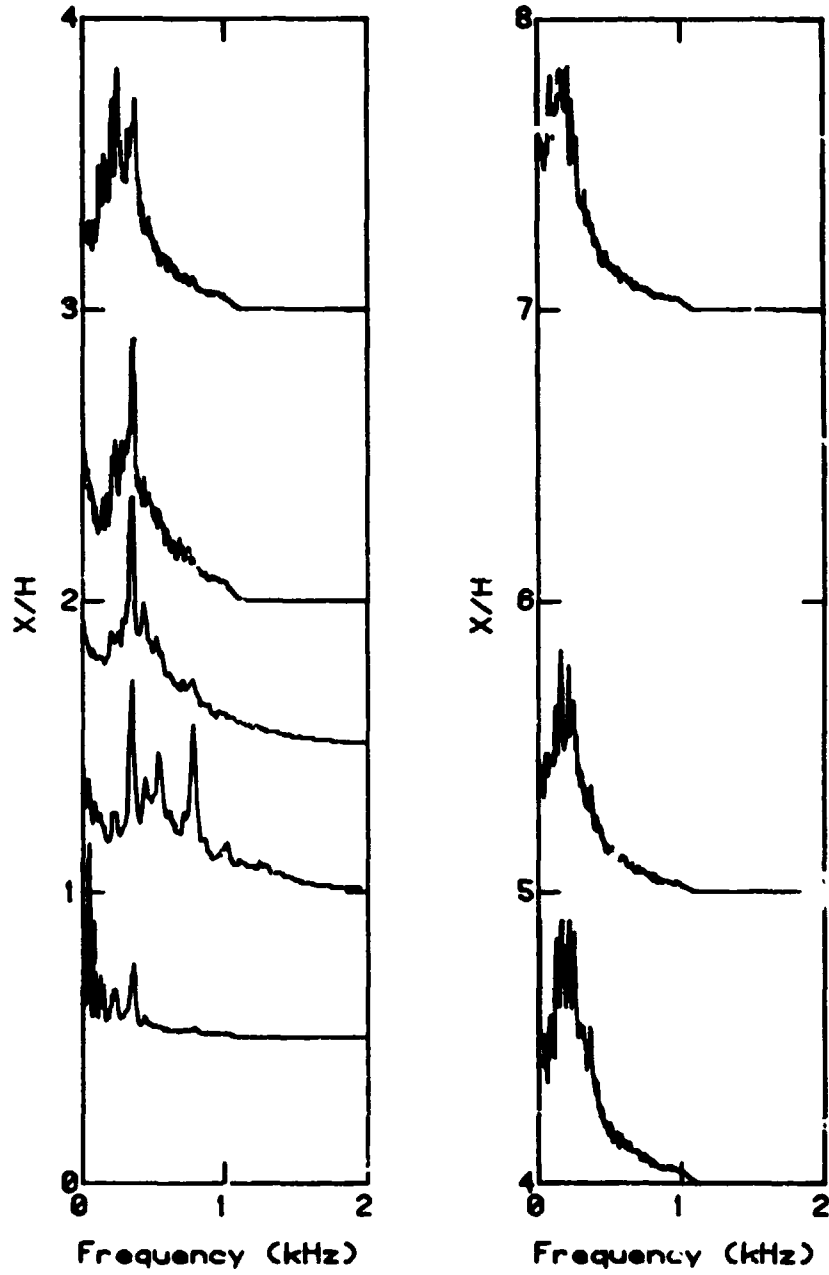


Figure 3.49 Sequence of LDV spectra taken in the reacting flow ($Re_H = 2.2 \times 10^4$, $\phi = 0.57$, v-velocity component)

MEASUREMENTS OF THE
 OF POOR QUALITY.

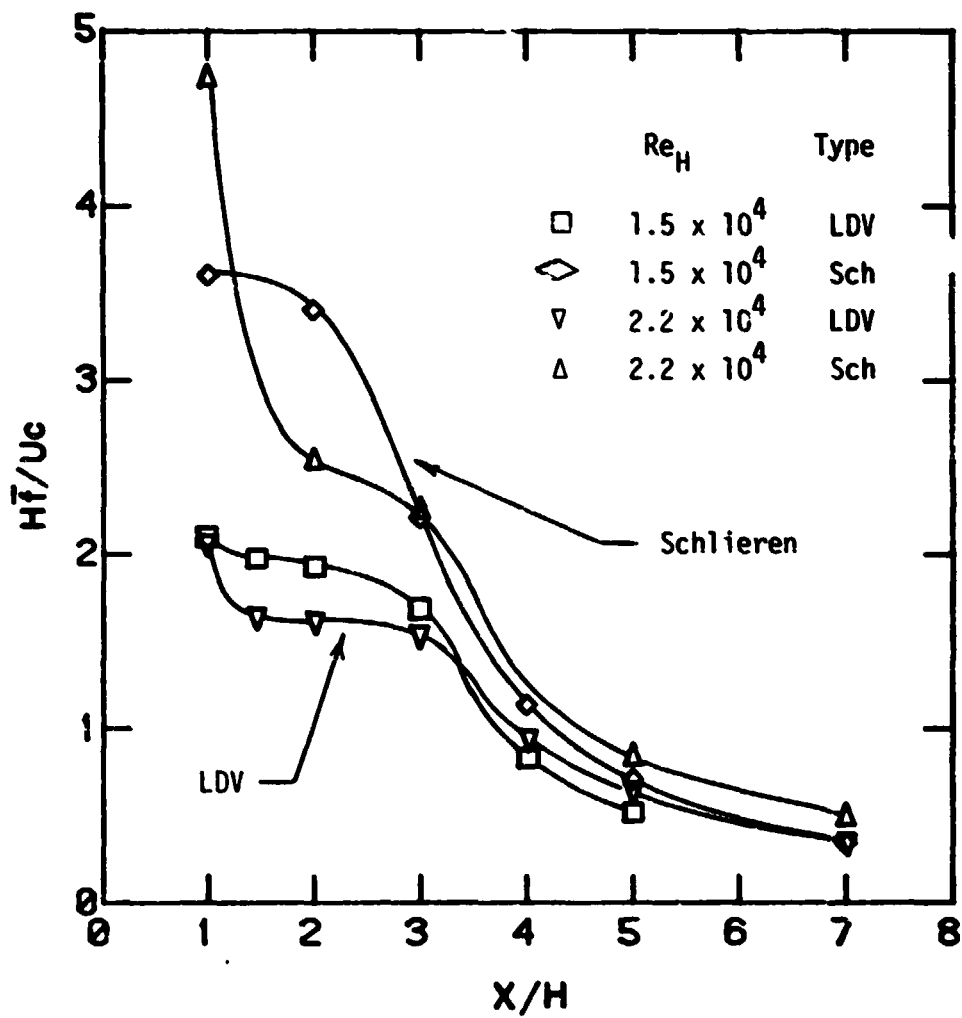


Figure 3.50 Strouhal number based on step height determined from schlieren and LDV measurements.

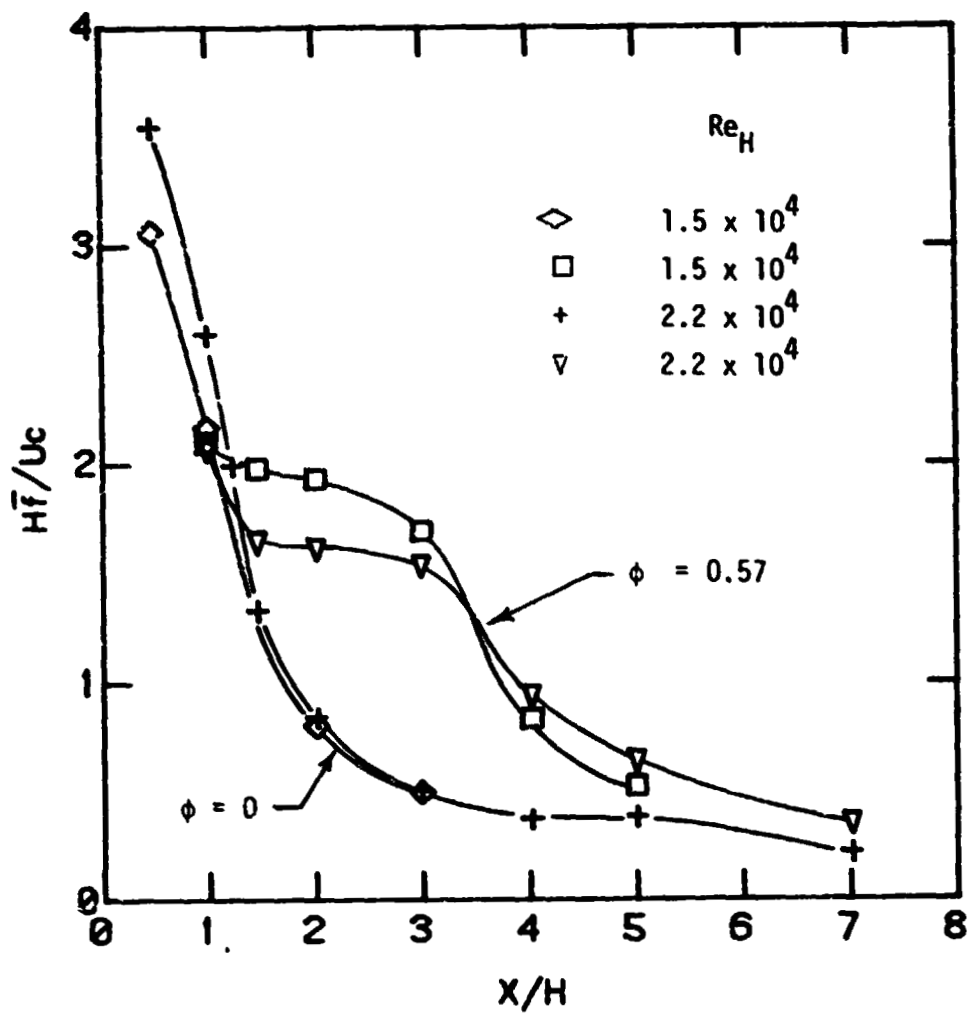


Figure 3.51 Strouhal number based on step height from LDV spectra.

ORIGINAL SOURCE
OF POOR QUALITY

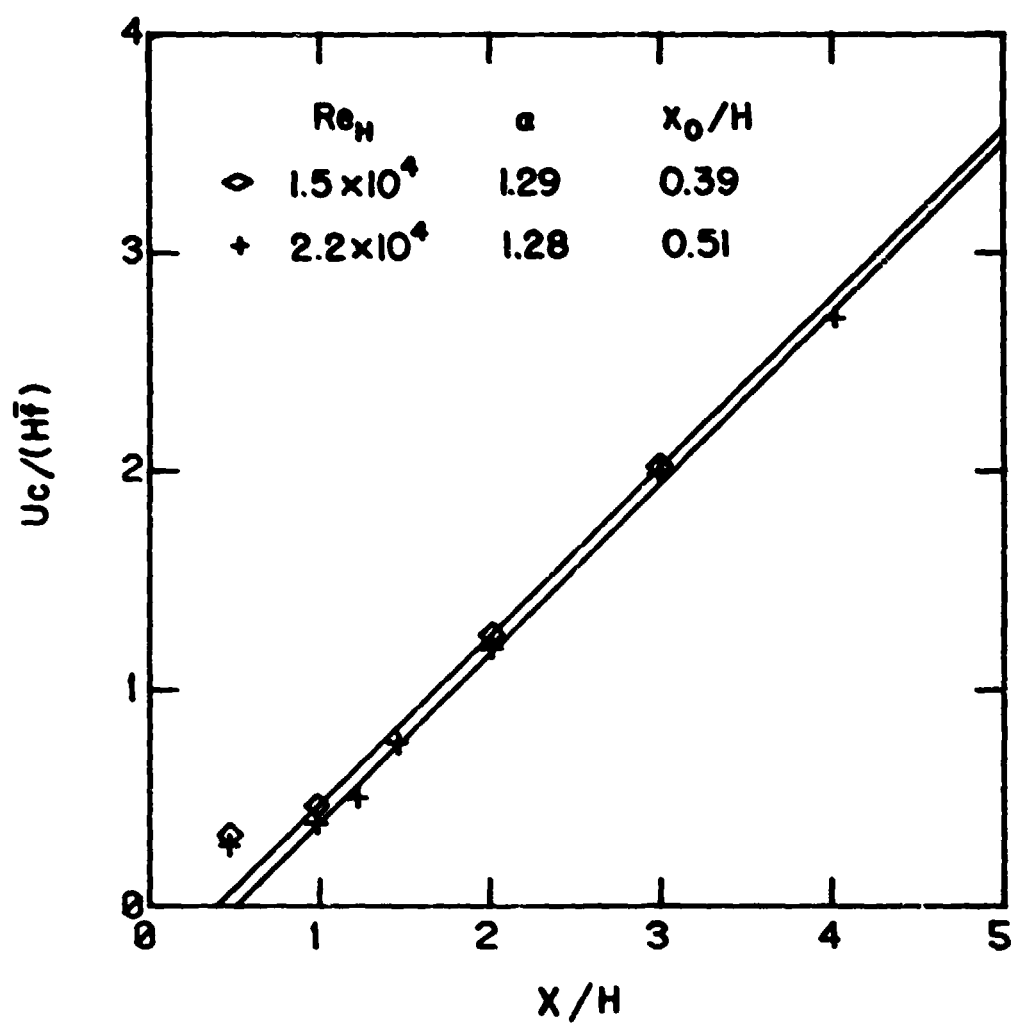


Figure 3.52 Inverse Strouhal number based on the step height for the isothermal layer.

ORIGINAL SOURCE
OF POOR QUALITY

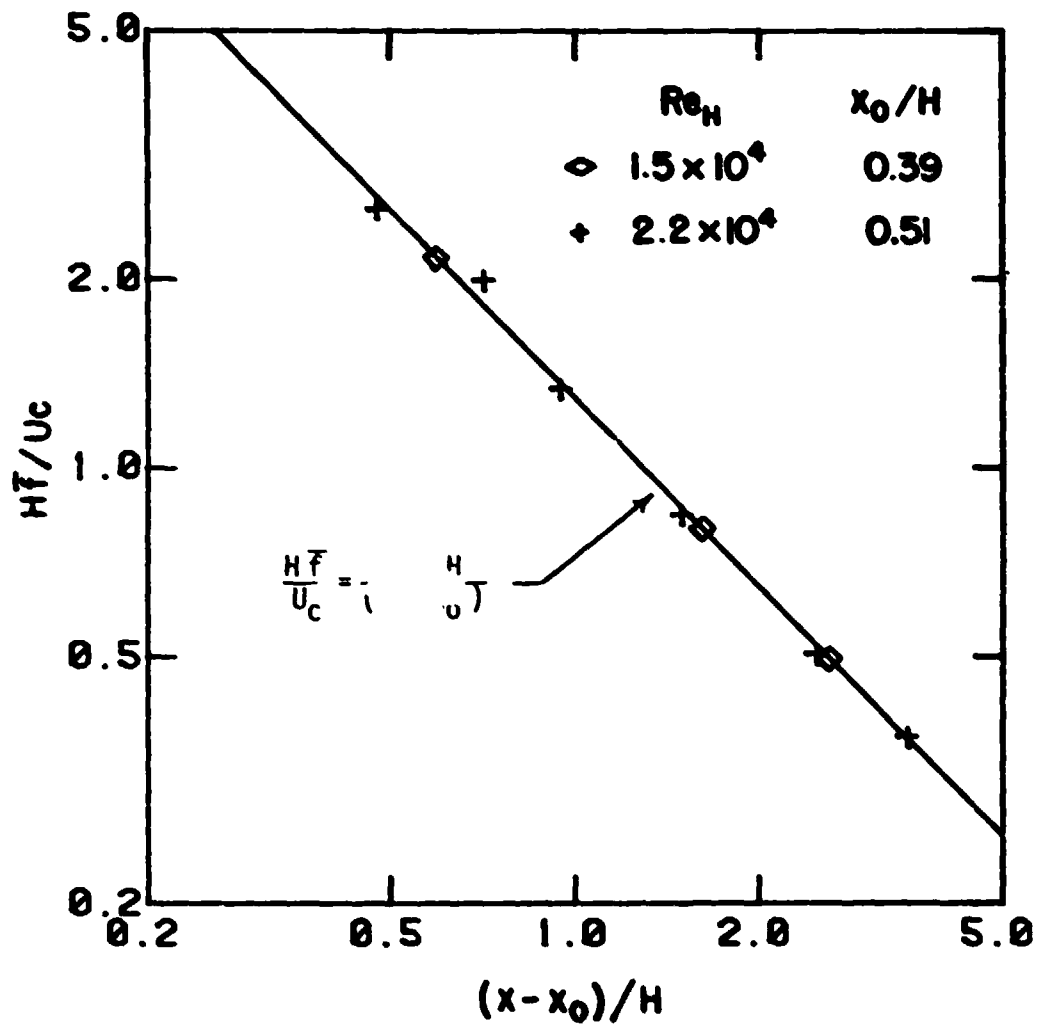


Figure 3.53 Strouhal number based on the step height for the isothermal data in mixing layer coordinates.

UNIVERSITY
OF TORONTO

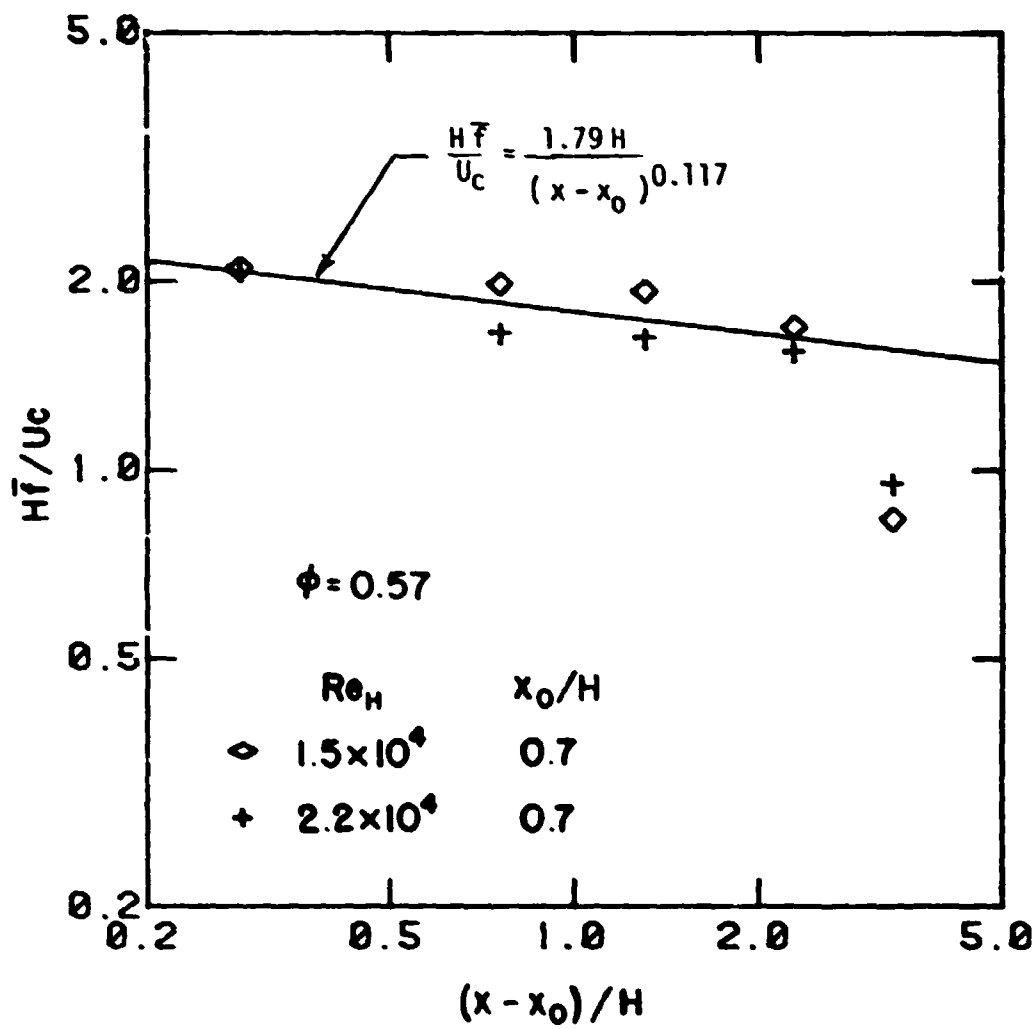


Figure 3.54 Strouhal number based on step height for the reacting data in mixing layer coordinates.

ORIGINAL PAGE IS
OF POOR QUALITY

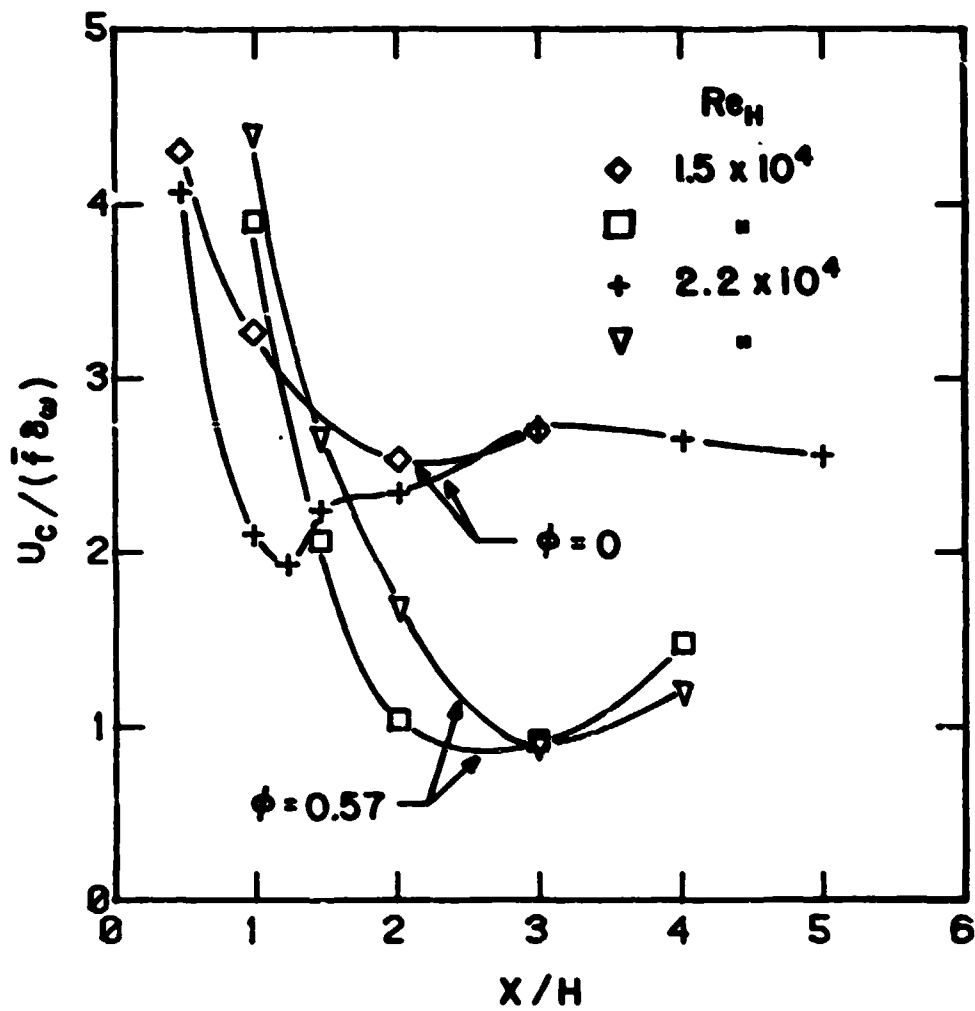


Figure 3.55 Inverse Strouhal number based on vorticity thickness from LDV spectra.

Chapter 4

SUMMARY AND CONCLUSIONS

The primary aim of this work is to assess the effect of combustion on the rearward-facing step flow. The flow field is documented by laser Doppler velocimetry measurements of the turbulent velocity and high speed schlieren visualization. The results and conclusions of the investigation with regard to the different aspects of the flow field are given in the following sections.

Initial Conditions

The state of the initial boundary layer at separation is determined. The boundary layer is partially tripped having high turbulence levels with a laminar profile. This partial tripping has two effects. The linear growth rate region of the shear layer is increased and the virtual origin appears downstream of the step.

Mean Velocity Flow Field

The mean velocity flow field is measured for both reacting non-reacting flow. The primary effects of combustion are:

1. The virtual origin of the reacting shear layer defined by the mean velocity profiles appears farther downstream of the step but the growth rate of the shear layer is unchanged.
2. In the reacting shear layer, the flame as seen from schlieren observations propagates faster into the incoming inviscid reactants than the shear layer defined by the mean velocity.
3. The reacting shear layer defined by the mean velocity is shifted toward the recirculation zone. Heat expansion from the reacting eddies propagating into the premixed reactants increases the

velocity at the top of the layer and lowers the upper boundary of the shear layer defined by the mean velocity. Heat expansion increases the velocity difference in the lower edge of the shear layer and causes it to grow into the recirculation zone more rapidly.

4. The reattachment length of the reacting shear layer is shortened by 30% due to the shift of the shear layer toward the recirculation zone. The transverse velocity (v) also shows this downward shift.

Turbulence Development

The turbulence intensity and the higher order moments of the streamwise turbulence are measured throughout the flow field with the following results:

1. Combustion causes the peak positions of the turbulence intensity profiles to shift toward the recirculation zone confirming the mean velocity results.
2. The turbulence levels decrease rapidly 1 - 2 step heights before reattachment for both reacting and non-reacting cases due to curvature effects.
3. In the reacting layer, the maximum turbulence levels are 30% higher and have a double-peak in their variation with x .
4. For the shear layer defined by mean velocity, the non-Gaussian behavior is similar for both the non-reacting and reacting conditions.
5. Under combustion, there is non-Gaussian behavior above the shear layer defined by the mean velocity. The velocity PDF is positively skewed from the impelling effect of large scale

structures expanding between the top of the shear layer and the upper flame boundary.

6. The streamwise velocity PDFs are double-peaked in the reacting shear layer near the step. The PDFs are single-peaked in all other cases. Intermittent formation of the large scale structures near the step in the reacting layer could have caused the double-peak.

Large Scale Structure Development

The large scale structures are observed with high speed schlieren photography and frequency analysis of the LDV signal. The following observations are made:

1. As reported by Ganji and Sawyer (1980), the large scale structures are found to control the overall structure of the reacting shear layer. Reaction occurs within the eddies as they entrain premixed reactants and hot products. The growth of the large scale structures is tied to the propagation of the flame.
2. The formation of the eddies is delayed in the reacting shear layer as the local Reynolds number is reduced by combustion.
3. As seen from the schlieren visualization, the propagation of the flame into the incoming reactants extends above the shear layer defined by the mean velocity profiles. The upper edge of the reacting large scale structures defines the flame boundary.
4. The most striking effect of combustion is the reduction of eddy coalescence in the reacting shear layer. The pairing process is nearly eliminated as a growth mechanism in the reacting layer. The layer grows primarily by entrainment of fluid and heat expansion.

REFERENCES

- Adrian, R. J., and R. J. Goldstein (1971), "Analysis of a Laser Doppler Anemometer," J. Phys. E: Instrum., 4, 505.
- Ashurst, W. T. (1979), "Calculation of Plane Sudden Expansion Flow Via Vortex Dynamics," Presented at the 2nd Symposium on Turbulent Shear Flows, Imperial College, London, July.
- Batt, R. G. (1975), "Some Measurements on the Effect of Tripping the Two-Dimensional Shear Layer," AIAA J., 13, 245-247.
- Batt, R. G. (1977), "Turbulent Mixing of Passive and Chemically Reacting Species in a Low-Speed Shear Layer," J. Fluid Mech., 82, 53-95.
- Birch, S. F. (1977), "On the Developing Region of a Plane Mixing Layer," Turbulence in Internal Flows, S. N. B. Murthy, editor, Hemisphere Publ., Washington.
- Birch, S. F. (1980), "Data Evaluation Report for Free Mixing Layers," Report prepared for the 1980/81 Stanford Conferences on Complex Turbulent Flows.
- Bradshaw, P. (1966), "The Effect of Initial Conditions on the Development of a Free Shear Layer," J. Fluid Mech., 26, 225-236.
- Bradshaw, P., and F. Y. F. Wong (1972), "The Reattachment and Relaxation of a Turbulent Shear Layer," J. Fluid Mech., 52, 113-135.
- Breidenthal, R. E. (1978), "A Chemical Reacting Turbulent Shear Layer," Ph. D. Thesis, California Institute of Technology.
- Browand, F. K., and B. O. Latigo (1978), "The Growth of the Two Dimensional Mixing Layer From a Turbulent and Non-Turbulent Boundary Layer," SQUID Report USC-1-PU.
- Brown, G. L. and A. Roshko (1974), "On Density Effects and Large Structure in Turbulent Mixing Layers," J. Fluid Mech., 64, 775-816.
- Castro, I. P. and P. Bradshaw (1976), "The Turbulent Structure of a Highly Curved Mixing Layer," J. Fluid Mech., 73, 265-304.
- Chandrsuda, C., R. D. Mehta, A. D. Weir, and P. Bradshaw (1978), "Effect of Free-Stream Turbulence on Large Structure in Turbulent Mixing Layers," J. Fluid Mech., 85, 693-704.
- Chigier, N. A. (1977), "Combustion Diagnostics by Laser Velocimetry," Experimental Diagnostics in Gas Phase Combustion

- Systems**, Ben T. Zinn, editor, **Progress in Astronautics and Aeronautics**, vol. 53, AIAA, New York.
- Chorin, A. J. (1973), "Numerical Study of Slightly Viscous Flow," J. Fluid Mech., 57, 785-796.
- de Brederode, V., and P. Bradshaw (1972), "Three-Dimensional Flow in Nominally Two-Dimensional Separation Bubbles I. Flow Behind a Rearward Facing Step," Imperial College Aero. Report 72-19.
- Dimotakis, P. E. (1976), "Single Scattering Particle Laser Doppler Measurements of Turbulence," AGARD No. 193.
- Dimotakis, P. E., and G. L. Brown (1976), "The Mixing Layer at High Reynolds Number: Large-Structure Dynamics and Entrainment," J. Fluid Mech., 78, 535-560.
- Drain, L. E. (1972), "Coherent and Noncoherent Methods in Doppler Optical Beat Velocity Measurement," J. Phys. D: Appl. Phys., 5, 481.
- Drain, L. E. (1980), The Laser Doppler Technique, John Wiley & Sons, New York.
- Durão, D. F. G., and J. H. Whitelaw (1975), "The Performance of Acousto-Optic Cells for Laser-Doppler Anemometry," J. Phys. E: Sci. Instr., 8, 776.
- Durst, F., and R. Kleine (1973), "Velocity Measurements in Turbulent Premixed Flames by Means of Laser Doppler Anemometers," University of Karlsruhe, Sonderforschungsbereich 80, Rep. SFB 80/EM/10.
- Durst, F., A. Melling, and J. H. Whitelaw (1972), "Laser Anemometry: a Report on Euromech 36," J. Fluid Mech., 56, 143.
- Durst, F., A. Melling, and J. H. Whitelaw (1976), Principles and Practice of Laser-Doppler Anemometry, Academic Press, New York.
- Durst, F., and W. H. Stevenson (1977), "The Influence of Gaussian Beam Properties on Laser Doppler Signals," University of Karlsruhe, Karlsruhe, West Germany, Rep. SFB 80/ET/109.
- Durst, F., and J. H. Whitelaw (1971) "Optimization of Optical Anemometers," Proc. Roy. Soc. Lond., A324, 157.
- Durst, F., and M. Zaré (1974), "Removal of Pedestals and Directional Ambiguity of Optical Anemometer Signals," Appl. Opt., 13, 2562.
- Eaton, J. K., and J. P. Johnston (1980a), "Turbulent Flow Reattachment: An Experimental Study of the Flow and Structure Behind a Backward-Facing Step," Report MD-39, Mechanical Engineering, Stanford University.

- Eaton, J. K., and J. P. Johnston (1980b), "An Evaluation of Data for Backward Facing Step Flow: Report Prepared for the 1980/81 Conferences on Complex Turbulent Flows," Dept. of Mechanical Engineering, Stanford University.
- Etheridge, D. W., and P. H. Kemp (1978), "Measurements of Turbulent Flow Downstream of a Rearward-Facing Step," J. Fluid Mech., 86, 545-566.
- Fielder, H., D. Korschelt, P. Mensing (1977), "On Transport Mechanism and Structure of Scalar Field in a Heated Plane Shear Layer," Lecture Notes in Physics, Symposium on the Structure and Mechanisms of Turbulence II, Springer-Verlag, Berlin, 58-72.
- Ganji, A. R. (1979), "Combustion and Stability Characteristics of a Premixed Vortex Dominated Two Dimensional Flow," Ph. D. Thesis, College of Engineering, University of California, Berkeley.
- Ganji, A. R., and R. F. Sawyer (1980), "Turbulence, Combustion, Pollutant, and Stability Characterization of a Premixed, Step Combustor," NASA Report No. 3230.
- George, W. K., and J. L. Lumley (1973), "The Laser-Doppler Velocimeter and its Application to the Measurement of Turbulence," J. Fluid Mech., 60, 321.
- Ghoniem, A. F., A. J. Chorin, and A. K. Oppenheim (1980), "Numerical Modeling of Turbulent Flow in a Combustion Tunnel," LBL Report No. 11520, University of California.
- Glass, M., and I. M. Kennedy (1977), "An Improved Seeding Method for High Temperature Laser Doppler Velocimetry," Combust. Flame, 29, 333.
- Goldstein, R. J., and D. K. Kreid (1976), "The Laser-Doppler Anemometer," Measurements in Heat Transfer, E. Eckert and R. J. Goldstein, editors, 2nd ed., McGraw-Hill, New York.
- Görtler, H. (1942), "Berechnung von Aufgaben der freien Turbulenz auf Grund eines neuen Näherungsansatzes," ZAMM, 22, 244-254.
- Hanson, S. (1973), "Broadening of the Measured Frequency Spectrum in a Differential Laser Anemometer Due to Interference Plane Gradients," J. Phys. D: Appl. Phys., 6, 164.
- Hjelmfelt, A. T., and L. F. Mockros (1966), "Motion of Discrete Particles in a Turbulent Fluid," Appl. Sci. Res., 16, 149.
- Humphrey, J. A. C., A. Melling, and J. H. Whitelaw (1975), "Laser-Doppler Anemometry for Verification of Turbulence Models," The Engineering Uses of Coherent Optics, E. R. Robertson, editor, Cambridge University Press, Cambridge.

- Husain, Z. D., and A. K. M. F. Hussain (1979), "Axisymmetric Mixing Layer: Influence of the Initial and Boundary Conditions," AIAA, 17, 48-55.
- Jones, R. E., L. A. Diehl, D. A. Petrash, and J. Grobman (1978), "Results and Status of the NASA Aircraft Engine Emission Reduction Technology Programs," NASA Report No. TM-79009.
- Keller, J. O., L. Vaneveld, D. Korschelt, G. L. Hubbard, A. F. Ghoniem, J. W. Daily, and A. K. Oppenheim (1981), "Mechanism of Instabilities in Turbulent Combustion Leading to Flashback," AIAA Paper 81-0107.
- Kim, J., S. J. Kline, and J. P. Johnston (1978), "Investigation of Separation and Reattachment of a Turbulent Shear Layer: Flow Over a Backward-Facing Step," Report MD-37, Mechanical Engineering, Stanford University.
- Kline, S. J., and F. A. McClintock (1953), "Describing Uncertainties in Single-Sample Experiments," Mechanical Engineering, January.
- Kolpin, M. A. (1964), "The Flow in the Mixing Region of a Jet," J. Fluid Mech., 18, 529.
- Konrad, J. H. (1976), "An Experimental Investigation of Mixing in Two-Dimensional Turbulent Shear Flows with Applications to Diffusion-Limited Chemical Reactions, SQUID Report CIT-8-PU.
- Kreid, D. K. (1974), "Laser-Doppler Velocimeter Measurements in Nonuniform Flow: Error Estimates," Appl. Opt., 13, 1872.
- Lefebvre, A. H., (editor), (1977), "Lean Premixed/Prevaporized Combustion," NASA Report No. CP-2016.
- McLaughlin, D. K., and W. G. Tiederman (1973), "Biasing Correction for Individual Realization of Laser Anemometer Measurements in Turbulent Flows," Phys. Fluids, 16, 2082.
- Marvin, J. G. (1977), "Turbulent Modeling for Compressible Flows," NASA Report No. TMX-73188.
- Mazumder, M. K., and K. J. Kirsch (1975), "Flow Tracing Fidelity of Scattering Aerosol in Laser Doppler Velocimetry," Appl. Opt., 14, 894.
- Meyers, J. F., and J. I. Clemons, Jr. (1979), "Processing Laser Velocimeter High-Speed Burst Counter Data," Laser Velocimetry and Particle Sizing, H. D. Thompson and W. H. Stevenson, editors, Hemisphere Publishing, New York.
- Moore, D. W. and P. G. Saffman (1975), "The Density of Organized Vortices in a Turbulent Mixing Layer," J. Fluid Mech., 69, 465-473.

- Moss, W. D., and S. Baker (1980), "Re-circulating Flows Associated With Two-Dimensional Steps," Aero. Quart., 31, 151-172.
- Pitz, R. W., and J. W. Daily (1979), "Experimental Studies of Combustion in a Two Dimensional Free Shear Layer," Presented at the 2nd Symposium on Turbulent Shear Flows, Imperial College, London, July.
- Pitz, R. W., and J. W. Daily (1981), "Experimental Study of Combustion in a Turbulent Free Shear Layer Formed at a Rearward Facing Step," AIAA Paper 81-0106.
- Roshko, A. and L. Bernal (1981), "Organized Structure in Turbulent Shear Flow and Development of a Smaller Scale," presented at the First Annual California University Fluid Mechanics Retreat, Stanford University, April.
- Self, S. A., and J. H. Whitelaw (1976), "Laser Anemometry for Combustion Research," Combust. Sci. Technol., 13, 171.
- Sherman, F. S. (1976), "The Dynamics of Unstable Free Shear Layers - Effects of Bouyancy and Non-linear Interactions," Fluid Dynamics Trans., 8, 141-193.
- Spencer, B. W., and B. G. Jones (1971), "Statistical Investigation of Pressure and Velocity Fields in the Turbulent Two-Stream Mixing Layer," AIAA Paper 71-613.
- Stevenson, W. H. (1977), "Principles of Laser Velocimetry," Experimental Diagnostics in Gas Phase Combustion, Ben Zinn, editor, Progress in Astronautics and Aeronautics, vol. 53, AIAA, New York.
- Trolinger, J. D. (1974), "Laser Instrumentation for Flow Field Diagnostics," AGARDograph No. 186.
- Whitelaw, J. H. (1975), "Developments in Laser-Doppler Anemometry at Imperial College," Studies in Convection, B. E. Launder, editor, Academic Press, New York.
- Winant, C. D. and F. K. Browand (1974), "Vortex Pairing: The Mechanism of Turbulent Mixing-Layer Growth at Moderate Reynolds Number," J. Fluid Mech., 63, 237-255.
- Wynanski, I., and H. E. Fiedler (1970), "The Two-Dimensional Mixing Region," J. Fluid Mech., 41, 327-361.
- Yarif, A. (1975), Quantum Electronics, Wiley, New York, p. 356.
- Yeh, Y., and R. Z. Cummins (1964) "Localized Fluid Flow Measurements with an He-Ne Laser Spectrometer," Appl. Phys. Lett. 4, 176.